RICE UNIVERSITY

Nonresonant Surface Enhanced Raman Optical Activity

by

Bruce E. Brinson

A THESIS SUBMITTED
IN PARTIAL FULFILLMENT OF THE
REQUIREMENTS FOR THE DEGREE

Doctor of Philosophy

APPROVED, THESIS COMMITTEE:

_____

Naomi J. Halas, Chair
Stanley C. Moore Professor in
Electrical and Computer Engineering,
Professor of Chemistry,
Professor of Biomedical Engineering
Professor of Physics

_____

Frank K. Tittel
J.S. Abercrombie Professor in Electrical and
Computer Engineering,
Professor of Bioengineering

_____

Peter J. Nordlander
Professor of Physics and Astronomy
Professor of Electrical and Computer
Engineering

HOUSTON, TEXAS
APRIL, 2009

UMI Number: 3362133

INFORMATION TO USERS

The quality of this reproduction is dependent upon the quality of the copy
submitted.   Broken or indistinct print, colored or poor quality illustrations
and photographs, print bleed-through, substandard margins, and improper
alignment can adversely affect reproduction.
In the unlikely event that the author did not send a complete manuscript
and there are missing pages, these will be noted.   Also, if unauthorized
copyright material had to be removed, a note will indicate the deletion.

UMI®

Abstract

Nonresonant Surface Enhanced Raman Optical Activity

by

Bruce E. Brinson

Nanoshells (NS) and nanoparticles (NP) are tunable plasmonic particles that can be precisely engineered for specific applications including surface enhanced spectroscopies. A new, general method for the synthesis of core-shell and solid nanoparticles has been developed and is presented. Based on the CO reduction of Au^{3+}, this new process yields the highest quality gold nanoshells synthesized to date. The constraints on precursor lifetime have been relaxed and post-synthesis purification has been eliminated.

Nonresonant surface enhanced Raman optical activity (SEROA) has been investigated using biomolecular analytes deposited on Au nanoshell or nanoparticle substrates. The first, and currently the only, near-infrared (780 nm) excited scattered circular polarization Raman optical activity spectrometer (NIROAS) has been constructed. Surface enhanced Raman optical activity spectroscopy has been validated by the collection of symmetrical, surface enhanced, signed circular polarization intensity difference spectra from several test molecules including, (S)- and (R)-tryptophan, and (SS)- and (RR)- phenylalanine-cysteine.

Acknowledgments

I would like to sincerely thank my research advisor, Professor Naomi J. Halas, for the invitation to join her group, the experiences, and the resources provided for me to utilize throughout my graduate career. Naomi removed administrative hurtles that, until now, have prevented employees of Rice University from earning an academic degree while at Rice. The result was the first degree awarded to an employee of Rice (M.S. 2004). Prior to meeting Professor Naomi Halas, Prof. Frank K. Tittel could see my light and asked me to join the professional research staff. Truly, it is a privilege to be evaluated by Professor Tittel. Prof. Peter Nordlander has been an inspiration for years and taken time from a busy schedule to serve on this defense committee. Professor Nordlander, I am truly grateful. Thank you.

Dr. Marie Pontier Johnson (Continental Carbon Company) served as my M.S. research and thesis advisor. We continue to share intellectual discussions, some of which lead to the discovery of the carbon monoxide reduction method for the synthesis of nanoshells and nanoparticles. I would also like to extend my sincere appreciation to our collaborators Larry Nafie (Syracuse U.) and Rina Dukor, the founders of BioTools, Inc. for funding, shared technology, and fruitful conversations.

Dr. Bill passed away this year. He was an institution by the nature of his being. I wish I could put that into words that would paint the picture of my gratitude to him. Thanks to Professor Richard E. Smalley for introducing me to the world of nanotechnology. I had nanoknowledge of the change this four-letter word would make on my life. So it must be asked: What is life without three microscopes, lasers, samples, and lab stuff on an office desk at 2AM? To my co-conspirator at Midnight Laser Zeppelin

Microscopy Dr. Rhonda Anderson, science should always be so much fun. Thanks for including me.

Many years ago, while discussing the desire to return to academic life, Dr. Dial Martin (Texas A&M University) said, "If you want to go to school and you can find a way to get in, you will find a way to stay." Dr. Dial, your philosophy has been shared with numerous students, thank you. I would also like to thank David Rice of Critical Link, LLC and Dr. Daniel Neumann of Rice University for assistance with software development. J. Britt Lassiter conducted the nanoshell optical scattering experiments, and Nikolay Mirin developed the thermodynamic theory for the CO nanoshell synthesis technique. In addition, I would like to extend my sense of gratitude to all members of the Halas research group, and I would like to extend special recognition to Oara Neumann, J. Britt Lassiter, Dr. Carly Levin, Rizia Bardhan, Nikolay Mirin, Janardan Kundu, Nathaniel (Nate) K. Grady, and Dr. Surbhi Lal.

As a member of the professional research staff, I have participated in numerous exciting research projects resulting authorship / co-authorship of seventeen publications, with several pending. I thank you to all for the shared experiences, excitement, and pleasure of interacting with many great people. I am very grateful for the editing assistance of Ms. Carol Yates and Ms. Mary Pless

Table of Contents

Table of Content (continued)

Table of Figures

Chapter 1

Chapter 2

Chapter 3

Chapter 4

Bibliography

Appendices

Chapter 1. Introduction and Literature Review

1.1 Introduction

The field of vibrational optical activity is composed of two spectroscopies, Raman optical activity (ROA) and infrared analog vibrational circular dichroism (VCD)[1] ROA and VCD spectra relay the molecular stereochemical information of optically active chiral molecules. VCD is a measurement of the absorption difference between incident right- and left-handed circular polarized light. While ROA, an inelastic scattering process, is a measurement of the difference in the change of the degree of polarization in the scattered light from a sample relative to the excitation (incident) source.

With the advent of the gas filled ion laser, Raman spectroscopy precise enough to measure the minute changes predicted in the Raman scattering of circularly polarized light.[2] So small are these circular intensity differences, that dust, thermal Schlieren effects, and background fluorescence can result in spectral intensity variations much larger than the ROA signal itself.

P. W. Atkins presented the polarization density matrix formalism for change in the polarization of incident light, induced by the analyte, and observed in scattered light.[3] L. D. Barron and A. D. Buckingham extended the theory and produced the first ROA spectrum.[4, 5] It was Laurence D. Barron of Glasgow University, who pioneered ROA spectroscopy. Since the inception of ROA measurements, the greatest obstacle has been that of systematic spectral artifacts.[6] Theory developed by W. Hug and validated by experiment[7] led to the first commercially available scattered circular polarization Raman optical activity spectrometer (SCP-ROA).[8]

ROA cross-sections are E^{-3} to E^{-4}, less than the cross-section of conventional Raman, while signal-to-noise ratios can be E^3-E^4 orders greater than that of Raman spectra. The ROA figure of merit, known as the circular intensity difference (CID), is the difference in right- and left-circular polarization intensities to their sum. Typical CID values range from 10^{-3} to 10^{-6}.[9]

Correct interpretation of ROA spectra is dependent on a thorough understanding of systematic artifacts and their origin. An instrument can be characterized by comparing experimental data to theoretical (simulated) spectra of a known (standard) system, such as (R)- and (S)-(-)-α-pinene.[10] Even so, the spectra of an individual sample (not just the same kind of sample) must be carefully scrutinized.

Surface enhanced Raman spectroscopy (SERS) is a very sensitive and well-established spectroscopic technique.[11] Using aggregated Ag particles in solution as plasmonic substrates, the first experimental evidence of resonant surface enhanced Raman optical activity (SEROA) has been presented by Abdali et al. [12-14] Johannessen, Abdali, and Blanch are currently investigating the resonant surface enhanced Raman optical activity of naturally occurring biological molecules. As with most of nature, all these works are applicable to molecules exhibiting left-handed chirality. Until SEROA spectra of complimentary molecular enantiomers can be produced and compared, the validity of SEROA remains in question.[12, 15]

The objective of this work is the validation of nonresonant SEROA by the elucidation of surface enhanced CID spectra from complimentary and biologically significant enantiomers. New protocols for the synthesis of Au nanoshells and the

synthesis of Au and Ag solid nanoparticles, where carbon monoxide (CO) is the reductant, will be presented in Chapters 2.

Brinson *et al.*, developed the first near-infrared excited scattered circular polarization Raman optical activity spectrometer (NIROAS) [16]. The NIROAS is the centerpiece of this thesis and will be discussed extensively in Chapters 3 and Appendix 1. The validity of SEROA has been established by the acquisition of mirror image CID spectra from the biologically significant (S)- and (R)- enantiomers, of tryptophan, and (SS) and (RR) amine-terminated glycine-glycine-phenylalanine-cysteine (phe-cys). SEROA sample preparation and corresponding spectra are presented and discussed in Chapter 4.

1.2 Raman Scattering

Raman scattering is a molecular vibrational phenomena discovered by Sir Chandrasekhara Venkata Raman. For this work, he was awarded a Nobel Prize.[17, 18] The Raman effect, also known as Stokes emission, is the inelastic scattering of electromagnetic radiation by the vibrational states of a molecule. Consider the N_0 and N_1 vibrational energy levels shown in Figure 1-1.
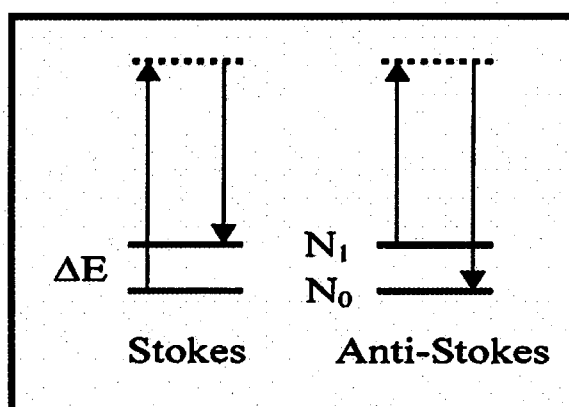
Figure 1-1. Raman energy level diagram.

If the photon incident on a material has a much larger energy than the transition energy between the N_0 and N_1 states, ΔE, it can be either elastically scattered by emitting a photon of the same frequency; a process termed Rayleigh scattering, or it can be inelastically scattered, via linear processes such as fluorescence and Raman scattering. When an incident photon interacts with a molecule in the ground vibrational state N_0, and the molecule absorbs the photon, it is raised to either a real (resonant, electronic) or a virtual (nonresonant, vibrational) state. Relaxation from either state can release energy in the form of a photon. However, a comparatively small number of the molecules may relax into a different state of the vibrational manifold. When the final state of the

molecule is in a higher vibrational level than the initial state, the scattered photon has less energy than the incident photon, the difference being ΔE. This process is known as Stokes emission. Alternatively, the molecule can be in the N_1 state when it absorbs the incident photon, and then relaxes to the N_0 ground state. In this case, the energy of the scattered photon is greater than the energy of the incident photon. This process is known as anti-Stokes Raman scattering. Under ambient conditions, the majority of molecules are in the ground state, N_0. Thus, anti-Stokes scattering intensity can be several orders of magnitude less than the Stokes scattering.[19] In this work, only Stokes modes will be evaluated

1.3 Raman Optical Activity

Raman optical activity is induced by the interaction of an electromagnetic wave with the molecular electronic dipole, quadrupole and magnetic dipole of a chiral molecule.[20] As a function of circular polarizability, a resulting Stokes emission, representative of molecular vibrations inaccessible by conventional Raman spectroscopy, can be measured. ROA is an inelastic scattering process by a chiral molecule that includes right- and left-handed circularly polarized light. A ROA spectrum results from a measurement of the difference in the change of the degree of polarization induced by the analyte, relative to the excitation source. From ROA experiments, biomolecular back bone structure, conformation, and absolute stereochemical structure can be determined.[20, 21] ROA spectra include: bending, wagging, ring deformation, ring breathing, rotation, and torsion modes.[21, 22]

Within the array of ROA spectrometers developed over the years, techniques include sample excitation by incident, random, right- and left-handed circularly and linearly polarized light. Each system must also be capable of measuring the change to the input polarization induced by the sample and thus, produce a polarization dependent spectrum. A minimum of two spectral measurements are required, one from each arm of a polarization analyzer. With the exception of particularly bright molecules such as α-pinene, contemporary data collection requires collection periods measured in hours, often over a period of days.[20]

An ROA spectrometer simultaneously produces conventional Raman spectra by summing the two polarization dependent spectra and the ROA spectra by taking the

6

difference between the two spectra. The circular intensity difference (CID), a measurement of the relative strength of an ROA signal, is given by Equation 1.

$$CID = \frac{I_l - I_r}{I_l + I_r}$$

Equation 1. Circular intensity difference.

where I_l and I_r represent the intensity of left and right handed circularly polarized light respectively.

1.4 Introduction to Nanoshells

A metal nanoshell is a plasmonic device consisting of a dielectric core surrounded by a thin, metallic shell. The core is typically a 40 to 250 nm radius spherical silica nanoparticle, surrounded by a 5 to 30 nm thick Au or Ag shell.[23, 24] Nanoshells have a tunable plasmon resonance, which is a function of relative size of the core, core index of refraction, shell, and local environment. (Figure 1-2) Their plasmon resonances can be tuned from the visible out into the near- and mid-infrared regions of the electromagnetic spectrum.[25, 26] The nanoshell resonant frequencies, lineshape, and the relative contributions of scattering and absorption to the extinction spectra (plasmon line shape)[27, 28] can be quantitatively modeled with Mie scattering theory[29]. Nanoshells have found applications as extinction, SERS[25], and SEIRA[26] substrates, photo-oxidation inhibitors in conducting polymers[30], optically triggered drug delivery substrates[31], optomechanical materials[32, 33], a diagnostic probe in whole blood[34], and a tissue specific, photo-thermal tumor therapy.[35]

The nanoshell geometry controls the far-field electromagnetic response of a nanoshell, and the local electromagnetic near-field at the nanoshell surface is also controlled by its geometry. The large, local electromagnetic fields of this simple, symmetric nanoparticle system can be accurately calculated and related to the measured SERS enhancements.[28, 36]
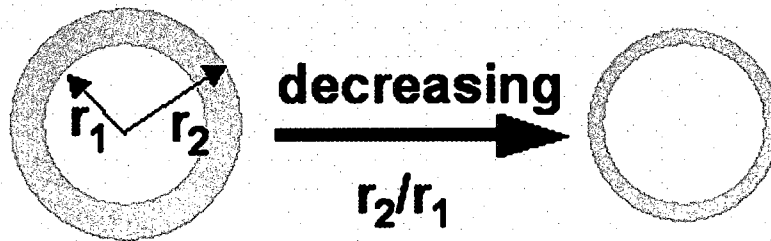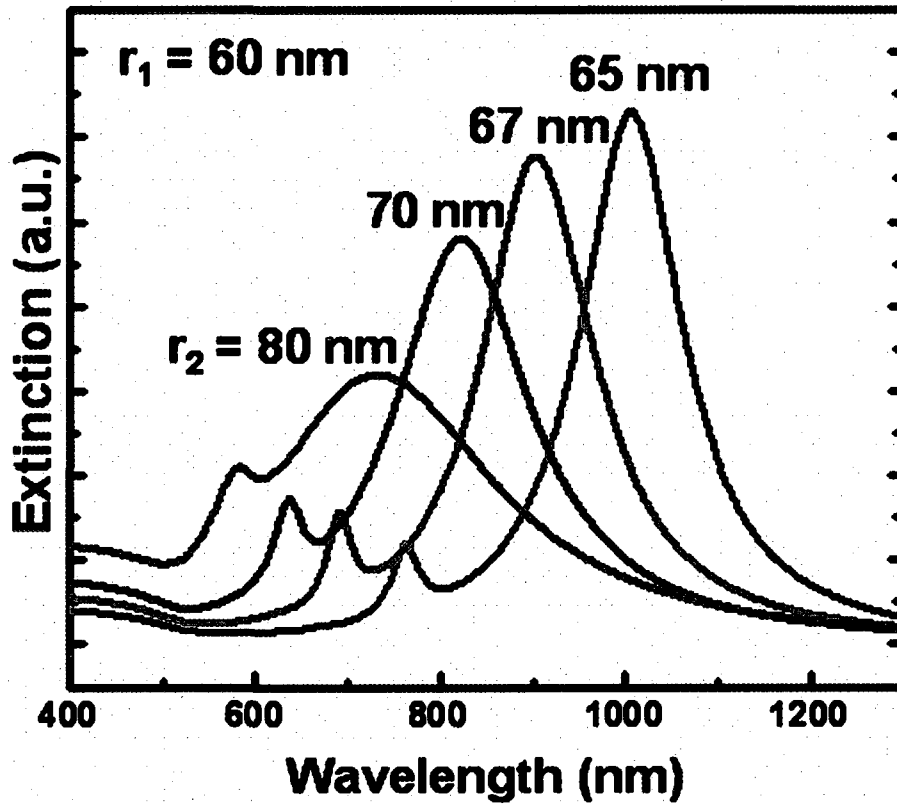
Figure 1-2Theoretically calculated (Mie scattering) optical resonances demonstrating plasmon tunability for nanoshells

Nanoshells with an inner silica core radius $r_1 = 60$ nm and an overall particle radius $r_2 = 65$, 67, 70, and 80 nm (corresponding to 5, 7, 10, and 20 nm thick Au shells). The plasmon resonance (extinction) of the particles red-shifts as r_1/r_2 increases. Modified from Oldenburg et al. (ref) to exclude the broadening mechanism.

An alternative plasmonic near-infrared resonant structure to the nanoshell is the gold nanoparticle (NP) aggregate. Au colloid consists of solid NPs, typically spherical or faceted in shape The surface plasmon resonance of the smaller spherical Au NP in aqueous solution occurs at approximately 520 nm. (Figures 1-3 and 4a) For larger, nonspherical particles, this peak has been observed to red-shift as much as 100 nm.

(Figure 1-3) While the plasmon peak of individual Au nanoparticles is off-resonance relative to 780 nm, as the distance between NPs approaches a few nanometers, a red-shifted aggregate plasmon appears at the expense of the isolated nanoparticle plasmon.[37] The degree to which the plasmon red-shifts, inversely with distance between adjacent particles. When minimal particle distance is determined by electrostatic repulsion, the aggregate peak can be shifted to ~700 nm. (Figure 1-4b) When the interparticle distance is further reduced by surface charge reduction or molecular bonding, in this case by phenylalanine-cysteine, the resulting smaller interparticle distance further red-shifts the plasmon peak into the near infrared NIR where it is resonant with 780 nm, excitation (Figure 1-4c). This effect holds for nanoshells as well.[38]
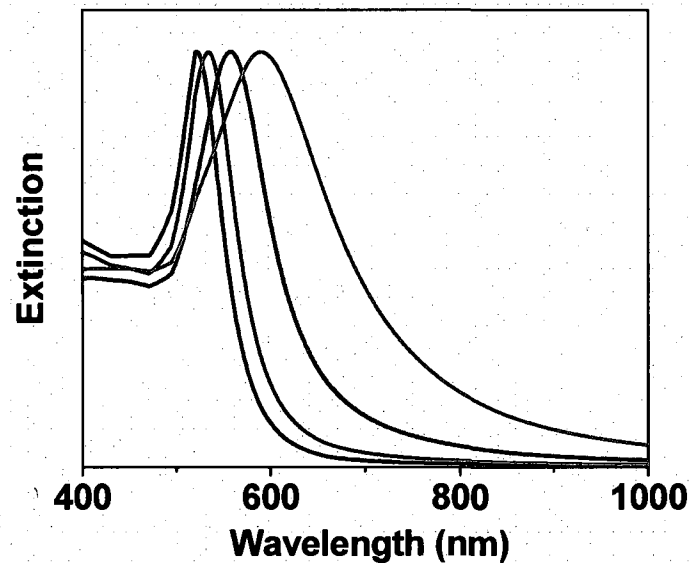
Figure 1-3 Normalized theoretically calculated (Mie scattering) optical resonances. Illustration of the plasmon red-shift with increasing particle size for Au nanoparticles with a radius of 30, 60, 90 and 120 nm.
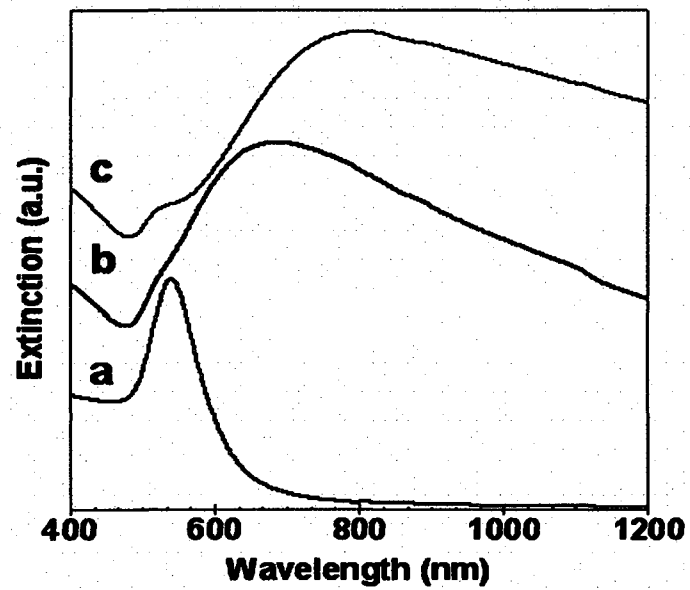
Figure 1-4. Optical extinction spectra of nanoparticles and nanoparticle films
(a) aqueous gold nanoparticles, (b) a 2D aggregated nanoparticle film, and (c) a 3D NP
film bound by amine-terminated glycine-glycine -phenylalanine-cysteine molecules.

1.5 Surface Enhanced Raman Scattering

The enhancement of the Raman spectra of molecules immobilized on a metal substrate is collectively known as surface enhanced Raman scattering (SERS).[11, 39, 40] In these studies, Raman scattering intensities were enhanced by several orders of magnitude. The use of aggregated Au nanoparticles as SERS substrates has resulted in detection limits approaching the single molecule limit.[41, 42, 43] When reabsorption is negated, for example, by the use of a NS film in air as opposed to an aqueous suspension, enhancements as high as 10^{10} have been reported.[28]

Raman spectra are chemically specific to the vibrational modes and electronic transitions (which can contribute to the spectral background) of an analyte. It is common for SERS spectra to differ from the parent Raman spectra, but in many instances, excellent repeatability can be observed or determined by digital processing methods.[44] The combination of low level delectability and specificity, lend SERS to biological, chemical, and environmental sensing applications.[37, 45, 46]

Now, over 40 years after Jeanmaire and Van Duyne published their first SERS paper, the nature of the electromagnetic and chemical mechanisms that lead to the SERS phenomena are still debated.[41, 47, 48] Reasons mitigating a unified SERS model include, but are not limited to, the nature of surfaces, particle-particle interactions, molecular binding geometry, molecular conformation, isomer distributions, and local environment.[41, 49, 50]

The use of nanoshells and nanoparticles that are resonant with a NIR laser, which is off-resonance with the analyte, has been shown to increase detection limits by 8-10

orders of magnitude.[37, 51] Plasmonic structures developed and applied to the validation of

NIR surface enhanced Raman optical spectroscopy will be presented in Chapter 2.

1.6 Polarization

The term polarization in the field of electromagnetic (EM) wave radiation describes the orientation of the electric field vector (E), as defined by the phase relationship of orthogonal components. In an isotropic medium, this phase relationship is constant. The phase relationship can be altered by reflection or when the EM wave is transmitted through a medium where a difference in the index of refraction for the orthogonal (x, y) components exists. Equation 2 describes the path drawn by the electric vector over a distance of one wavelength.

$$E = A\cos(kx - \omega t) - B\sin(kt - \omega t)$$

Equation 2. Path drawn by the electric vector.

where A, B are the amplitudes of the orthogonal x and y vectors, k (the reciprocal of wavelength) is the wavenumber, ω is the frequency of the wavelength, and t is time.

The change in the orientation of the unit vector (E) about the direction of propagation (k) over a distance of one wavelength, determines the degree of polarization (DP).

$$DP = \frac{\sqrt{Q^2 + U^2 + V^2}}{I}$$

Equation 3. Degree of polarization (DP).

where Q, U, and V are the applicable Stokes vector and I the polarization independent optical intensity.

With the exception of laser radiation, light exists in an elliptical or randomly polarized state. Linear and circular polarization can be special cases of elliptical polarization. As seen in Equation 2, when $|A|$ or $|B|$ = zero, the light is linearly polarized and when $|A| = |B| = 1$ ($A \bullet B = 0$), the light is circularly polarized. Included in a complete description of polarization is the "sense" of polarization, which describes the direction of rotation, scribed about the optical axis (k) by the E-vector. The sense is described as right- or left-handed circular polarization, and can be visualized as clockwise or counter clockwise rotation, respectively. Obviously, the direction of observation will determine how the rotation is described. After a review of optical textbooks[52-54], by convention, the sense of elliptical polarization is interpreted as if looking to the source. Figure 1-5 illustrates in three dimensions the rotation of the electric vector about the direction of propagation for right-handed (using the right-hand rule in the direction of propagation) circularly polarized light.[53] Figure 1-6 illustrates the sense of, and the change of the sense and degree of polarization for phase shift increments of $\pi/4$.[55]
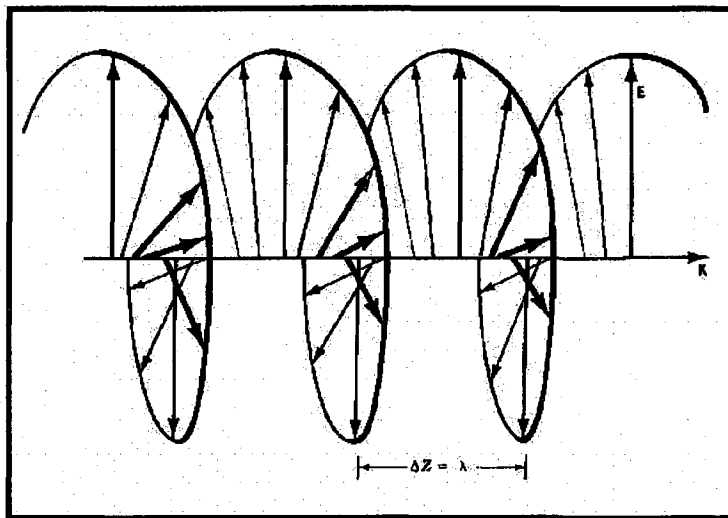
Figure 1-5. 3D artist illustration of elliptical polarization.
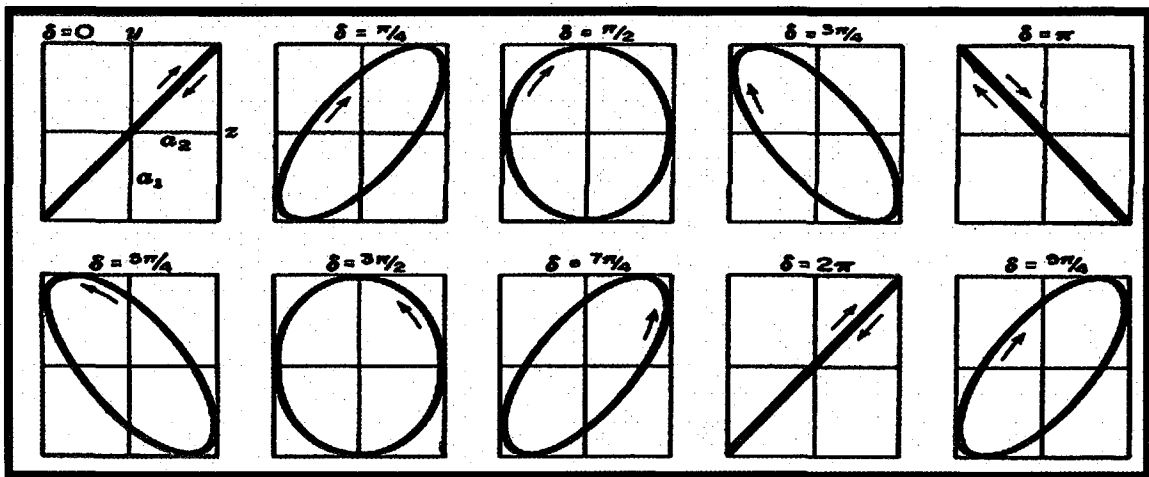
Figure 1-6. The sense and degree of polarization vs. phase shift.

1.7 Conclusion

The principles of Raman scattering, Raman optical activity, plasmonic nanoshells, surface enhanced Raman spectroscopy, and the degree of circular polarization have been presented. In chapters 3 and 4, these building blocks will be applied to the validation of surface enhanced Raman optical activity.

Chapter 2. Synthesis of Au core-shell and solid Nanoparticles

2.1 Introduction

Nanoshells are particles consisting of a dielectric core surrounded by a thin metallic shell, form a class of nanostructures with remarkable optical properties.[56-58] Au nanoshells, consisting of spherical silica nanoparticle cores surrounded by a uniform nanoscale gold shell layer, and Au nanorice, prolate hematite nanoparticles surrounded by a gold shell layer, are two examples of this general nanoparticle morphology. The unique optical properties of these nanoparticles are due to their geometry dependent, plasmon-derived optical resonances whose frequencies depend sensitively on the inner and outer dimensions of their metallic shell layers. The intense optical absorption and scattering properties of this class of nanoparticles can be made to span a remarkably large region of the electromagnetic spectrum, from visible frequencies to the far infrared.[56, 59] This property has led to the use of these types of nanoparticles in numerous applications, from fluorescence enhancement of weak molecular emitters,[60] substrates for surface plasmon resonance sensing,[61] biosensing,[34] surface enhanced Raman and surface enhanced infrared absorption spectroscopies,[26, 38, 62] to contrast enhancement in bioimaging and photothermal cancer therapy.[63, 64]

The plasmon-derived optical properties of metallic shell particles have been explicitly verified using fully quantum mechanical calculations[65-67] but can be understood in simple physical terms using the plasmon hybridization concept.[68-70] In plasmon hybridization, the tunability of the plasmon resonances of dielectric-core metal-shell nanoparticles arises from the interaction of cavity plasmons associated with the inner shell surface with sphere plasmons associated with the outer shell surface. The plasmons

associated with the inner and outer surface of the shell mix and hybridize, resulting in a lower energy, "bright" or "bonding" plasmon that couples strongly to incident light, and a higher energy "dark" or "anti-bonding" plasmon that couples weakly to incident light. The hybridization interaction is stronger for thinner shell layers, leading to a strongly red shifted resonance for the "bright" plasmon at a wavelength determined by the thickness of the shell and the overall particle radius. Therefore, to position the plasmon resonance at a wavelength of interest it is crucial to be able to synthesize metallic shell particles with thin, uniform shells.

Synthesis of dielectric core-Au shell nanostructures is a multistep process. It is initiated by functionalizing oxide nanoparticles with aminopropyltriethoxy- or - methoxysilane, followed by the binding of very small (1-2 nm diameter) Au nanoparticles onto the nanoparticle surface to a saturation coverage of nominally 25-30%.[57, 71] Core-decoration is followed by the chemical reduction of $Au^{3+}_{(aq)} \rightarrow Au^{0}_{(s)}$ onto the nanoparticle precursor surface. In this last reduction step, the tiny Au islands grow larger and ultimately merge, resulting in the formation of a continuous, multicrystalline metallic shell layer. Once formation of the shell layer is complete, the optical properties of the plasmonic nanoparticles correspond quantitatively to classical electromagnetic theory.[72] Although the plasmon resonance of a nanoshell is robust with respect to small defects or variations in surface roughness,[73, 74] for the electromagnetic response of plasmonic nanoparticles to agree quantitatively with theory, it is critically important that the shell layer formation on the nanoparticle surface have a continuous and uniform morphology. A striking example of a "nanoshell defect" that can give rise to drastic changes of the optical properties is the nanoegg, a metallic nanoshell with a

homogeneous metallic shell of nonuniform thickness. This particle can be fabricated in a controlled manner[75] and is described as a nanoshell with a displaced (nonconcentric) dielectric core. The symmetry breaking of core displacement modifies the optical properties quite dramatically, giving rise to additional hybridized plasmon resonances in the extinction spectrum of the nanoparticle.[75, 76]

Plasmon tunable, Au nanoshells, Au nanoparticles and nanoparticle aggregates have been established as excellent SERS substrates.[11, 28, 37]. When a molecule is resonantly excited, specimen fluoresce may obscure vibrational spectra. The molecules to be evaluated for SEROA are transparent in the NIR. For biological applications, designing a SEROA substrate that is nonresonant in the visible spectrum and resonant in the NIR should enhance the vibrational spectra while eliminating specimen fluorescence. The plasmon peak profile of Au nanoshells and nanoparticle films can be tuned to this specification. Nanoshell and nanoparticle sample structures have been develop and successfully applied to Surface enhanced Raman optical activity experiments. The SEROA sample structures will be elaborated on in chapter 4.

The aqueous phase synthesis of gold nanoparticles depends on the reduction of tetrachloroauric acid in the presence of a reducing agent. Several reducing agents have been reported for the synthesis of metallic nanoparticles, and typically have a significant influence on the morphology of the final nanoparticle product. For the growth of gold or silver shell layers on silica nanospheres, the shell layer morphology depends on the reducing agent used in the metallization process.[71, 77] For example, in the case of Au nanoshells, the reducing agents formaldehyde (H_2CO), hydroxylamine-hydrochloride, and sodium borohydride do not produce equivalent results in otherwise comparable

synthesis protocols.[71] Also associated with the use of certain reductants have been variations in shell layer morphology due to specifics of reagent preparation. Both colloidal solutions and reductant solutions are known to change slowly over time, resulting in the growth of nanostructures with morphologies deviating from those achieved with freshly prepared solutions. These slow variations are most likely due to changes in equilibrium concentrations of the various ionic constituents or of dissolved gases, and are quite challenging to monitor, as is their precise influence on shell layer growth. A reducing agent method immune to such variations would provide consistent reproducibility in shell formation and improve the reliability of plasmonic nanoparticle fabrication.

In this chapter a robust and reliable method is reported for the growth of an Au layer on a prepared dielectric nanoparticle surface based on the use of carbon monoxide gas (CO) as the reducing agent.[78, 79] The shell growth is demonstrated on silica core-Au shell nanoshells and hematite core-Au shell nanorice structures. We compare nanoparticles prepared with this new method to nanoparticles prepared using the conventional liquid phase reductant, formaldehyde (H_2CO). For both nanoparticles, the growth of a continuous Au shell layer is achievable at smaller thicknesses with CO as the reducing agent. The CO reduction method is also applicable to Au and Ag colloid synthesis. Based on CO flow rates, flow times and k-carb age the nature of the Au colloids can be controlled.

2.2 Synthesis of gold Nanoshells

Ensemble extinction spectra, single particle scattering spectra and SEM images of specific single nanoshells and nanorice grown by both methods provide clear evidence that thinner, more uniform shell layer morphologies on nanoshells and nanorice can be fabricated with this approach. When precursor chemicals are prepared within a few days of nanoparticle synthesis both CO and H_2CO reduction methods produce comparable high quality nanoparticles. However, the reduction of Au^{3+} by CO results in the growth of high quality shell layers independent of the age of precursor reagents.

2.3 Preparation of precursor solutions

A multistep procedure was performed to prepare the various precursors,[56] followed by reduction of aqueous Au^{3+} to Au^0 , resulting in nanoshell or nanorice formation. With the exception of core functionalization by APTES or APTMS in ethanol, all components of the nanoparticle precursor solutions and suspensions were prepared using Milli-Q™ water.

Unless otherwise specified, all chemicals were supplied by Sigma-Aldrich or Fisher Scientific and used without further modification. Deionized water (18 M$\square$) was provided by a Milli-Q™ system. 1) Chloroauric acid: gold (III) chloride ($HAuCl_4 \cdot 3H_2O$, 99%), 2) THPC colloidal gold suspension: Tetrakis(hydroxymethyl)phosphonium chloride (THPC, 80% solution in WATER), sodium hydroxide (1 M), and chloroauric acid, 3) Plating Solution: potassium carbonate (certified A.C.S., Fisher Sci.) and chloroauric acid, 4) SiO_2 core functionalization: condensed silica core particles (Ammonia stabilized, 30% colloid silica, Precision Colloids, Cartersville, Georgia) and 3-aminopropyltriethoxysilane (APTES, minimum 98% Sigma), 5) Hematite cores: ferric

chloride (FeCl$_3$·6H$_2$O) and potassium phosphate (KH$_2$PO$_4$), 6) Precursor nanoparticle synthesis: functionalized silica or hematite cores, THPC gold solution, sodium chloride, 200 proof ethanol (Pharmco-Aaper), 7) Reducing agents: carbon monoxide (CO, 99.0%) (Matheson-Trigas) or formaldehyde (H$_2$CO, 37%). 8) electron microscopy sample preparation: silicon substrates (Addison Engineering, Inc.), glass microscope slide cover slips, poly(4-vinylpyridine) (PVP, MW 160,000).

Caution: ethanol, H$_2$CO, CO, chloroauric acid, THPC, APTMS, APTES and piranha present potential health and or fire hazards. Appropriate precautions should be observed at all times.

Chloroauric acid

A 1% by weight (2.54 mM) aqueous chloroauric acid solution was prepared and stored in an amber glass container for a minimum of three days before use.

Ferric Chloride solution

An aqueous solution containing 20 mM FeCl$_3$ – 400 µM KH$_2$PO$_4$ was prepared prior to the precipitation of hematite particles.

Synthesis of THPC Gold Suspension

A THPC gold solution composed of 1-2 nm Au colloid was prepared according to Duff et al.[80] Under rapid stirring, 1.2 mL of 1 M NaOH was added to 180 mL of WATER, followed by the addition of 4 mL of a 1.2 mM aqueous THPC solution to yield a final THPC concentration of 2.6 µM. After five minutes of continuous stirring, 6.75 mL of 1 wt % aqueous chloroauric acid was added in one quick motion, after which the solution immediately turns to a medium brown color. The final solution was refrigerated for at least 2 weeks before use. The product has a shelf life of ~ 6 months when stored at

4 °C. The suspension quality, which degrades with increasing Au colloid size, can be monitored by watching for a pronounced Au colloid peak in the optical extinction spectrum, which appears upon nanoparticle restructuring or aggregation.[80, 81]

Synthesis of Au Plating Solution

A 44 µM aqueous $HAuCl_4$ plating solution was produced by the addition of 3 mL of 1 wt % chloroauric acid to 200 mLs of a 1.8 mM aqueous K_2CO_3. The solution is then stored for a minimum of 24 hours. Typically, when the plating solution is reduced by H_2CO, the highest quality nanoshells, as assessed by SEM imaging and optical properties, were obtained when used between 24 and 72 hours after preparation. In the case of reduction by $CO_{(g)}$ the shelf life time is extended beyond 6 weeks.

Synthesis of Ag particle (colloid) precursor

An $AgNO_3$ saturated aqueous solution was produced by the addition $AgNO_3$ to WATER until after vigorous agitation, precipitates continued to formed on the bottom of the bottle. The solution was aged under ambient conditions for 2 hours to several days. Clear liquid was removed and passed through 0.2 µM filter paper into a brown bottle. The solution was aerated with Ar before use.

Synthesis of Hematite Core Particles

Spindle-shaped hematite particles with an aspect ratio of 6.3 (340 ± 20 nm x 55 ± 5 nm)[57] were prepared by forced hydrolysis of ferric chloride salts in an alkaline media. Briefly, 100 mL of reaction mixture containing 20 mM of $FeCl_3$ and 400 µM of KH_2PO_4 solution were sealed in a round bottom flask and heated at 100 °C for 72 h. The resulting dark orange precipitate consisting of α-Fe_2O_3 particles were washed several times in

water and ethanol at 3900 RCF for 25 minutes per centrifugation cycle. The final precipitate was redispersed in 25 mL ethanol and used as stock solution".[57, 82]

APTES Functionalization of Silica Cores

The protocol used for 126 nm diameter cores is presented here. This general procedure is applicable for various silica core sizes; however, the volume of APTES scales with the available silica core surface area and the relative centrifugal force is inversely related to particle size. For example, silica core particles with a 36, 95, and 190 nm radii were centrifuged at 6000, 1000, and 400 RCF, respectively. As-purchased SiO_2 particles were diluted from 30 wt % to 1 wt % in water. Ammonia stabilization of the particles was removed by: washing the functionalized cores three times via centrifugation at 4000 RCF for 30 minutes; removal of the supernatant, followed by redispersion in 40 mL of water using an ultrasonic probe. After the final removal of the supernatant, the particles were redispersed in ethanol. This process (in ethanol) was repeated an additional three times. The final suspension was redispersed in 40 mL of ethanol, placed in a polypropylene flask, and stirred rapidly. Fresh APTES (300 μL) was added to the suspension with continuous stirring for 10 minutes. The solution was sealed and slowly stirred overnight under ambient conditions.

Next, the mixture was boiled in a borosilicate container for two hrs. Total evaporation of the solvent during the synthesis of the functionalized cores was prevented by the continuous addition of ethanol. Again, the functionalized core particles were washed three times in ethanol by centrifugation at 3500 RCF for 30 minutes as described in the previous section. After the last centrifuge cycle and removal of supernatant, the functionalized particles were redispersed in 20 mL of ethanol. This process resulted in

Ammonia (NH$_4$)-terminated nanoparticles that may be stored and reliably used to fabricate high quality nanoshell precursor particles for at least a year. However, the actual shelf life has not been characterized beyond one year. An ultrasonic probe was used to redisperse the cores immediately before the synthesis of the nanoshell precursor particles in the next step.

APTMS-Functionalized Hematite Particles

(by Rizia Bardhan) 5 ml of as-prepared hematite nanoparticles were stirred to a rapid vortex, after which 600 μL APTMS was added. The stirring velocity was reduced and continued for 12 hours. Excess APTMS was removed by several centrifugation / ethanol cycles after which the core particles were redispersed in ethanol."

Synthesis of Nanoshell Precursor Particles

First, 40 mL of a THPC gold solution (see above) was sonicated for 1 minute. During sonication, 4 mL of 1 M NaCl was added, followed immediately by the addition of 300 μL of the APTES functionalized silica or APTMS functionalized hematite nanoparticle suspension. After continuous sonication for an additional 1-2 minutes, the solution was allowed to reach equilibrium over a 12 hr period. This step was followed by centrifugation at 1400 RCF (or 1150 RCF for nanorice) for 20 minutes to remove excess THPC. The precursor nanoparticles formed a pellet at the bottom of the centrifuge tube. After removal of the supernatant, the particles were resuspended in 30 mL of WATER with a sonicating probe; centrifuged a second time and redispersed in 5 mL of WATER. The nanoparticle precursor suspension was refrigerated when not in use. The highest quality and thinnest complete shells are produced within a few days of synthesis, yet complete nanoshells may still be obtained after 1-2 months.

2.4 Synthesis of Nanoshells and Nanorice

The synthesis of nanoshells and nanorice follow a common protocol. Under ambient conditions, two $Au^{3+}_{(aq)}$ reducing agents: $CO_{(g)}$ and $H_2CO_{(aq)}$ were compared in nanoshell and nanorice synthesis. For nanoshells, the plating solution (aged 5 and 6 days, used with H_2CO and CO reduction methods, respectively) and nanoparticle precursor suspension (aged 9 and 49 days, H_2CO and CO, respectively) measured by volume, were combined to produce a sequence of 6 mL suspensions with Au ion to particle ratios between 2.5×10^7 and 2×10^8. Pairs of 3 mL aliquots of each nanoshell or nanorice precursor solution were prepared in glass vials. (Nanoshells were successfully synthesized using plating solutions as old as 37 days with the same batch of precursor nanoparticles used in the experiments reported in this paper.) Nanoparticle concentrations can vary significantly batch-to-batch between nanoshell precursor solutions.

The Au^{3+} reduction technique by H_2CO (Equation. 1-3) includes the rapid discharge of 15 μL of H_2CO from a 100 μL pipette into 3 mL of the precursor suspension, after which the sample vial is gently vortexed by hand for about 10 seconds. (When the process is scaled to produce larger quantities of nanoshells, typically 200 mL of plating solution would be used. In this case, the nanoshell precursor material is stirred rapidly, to produce a strong vortex before the addition of H_2CO.) The nanoshell and nanorice suspensions produced by H_2CO reduction were subsequently aged for a minimum of 10 minutes, allowing for complete consumption of the Au^{3+} stock solution before the collection of optical spectra. SEM samples were prepared within the hour. H_2CO-reductant nanoshells must be promptly washed by centrifugation at 300 RCF (or 150 RCF for nanorice) for 10-15 minutes and redispersed in WATER or an aqueous

1.8mM K_2CO_3 solution to remove residual H_2CO. Failure to wash the H_2CO-nanoshells will result in particle aggregation within a few hours.

Reduction of Au^{3+} by CO (Equation. 4-6) was performed either by aeration or by exposure of solution to a CO atmosphere. For the aerated samples, CO was delivered through a glass diffusion tube (Chemglass) immersed in the bottom of the vial at a flow rate (Cole Parmer) of 25 sccm for periods of 10 to 15 seconds. In the atmospheric CO technique, the volume in the sample vial above the suspension was filled with CO, after which the vial was capped and gently rocked for five to ten seconds. CO-reductant nanoshell and nanorice optical extinction spectra were collected immediately. SEM samples were prepared within the hour. CO-nanoshells do not require post reduction washing.

2.5 Characterization and Comparison of Nanoshells and Nanorice reduced using H₂CO and CO

Optical extinction spectra of aqueous samples in 1 cm path length polystyrene cuvettes (Fisher Scientific) were collected using a Varian Cary 5000 UV-VIS-NIR scanning spectrophotometer. Scanning electron micrographs and energy dispersive x-ray (EDS) spectra were obtained with an FEI Quanta 400 Scanning Electron Microscope (SEM) operated at 30 kV in the environmental (ESEM™) mode with an WATER vapor pressure of ~2 Torr. For high-resolution SEM imaging Si substrates were cleaned by immersion in a 3:1 H_2SO_4: H_2O_2 (piranha) for 20 minutes, thoroughly rinsed with Milli-Q water and dried with filtered N_2. *Piranha and the components of piranha are highly corrosive chemicals that present numerous health hazards. When H_2O_2 and H_2SO_4 are combined, an exothermic, potentially explosive reaction will result. Prior to working with piranha solutions, the reader is encouraged to review OSHA form 174, Sept. 1985, and to take all necessary precautions.* The substrates were then coated with a PVP adhesion layer as described above. They were subsequently rinsed with ethanol, dried with filtered N_2, and allowed to cure under ambient conditions for 12 hours. Nanoparticles were immobilized on the substrate surface by the sedimentary deposition for a period of 1-2 hours after which they were gently rinsed with water and dried with filtered N_2.

Optical scattering spectra: Single particles scattering experiments were conducted by J. Britt Lassiter. Optical scattering spectra were collected for individual nanoshells deposited over SiO_2 using an inverted microscope (Zeiss Axiovert 200 MAT) in the dark-field configuration. A reflection dark-field objective (100x, NA 0.9) was used to focus the image of each single nanoparticle at the entrance slit of the spectrograph (SP-2156;

Acton Research, Acton, MA). Data were collected with a charge-coupled device array (PhotonMax 512; Princeton Instruments, Trenton, NJ).[72]

To facilitate the analysis of the same particle by both ESEM and optical scattering experiments, acetone-cleaned glass substrates were patterned by the deposition of an Au film through an alphanumerically indexed transmission electron microscope grid (e.g., a mask; Ted Pella, Inc.) in contact with the SiO_2 surface. An adhesion layer was added to the substrate by immersion in a 1 wt. % PVP-ethanol solution for 8-12 hours after which they were rinsed with ethanol and dried with filtered N_2. Nanoshells were allowed to deposit on the surface for 20 seconds, which resulted in an interparticle spacing of nominally 5 μm.

For the single particle optical scattering spectra collection, ESEM images and the optical microscope dark field of view were correlated to locate a specific nanoshell. By designing samples with an appropriate particle-to-particle separation, an adjustable slit can be used to optically isolate an individual nanostructure. Spectral data were acquired using the previously described spectroscopic system and processed by our own analysis software (MatLab).

Characterization of Nanoshells

Theoretical spectra which agree well with the empirical optical extinction spectra were calculated using generalized Mie theory.[36] Both experimental and theoretical spectra were normalized at the maximum extinction values. An r_1 value of 63 nm was determined by combined scanning electron microscopy (SEM) and Mie scattering theory. Using this value of r_1 (63nm) and the dielectric constant of the medium, (H_2O, 1.77), the Au shell[83] and the dielectric core (SiO_2, 2.04), the value of r_2 (85 nm) and the theoretical

extinction efficiency (A$_{theoretical}$, 4.98) was determined using Mie theory.[36, 84, 85] To

determine the concentration of the nanoparticle precursor suspension, the Beer-Lambert

law was used:

$$NS/mL = \frac{2.303 \times A_{Dp}}{A_{theoritical} \times L \times 2\Pi \times r_2{}^2}$$

Equation 2-1 The Beer-Lambert law

Where L is the optical cell path length (L = 1 cm), r_2 is the overall nanoshell

radius in cm, A$_{theoretical}$ is the peak extinction efficiency extracted from the theoretical

extinction spectra for [r_1, r_2] nanoshells, and A$_{Dp}$ is the experimentally measured peak

absorbance.

The CO$_{(g)}$-reductant [63,85] nm nanoshells (Figure 2-2A vi) were chosen as the

point of reference for the precursor Au^{3+} to nanoparticle ratio, based on SEM, optical

extinction, and Mie theory. The nanoshell density was determined to be 2.86 x 10^9/mL

thus the precursor Au^{3+} / nanoparticle ratio was 3.05 x 10^7. The sample set was scaled

relative to this value.

2.6 Results and Discussion

The growth of a continuous, uniform Au layer on a dielectric nanoparticle is the

critical step in the synthesis of nanoparticles such as nanoshells or nanorice, giving rise to

their unique geometry-dependent plasmon resonant properties. Here we report a novel,

streamlined method for Au layer metallization on prepared nanoparticle surfaces using

carbon monoxide as the reducing agent. This approach consistently yields plasmonic

nanoparticles with highly regular shell layers and is immune to variations in precursor or

reagent preparation

A schematic of a nanoshell precursor nanoparticle consisting of ultrasmall Au nanoparticles bound to a silica nanoparticle surface, two reductant methods used for shell layer growth, and the morphological differences in the final metalized nanoparticle are shown in Figure 2-1. This schematic represents the final reduction step where the silica nanoparticle-bound Au nanoparticles coalesce into a continuous, multicrystalline metallic layer on the nanoparticle surface. In particular, this schematic illustrates the thin shell layer limit, where just enough $Au^0_{(s)}$ is deposited on the nanostructure to result in the formation of a continuous shell layer. In general, different reductants may require different concentrations in Au^{3+} to achieve continuous coverage of the nanoparticle: a complete shell layer that forms at lower Au^{3+} concentrations would be thinner, and the resulting nanoparticle would have a longer wavelength plasmon resonance.

$$CO_{(g)}$$

$$H_2CO_{(l)}$$
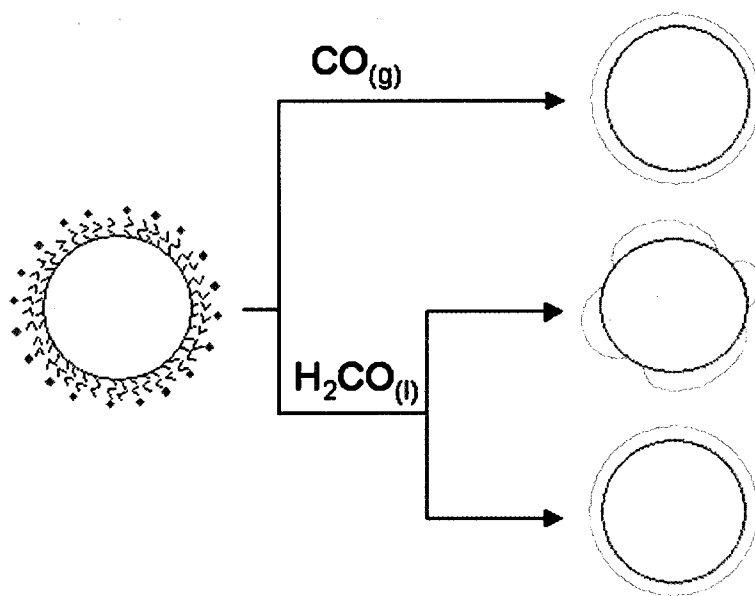
Figure 2-1 Schematic of shell layer deposition for NS synthesis in the thin shell limit.

The SiO$_2$ core decorated with Au nanoparticles, in a HAuCl$_4$ solution, serves as the deposition substrate, upon which a shell layer is grown using either carbon monoxide or formaldehyde reductants. Variations in shell morphology, observed when using the H$_2$CO reduction method, can be avoided using CO as the reducing agent.

The evolution of the optical extinction of the nanoshell precursor nanoparticles during shell layer growth as a function of Au^{3+} concentration, for the CO$_{(g)}$ and H$_2$CO reductants, is shown in Figure 2-2. At low Au^{3+} concentrations, metal deposition onto the precursor nanoparticle enlarges the discrete Au nanoparticles on the nanostructure surface. In this concentration regime, the extinction peak shifts to longer wavelengths due to the increased size of the nanoscale Au islands on the nanoparticle surface and decreased distance between these islands, resulting in increased interparticle plasmon coupling and a red shifted plasmon resonance. This red shifting continues with increasing Au^{3+} until a concentration resulting in the formation of a complete shell layer. Once a complete shell layer is formed higher Au^{3+} concentrations, result in increased thickness of the metal shell layer and a shift of the nanoshell plasmon to shorter wavelengths. The long wavelength limit therefore corresponds to the minimum Au^{3+} concentration required to form a continuous shell layer. The longer the wavelength, the thinner the shell layer of the nanoparticle formed.

In Figure 2-2A we see this transition of the extinction peak to longer wavelengths, then shorter wavelengths, with increasing Au^{3+} concentration. The maximum wavelength depends significantly on the type of reductant. In this case, the CO reductant yields nanoparticles with a peak extinction wavelength shifted to a measurably longer wavelength (780 nm) than the formaldehyde reductant (745 nm) for the thinnest shells.

33
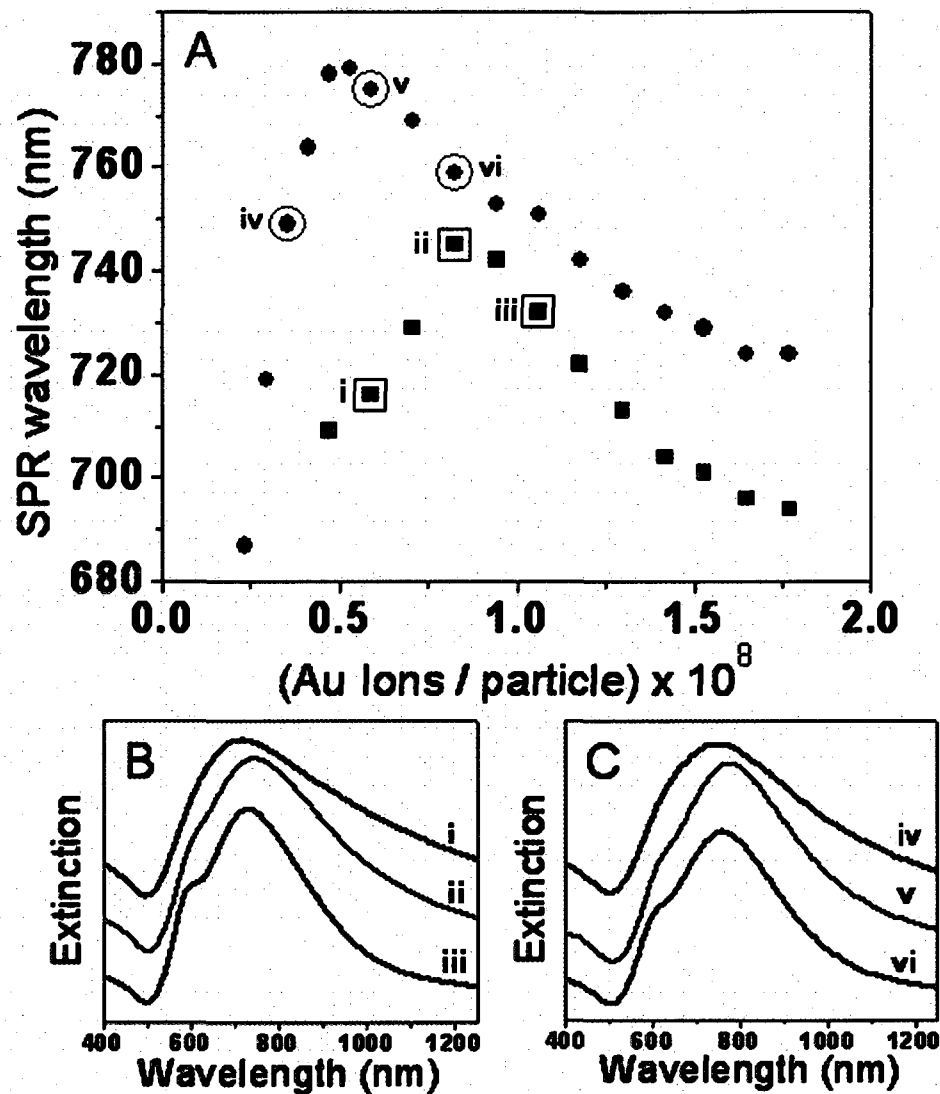
Figure 2-2 Plasmon resonance shift and extinction spectra of nanoshells synthesized using the CO and H₂CO reduction methods.

(A) Surface plasmon resonance wavelength as a function of available Au ions per particle for nanoshells grown with CO (red) and H_2CO (blue) reducing agents. (B, C) Selected extinction spectra corresponding to the data points (i-vi) in (A) for nanoshells grown with (B) H_2CO and (C) CO reducing agents. Extinction spectra (i) and (iv) are corresponding to incomplete shell layer growth. Extinction spectra (ii) and (v) correspond to nanoshells near the thin shell limit, and extinction spectra (iii) and (vi) correspond to nanoshells with thicker shell layers.

The large wavelength difference seen here, between nanoshells grown using the CO and H_2CO reducing agents, corresponds to the use of older nanoshell precursor and H_2CO reductant solutions, and is generally a function of the age of these solutions. The longer peak wavelength achieved for nanoshells formed using the CO reductant occurs at a ~40% lower Au^{3+} concentration per nanoparticle than for shell layers grown using the formaldehyde reductant, consistent with the formation of thinner continuous shell layers. These two characteristics indicate that less Au^{3+} is required to form a complete shell layer for the CO reductant than for the formaldehyde reductant in this case.

Extinction spectra representative of various stages in the growth of the shell layer (Figure 2-2 (i)-(vi)) are shown in Figure 2-2 (B,C). Spectra corresponding to the regime of incomplete shell layer growth, (i) and (iv), show a broad and relatively featureless curve, while the other curves show evidence of both dipole and quadrupole resonances in the spectral lineshape, corresponding to the extinction spectrum of a nanoshell with a continuous shell layer. Comparison with Mie scattering theory indicates that the difference in shell thickness for the two-reductant methods, in the thin shell limit is approximately 3-5 nm. However, a closer examination of the nanoparticles in the thin shell limit reveals significant reductant-dependent differences in morphology for nanoshells fabricated with these two reducing agents.

An examination of nanoshells grown with Au^{3+} concentration corresponding to the maximum wavelength shift reveals the largest differences in nanoshell morphologies obtainable with these two reductants (Figure 2-3). In the case where nanoshells are synthesized from reductant and nanoparticle precursor solutions aged 5 and 9 days respectively, comparable nanoshell morphologies result, with continuous uniform layers,

Figure 2-3 A,C. Occasional pinhole defects can be detected on the nanoshells grown using the H_2CO reducing agent solution (Figure 2-3C) but are generally not visible for the nanoshells grown with the CO reductant (Figure 2-3B).
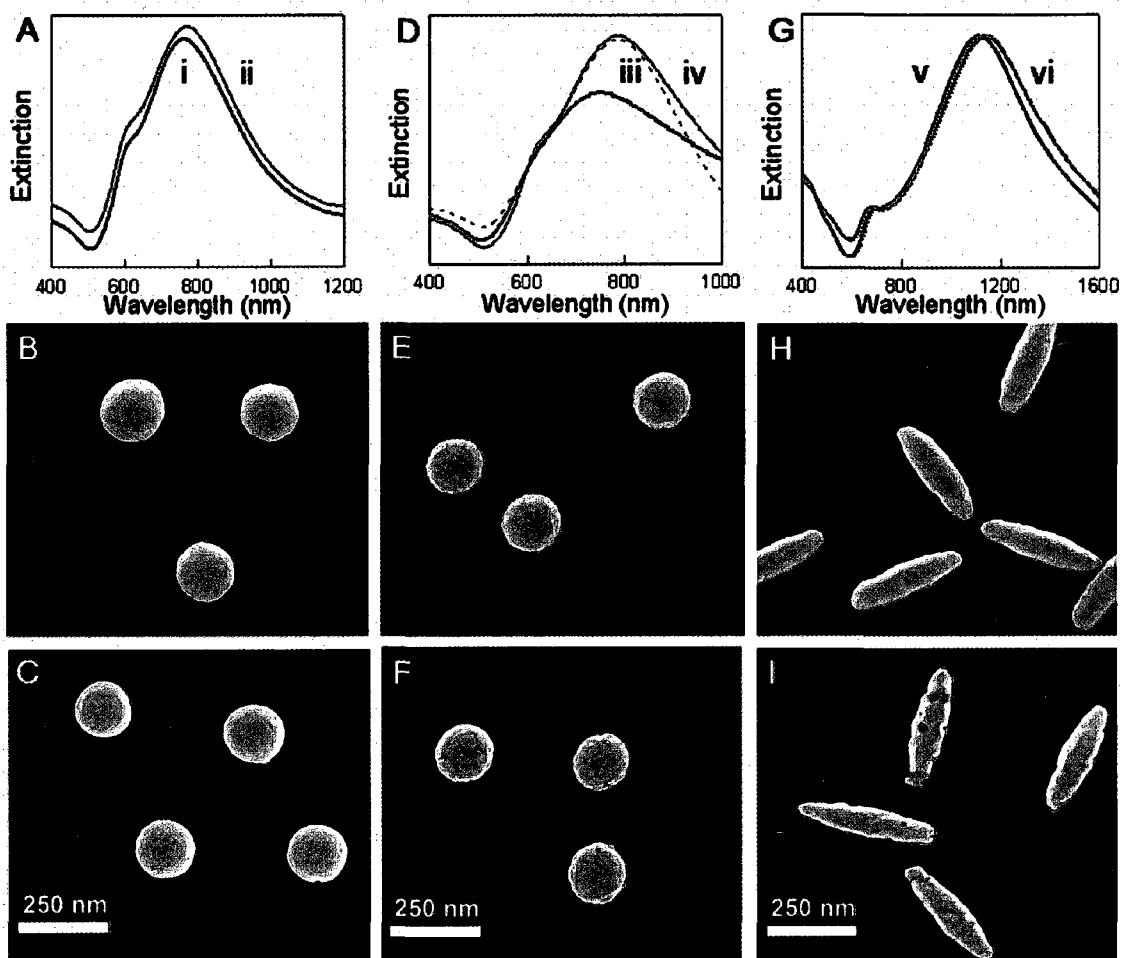
Figure 2-3 Nanoshell and Nanorice Extinction spectra and SEM images.
(A) Optical extinction spectra of nanoshells synthesized under optimal conditions (reductant solution aged 5 days and precursor nanoparticle suspension aged 9 days) (i) [63,83] H_2CO-nanoshells, (ii) [63,83] CO-nanoshells. Scanning electron micrograph (SEM) images of (B) CO and (C) H_2CO-nanoshells corresponding to the spectra are shown in (A). (D) Optical extinction spectra of nanoshells synthesized using aged precursor solutions (reductant solution aged 6 days and precursor nanoparticle suspension aged 49 days) (iii) H_2CO-nanoshells, (iv) [63,75] CO-nanoshells and the Mie theory fit corresponding to (iv). (E, F) SEM images of nanoshells grown using (E) CO and (F) H_2CO reductant solutions corresponding to the spectra shown in (D). G) Optical extinction spectra of nanorice grown using (v) H_2CO and (vi) CO reductant solutions. SEM images of nanorice grown using (H) CO and (I) H_2CO reductant solutions whose spectra are shown in (G).
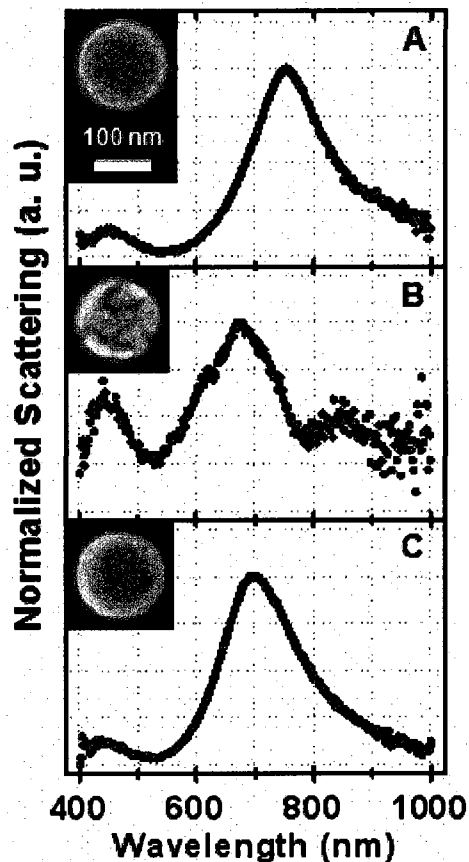
Figure 2-4 Normalized scattering spectra and corresponding SEM images of individual nanoshells.

Nanoshells were grown using (A) CO and (B) H_2CO reducing agents in the thin Au layer limit, using the same Au^{3+} ion concentration. (C) nanoshell grown with H_2CO reductant (not in the thin Au layer limit).

For the case where the reducing agent and precursor solutions have been aged for

6 and 49 days respectively, a greater variation in nanoshell morphology between the two

reducing agents results. The extinction spectra and representative SEM images are shown

in Figure 2-3 D,F. Nanoshells grown with the CO reductant are observed to have

continuous and uniform shell layers, Figure 2-3 E. Nanoshells obtained using the H_2CO

reductant show incomplete shell layer growth with extended, interconnecting fissures in

the shell layer. The extinction spectrum of the nanoshells prepared with the CO reducing agent agreed quantitatively with Mie scattering theory.

An extension of the thin shell limit by CO reduction was also observed for nanoshells synthesized with silica core radii of 36, 95, and 190 nm (data not shown). This variation in shell quality also extends to the synthesis of nanorice, which incorporates spindle shaped hematite core nanoparticles. In the synthesis of nanorice, similar changes in morphology that depend upon the type of reducing agent used are obtained. For a thin shell layer, nanorice grown using CO as the reducing agent have significantly more continuous shell layers with fewer defects than is typical of nanorice synthesized using H_2CO as the reducing agent (Figure 2-3 (G-I)).

Single particle scattering spectra of the specific individual nanoshells, correlated with the ESEM images of each nanoparticle, provide the most detailed picture of how the nanoparticle morphology affects the plasmon response of the nanoparticle.[20,35] Typical scattering spectra obtained for individual nanoshells in the thin shell limit, prepared with the same Au^{3+} concentration but using the two different reductants, are shown in Figure 2-4. The nanoshell grown using CO as the reductant (Figure 2-4 A) has both a highly uniform shell morphology and a high quality nanoshell plasmon line shape. A representative nanoshell grown at the same Au^{3+} concentration but with H_2CO as the reducing agent has an incomplete shell layer and a correspondingly poorly defined plasmon line shape and peak wavelength in its scattering spectrum, Figure 2-4 B. The particle-to-particle spectral variation for the nanoshells grown using theH_2COreductant was far greater than that for the nanoshells grown using CO as the reductant, which is directly a result of a greater particle-to-particle variation in shell morphology. In addition,

the higher energy "dark" plasmon mode at 450 nm, only weakly allowed for a spherically symmetric nanoshell, appears much more prominently in the scattering spectrum of the incompleteH₂CO-reductant nanoshells, in some cases having an amplitude approaching the "bright" plasmon at ~700 nm. The H_2CO reductant does, however yield high quality nanoshells when thicker shell layers are grown, as seen in the spectrum and image of a representative nanoshell in Figure 2-4 C.

2.7 Synthesis of Gold and Silver Nanoparticles by CO Reduction

Gold nanoparticles (NP) maybe produced by the reduction of Au plating solution using H_2CO and CO, as described for the synthesis of NS. By the CO aeration method, silver NP maybe produced by the reduction of a sliver plating solution ($AgNO_3$).

Au nanoparticles (colloid) synthesis by H_2CO reduction is performed in the same manner as in the synthesis of core-shell particles. H_2CO particles must be washed in the manor previously described (2500 RCF, 20-30 min.). In the case of H_2CO, the colloids become larger and the SPR line widens with increasing Au plating solution age. It is preferred that the minimum volume of H_2CO should be introduced to the system, so that the Au plating solution age is the variable in the synthesis of Au NP by H_2CO reduction.

Visually, a typical H_2CO-Au product has an iridescent orange-brown color in reflection and is purplish in transmission. The dynamic range for the SPR peak position is 520 - ~600 nm, with observed colloid sizes ranging from 50-100 nm. In the washing process, an initial volume of 40 mL is centrifuged, after which all but 100-200 μL of supernatant is removed. The NPs were resuspended in 10-30 mL of WATER. As with all

H_2CO reduced Au^{3+} products, after the washing process, H_2CO l is observed in aqueous SERS spectra of the Au colloid.

The synthesis of Au NP (Ag NP) using CO is a simple process; aerate the plating solution with CO in the same manner used for NS. As with CO-NS, CO-NPs do not require post synthesis purification (washing). CO Au NP solutions range from clear ruby red to clear violet color.
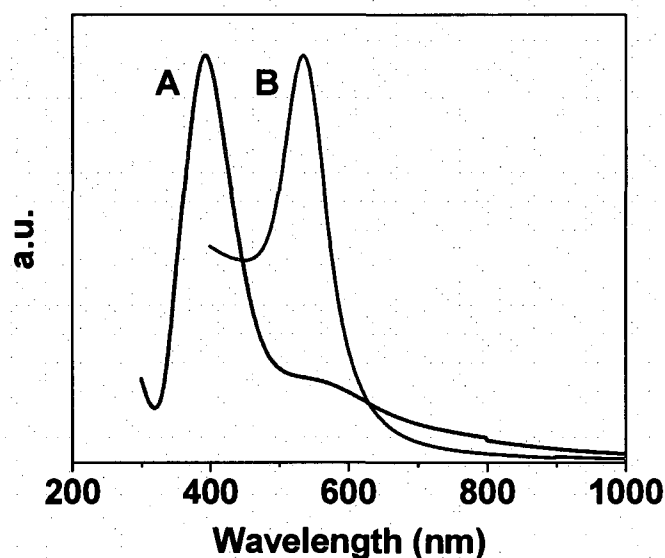
Figure 2-5 Optical absorption spectra of aqueous (A) CO Ag NP (395 nm), and (B) CO Au NP (535 nm)

In contrast to H_2CO as the reductant, the use of CO provides tunable parameters in the synthesis of Au-NP. These include the aeration rate, time and age of the plating solution. The Au products with the narrowest size distribution result when using a slow CO flow rate and a small reaction vessel. For example: place 6 ml of Au plating solution in a 13mm diameter vial and a CO flow rate of 20 sccm from a 5 mm diameter gas diffusion tube. Parameters of Ag NP synthesis have not been evaluated

2.8 Conclusion

An improved method for the growth of continuous Au shell layers on dielectric oxide nanoparticles and by a common reductant, the synthesis of Au and Ag colloid is reported. The reduction of Au^{3+} by CO results in the formation of thin, uniform shell layers on these dielectric core nanoparticles at lower Au^{3+} concentrations, where continuous shell layers are not achievable with current liquid phase reduction methods. This approach relies only on the introduction of CO(g) into the solution of prepared precursor nanoparticles and Au^{3+}, and is not susceptible to variations in shell layer morphology influenced by preparation of reductant or precursor solutions, a limitation of current shell layer growth methods. Extension of the CO reduction method to Au and Ag nanoparticles exemplifies the "general" nature of the process.

In the absence of the post synthesis purification required for other reductants, the use of CO as a reductant has transformed the manufacturing of nanoshells from a batch to a continuous flow process with potential for mass production.

Aqueous nanoshells and structured nanoparticle films will be the plasmonic substrates used to validation of Surface Enhanced Near Infrared Raman Optical Activity spectroscopy

Chapter 3. Over View of Raman Optical Activity Spectroscopy

Raman optical activity (ROA) is a vibrational spectroscopic technique that is reliant on the intensity difference between the right and left handed, circular polarized components of the scattered beam.

This chapter describes the development of a Near Infrared Raman Optical activity spectrometer (NIROAS) that overcomes the limitations of the ROA spectrometers that rely on resonant (488-532 nm) excitation lasers. The NIROAS allows for nonresonant excitation of biological analytes where the intrinsic fluorescence is minimal, and the use of NIR resonant Au nanoparticle substrates in the study of surface enhanced Raman optical activity. The reader will be familiarized with concepts of the enantiomer, chirality, and the near infrared Raman optical activity spectrometer.

3.1   Enantiomers

Molecular enantiomer(s) are commonly referred to as stereoisomers of a molecule. Complimentary enantiomers usually have common chemical and physical properties except for their ability to rotate plane-polarized light in opposite directions. [86]

Structurally, enantiomers are mirror images of each other with the caveat that one cannot be superimposed on the other. The classical real-world example of this kind of symmetry is the hand. Note that a pair-of-hands has mirror symmetry. However, one hand cannot be positioned with the other so that they are identical in all aspects from any point of view. This is illustrated in Figure 3-1.

Electronic optical activity relates to the absorption differences (electronic transitions) between right- and left-handed circularly polarized light. This is known as circular dichroism (CD). CD can have origins in both electronic activity and the secondary structure of the molecules. Molecules exhibiting CD do not necessarily exhibit ROA, which requires a chiral center nor do molecules that exhibit ROA necessarily exhibit CD.[86, 87] Notation that indicates the direction a molecule will rotate plane polarized light is (+) and (-), for clockwise and counter-clockwise respectively.

A mixture of enantiomers of equal concentration is known as a racemic mixture. Logically it follows that racemic mixtures have a net electronic and / or Raman optical activity of zero.
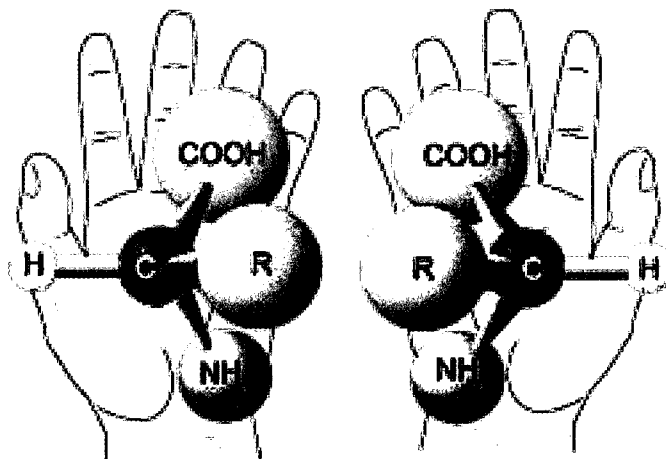
Figure 3-1. Generic amino acid Enantiomeric pair overlaid on hands

Chirality is the term used to describe the handedness. Three naming conventions are in common use. In their common nomenclature they are, (R) (rectus) and (S) (sinister), (+) and (-), and (L) and (D). Alternately, lower case (d) and (l) are used in place of (+) and (-). Capital (D) and (L) nomenclature is usually typeset in small capital

letters (L, D). The assignments of (R) and (S) are based on molecular structure and assigned a priority according to the Chan Ingold Prelog rules.[88, 89] (R) and (S) do not have a fixed relationship to either, (+) (dextrorotary) and (-) (levorotary) or (D) and (L) nomenclature. (L, D) are referenced to the molecule gyceraldehyde and based on the spatial configuration of its atoms. Indeed, a molecule possessing (S) or (R) chirality may exhibit (+) or (-) electronic optical activity.

Often ROA signals are very weak, E^{-3} E^{-6} that of Raman. If a molecule is optically active, Raman optical activity is indicated by the measurement of the intensity difference between incoherently scattered right- and left-handed circularly polarized light.

3.2 Raman optical activity

Raman optical activity in small chiral molecules was first observed by Barron et al.[22, 90] Hecht, Barron, and Hug developed a new generation of laser-based ROA instrumentation at the University of Glasgow. The new designs were based on the theory that relative to right-angle collection, the ROA signal to noise ratios of numerous ROA bands should improve significantly in the backscatter collection geometry. Hecht and Barron pointed out that under most conditions, ROA scattering intensity in the forward direction is zero, or at least the forward ROA signal is lost to isotropic scatter.[8, 13, 50] Advances including simultaneous dual channel collection, and the virtual enantiomer contributed to a systematic artifact compensation and the current state of the art Scattered Circular Polarization Raman Optical Activity Spectrometer (SCP-ROA).[7, 8, 51] An improved version of this system has since been commercialized by BioTools, Inc. Prof. Barron, the developer of the GUROAS#, purchased the first production Chiral*RAMAN*™ spectrometer. He remarked, "We have recently taken delivery of the first production model. It is around five times faster than our homemade instruments and much easier to use." [87] Fundamental concepts developed by Barron, Hug and Nafie are the basis of the NIR SCP-ROA spectrometer (NIROAS) described in this document.

3.3 Scattered Circular Polarization (SCP-ROA)

The concept of incident linear polarized light that has been circularly polarized to some degree by chiral molecules was suggested by Laurence Barron[91]. It was put forth; that the degree of circularity should not be zero when incident linear polarized light is scattered by chiral molecules.[91] This was demonstrated experimentally by Spencer et al.[5] In the case of SCP-ROA experiments, linear or preferably random polarized radiation is incident on the sample.[51, 91] Backscattered light is collected and collimated, after which it is phase modulated to produce right- and left-handed circular polarization relative to the beam incident on the sample. Historically, SCP ROA had a decisive intensity disadvantage over other ROA techniques. This ceases to be the case if the two circular components of the scattered light are measured simultaneously.[51] The Hug-Hangartner ROA design, inclusive of simultaneous dual channel collection, reduced the excitation power required to obtain a SCP signal intensity by 50% compared to previous instrument designs.[7, 51]

3.4 The Near Infrared SCP Raman Optical Activity Spectrometer

As previously mentioned, ROA measurements are the study of the right- and left-circular polarizability of chiral structures. The ratio of the intensity difference to the sum of the right- and left-handed signals is a consequence of the relative strength of the molecular electronic quadrupole, magnetic dipole and the dipole moment's interaction with an electromagnetic wave.[30] The ROA / Raman cross section is small, on the order of 10^{-3} to 10^{-6}. Complicating issues include spurious artifacts due to stray birefringence and asymmetry. Shot noise, and low frequency flicker (detection limits) have frustrated spectroscopists for decades. ROA instrumentation pioneers have devoted substantial portions of their careers to understanding and eliminating these deceptively genuine looking spectral artifacts
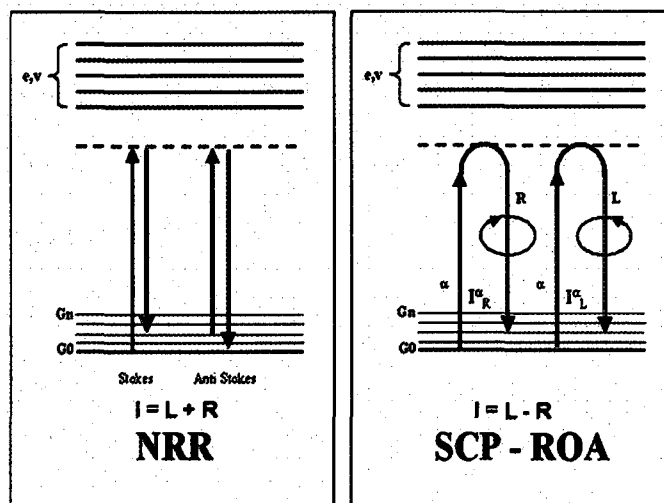
Figure 3-2 Nonresonant Raman and scattered circularization Raman optical activity energy diagrams

48

Like classical Raman spectrometers, the ROA systems illuminate the sample with near field monochromatic coherent light, e.g., a focused laser beam. The fundamental difference from other Raman systems is that ROA systems interrogate a sample by monitoring the change in the degree of polarization, relative to the incident beam and thus, the optical coupling difference between right- and left-handed Raman optically active modes. The energy flow diagrams in figure 3-2 illustrate the difference between the measurements of Raman and ROA. Both processed occur simultaneously. Intensities, of the circularly polarized component, relative to Raman signals are small, on the order of E^{-3} to E^{-6}. This is why systematic birefringence, at levels often imperceptible by conventional polarization analysis techniques, can dominate an ROA spectrum. On a scale for phase shift in materials considered isotropic, even high quality fused silica can elevate the background to a level that obscures the ROA information.

3.5 ROA Spectrometer Design

The near infrared Raman optical activity Spectrometer (NIROAS) is based on the design of the Chiral*RAMAN*™ spectrometer. Principle changes to the instrument design are the incorporation of NIR Laser, optimized optical components and software enhancements. All of the optical elements are commercially available. Advances in machine control electronics, digital signal processing (DSP), and the user interface developed by Dave Rice et al. (Critical Link, LLC), have greatly reduced acquisition time and improved the ease of use. During the development of the NIROAS numerous upgrades have been made to the original ROA application (Brinson and Rice). Many of the upgrades will be transparent to the user while others provide additional tools and diagnostic capability. The reader is referred to the NIROAS user's manual in Appendix II for information supporting the following discussion.
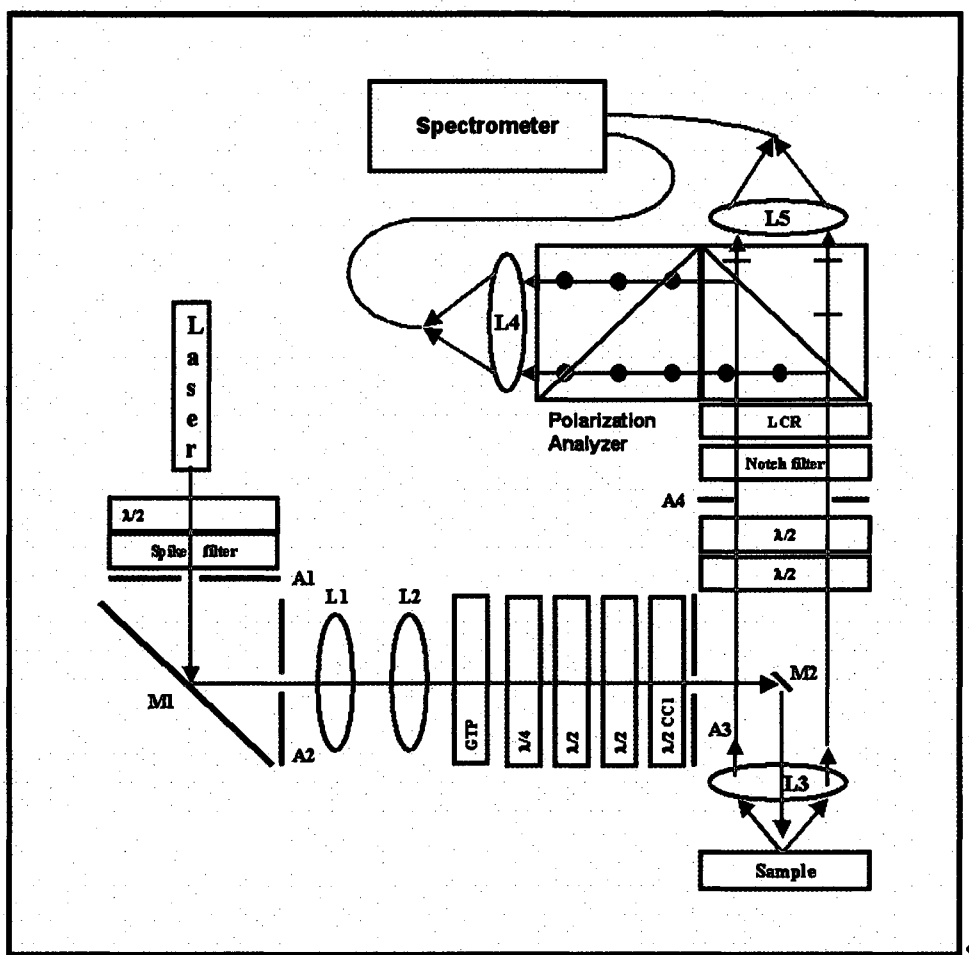
Figure 3-3 Schematic of the near infrared excited scattered circularization polarization Raman optical activity spectrometer.

The incident light path

Referring to Figures 3-3, 3-4: The NIROAS excitation laser is a wavelength tunable laser diode Littrow oscillator / tapered amplifier configuration rated at 1.4 watts of optical power at 780 nm. (Sacher Lasertechnik, Inc.) The laser is equipped with an internal faraday rotator, is followed by a $\lambda/2$ plate (Melles Griot) and a laser line (780 nm, FWHM 5nm) spike filter (CVI)

The incident beam shutter (NM Laser Products), positioned in the confocal plane between L1 an L2, is followed by a Glan-Thompson Polarizer (GTP) (ThorLabs),

To deliver a randomly polarized excitation, two counter rotating zero order $\lambda/2$ plates (Halle, Berlin, Germany), referred to as *linear rotators* (LR1 and LR2), are positioned between the Glan-Thompson polarizer and the sample.
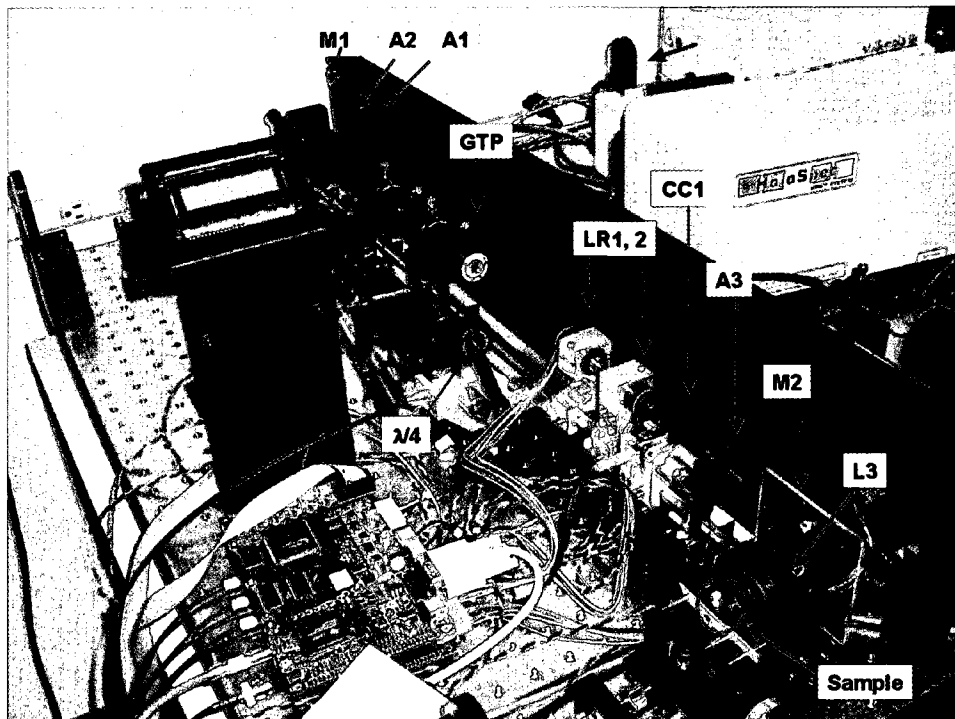
Figure 3-4. Optical components of the NIROAS incident light rail

The incident beam is turned by a second periscope mirror set (M2), after which it is focused onto the sample. Scattered light is collected, and transformed to the far field, by; an ultraviolet light grade, fused silica, +30 mm, F1, aspheric objective lens (Archer OpTx, Inc.).
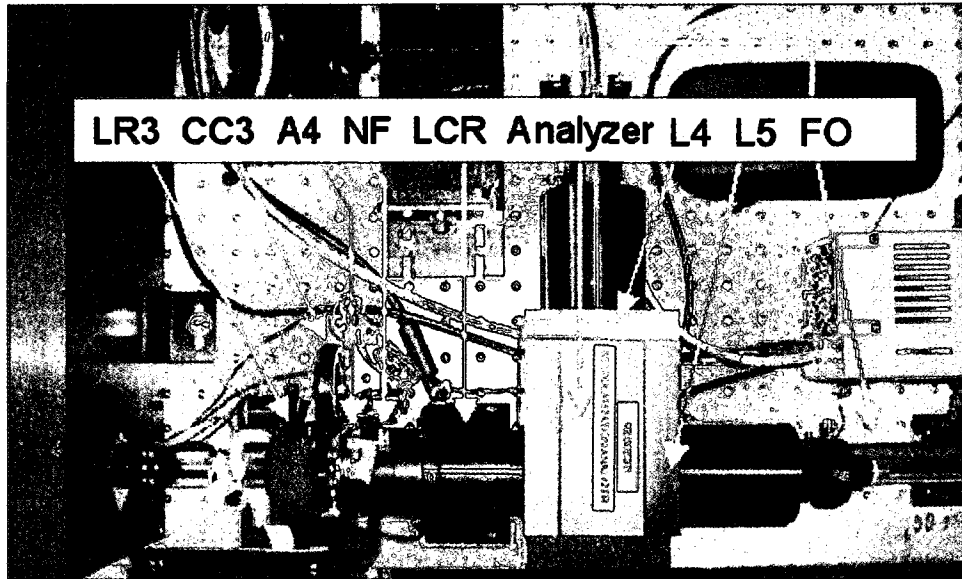
Figure 3-5 Optical components of the NIROAS scattered light rail.

The scattered light path

Referring to Figures 3.3 and 3.5: Scattered light is collected by the objective lines and transmitted through a rotating 30 mm diameter zero-order $\lambda/2$ plate (LR3) (CVI Inc.). LR3 has a constant phase shift for circularly polarized light. Thus, the CID experiences concurrent sign changes while linearly polarized light intensities are time averaging. LR3 is followed by a 780 nm notch filter (OD 5.5, FWHM 10 nm) (Kaiser Inc.), and a Liquid Crystal Variable Retarder (LCR) (Meadowlark Optics). The LCR behaves as a dynamic quarter waveplate that can be rapidly switched (<50 mS) to produce a $\lambda/4$ and $3\lambda/4$ ($-\lambda/4$) phase shift. The LCR is that it converts incident right- and left-handed circularly polarized light into S and P linearly polarized light. Unique to the NIROAA is the integrated assembly that includes the notch filter, LCR, polarization analyzer, L4 and L5, and the FO coupler. This arrangement simplifies assembly and serves to protect

fourteen (10) surfaces from atmospheric contamination. Scatted light from the S and P arms are subsequently coupled to the spectrometer and incident on upper and lower halves of the CCD array.

ROA spectra of Phenylethylamine
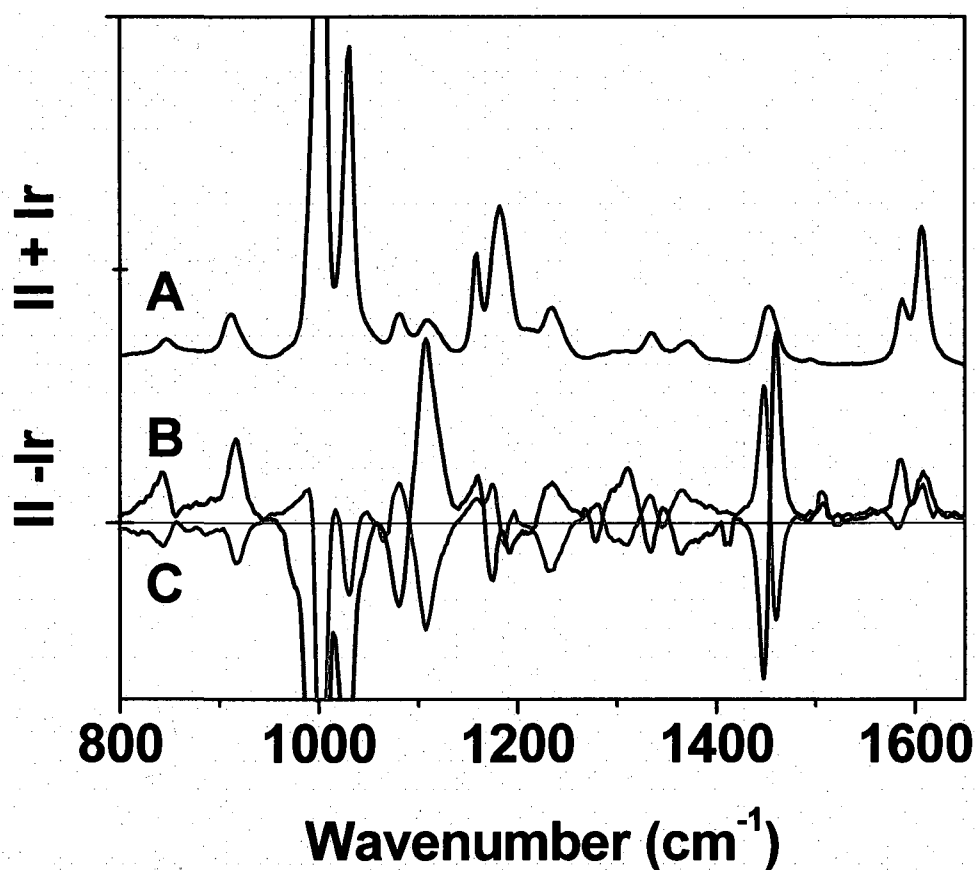
Figure 3-6. Phenylethylamine Raman and ROA spectra.
(A) Scaled and offset Raman, (B) (S)-phenylethylamine ROA, and (C) (R)-phenylethylamine ROA spectra recorded by the NIROA spectrometer.

Phenylethylamine is a bright ROA molecule exhibiting well-defined vibrational modes. The Raman and complimentary ROA spectra of phenylethylamine are shown in Figure 3-6. Collection of E^{10} counts @ 1000 cm^{-1} required 500 mW @ 780 nm of excitation power and an exposure period of 180 minutes.

The ROA spectra exhibit mirror symmetry across the spectrum including regions where the Raman spectrum is featureless. Recalling the ROA cross-section can be E^{-3} to E^{-6} of the Raman cross-section, the point to be carried forth is that ROA vibrations produce very weak signals relative to the parent Raman spectra, but can be resolved by the NIROA spectrometer.

Advances in Software

The software used for the Chiral*RAMAN*™ spectrometer has been extensively adapted and upgraded for the NIROA spectrometer. Challenges included spectral artifacts induced by cosmic rays, scattered light intensity variations, lost data files, and the inability to precisely monitor Raman intensities and peak ratios during a scan.

The cosmic ray issue was resolved by a real time spectral analysis routine, which discards and replaces data that includes a pixel column intensity significantly greater than the two adjacent pixels. The discard threshold is user defined.

The scattering intensity of NP film SERS samples can increase and decrease over time due to photochemical stimulation or decomposition. This also applies to aqueous SERS samples with limited suspension life times. A plotting routine incorporated into the user-interface, displays six real-time plots, inclusive of absolute intensity, S/N ratio, and peak-to-peak ratios. Applications include time-resolved experiments, monitoring

photochemical decomposition, molecular conformation changes and instrument diagnostics.

Until now, scattered light intensity variations induced by the virtual enantiomer artifact compensation system have been ignored. Concurrent with the polarization artifact cancellation scheme, four sets of eight difference spectra are digitally processed. The CID differenced within the eight scans in each state will be constant, but the absolute difference in counts between states will not be constant. The *Path Correction* code has been modified to compensate for the discrepancy based on the parent spectra. The new path correction coefficients are updated at the end of each set of 32 scans.

Numerous modifications, transparent to the user, enhanced the software stability and ease of use. The reader is referred to Appendix II for additional details.

The SX stage: a Solution to the Repeatability Challenges of SERS

Historically, due to the extreme sensitivity of the SERS measurement, the SERS spectra suffered from a lack of reproducibility SERS elucidate genuinely representative SERS spectra, the instrument and user time intensive *step and repeat* approach is often employed (Figure 3-7 a). This technique often involves collecting tens of spectra from as many locations, and post processing by methods ranging from signal averaging to statistical probability calculations.[44, 92] Additionally, the *step and repeat* technique requires continuous irradiation of each probed location, therein a higher probability of photochemical modification or decomposition prevails.
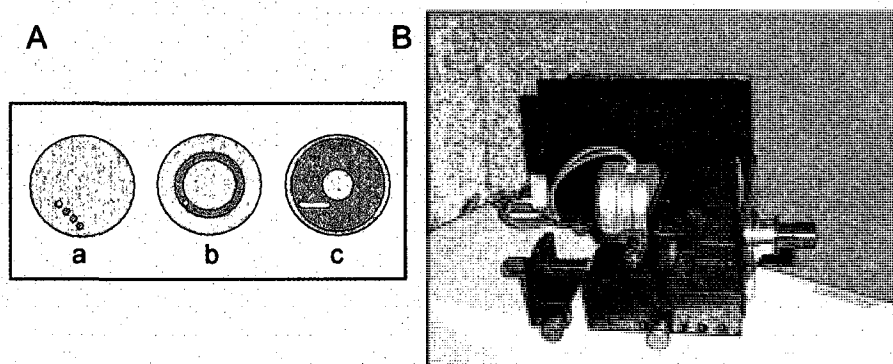
Figure 3-7. The SX Stage
(A) the areas sample by (a) step and repeat, (b) rotation, and (c) rotation and translation of the sample. Violet shading highlights the interrogation area. (B) Photograph of the SX stage.

We have developed a stage to hold and move the sample that alleviated some of the issues with the exposure of a small area of the sample for extended times. The SX Stage, Figure 3-7B, rotates a ½" or 1" diameter solid-state sample at 250 RPM (Figure 1b), and / or translates the sample perpendicular to the spectrometer's optical axis (Figure 3-7c). This provides for sample averaging over large areas and higher laser power. For example, given a beam waist $(2\omega^0)$ of 100 μm and a rotation radius of 1 mm, scattered

57

light from 62.5 times the single point area contributes to the spectra. Relative to *step and repeat*, higher excitation power can be used when the SX stage is implemented.

Conclusion

The near infrared excited Raman optical activity spectrometer has been constructed and qualified by the collection of ROA spectra from enantiomers of phenylethylamine and α-pinene (not shown). In the following chapter, the NIROAS, and plasmonic nanoparticle substrates will be used to determine the merits of nonresonant surface enhanced Raman optical activity spectroscopy.

Chapter 4. Nonresonant Surface Enhanced Raman Optical Activity

4.1 Introduction

Thus far, Raman optical activity, plasmonic nanostructures, and the NIROAS have been discussed. In this chapter, these concepts will be combined with descriptions of analytes, sample preparations, and SEROA experiment.

Symmetrical CID spectra were collected from the enantiomers of tryptophan, and amine-terminated phenylalanine-cysteine-glycine-glycine (phe-cys). SEROA sample structures consisted of analyte functionalized, three dimensional, aggregated Au nanoparticle films. After the analyte, instrumentation, and the sample structures are presented, the experimental results will be discussed

Nonresonant SEROA has been validated by the display of mirror symmetry circular intensity difference spectra. SEROA modes have been elucidated from spectral ranges were the SERS S/N ratio approaches 1. (Section 4.3.3) A particularly strong argument will be demonstrated for the tryptophan functionalized NP film.

4.2 Experimental: Materials, Methods, and Calculations

4.2.1 Analytes

The stated purity of all analytes was $\geq$ 98%. All analytes were used without further modification. Powder (S)- and (R)-tryptophan, and liquid (R) and (S) α-pinene were purchased from Sigma-Aldrich. Powder (SS)- and (RR)-phenylalanine-cysteine-glycine-glycine(S) oligomer were synthesized by aaddtec™, Inc. Liquid phenylethylamine was purchased from TCI America. Water (18 MΩ) was supplied by a Milli-Q™ purification system. Au nanoparticle synthesis and common laboratory chemicals were previously described in Chapter 2.

4.2.2 Instrumentation

Optical absorption spectra of aqueous samples in either a 1 cm path length polystyrene (Fisher Scientific) or quartz (Sterna) cuvette, were collected using a Varian Cary™ 5000 UV-VIS-NIR scanning spectrophotometer. These measurements confirmed equivalent concentrations of the stock solutions. **Optical extinction** spectra were collected from NP films and aqueous NP.

Circular dichroism spectra of aqueous control solutions and dry NP film samples was collected using a Jasco J810 Spectropolarimeter, or similar instrument, fitted with either 10 mm path length quartz cuvette (Sterna) or a custom mount for film samples.

Nonresonant vibrational spectra (aqueous 780 nm) including Raman, ROA, SERS and SEROA were collected by the NIROAS. The NIROAS optical alignment and electronic calibrations were optimized monthly, as described in Appendix 2. A

microscope equipped a 50x or 63x objective lens, and 780 nm excited Renishaw InVia™ Raman spectrometer was used to collect vibrational spectra from as delivered analytes, and from functionalized NP and NS films on PVP coated quartz substrates.

Scanning electron microscopy (SEM) micrographs were collected using an FEI Quantum 400 SEM operated in the high vacuum or ESEM mode.

4.2.3 Analyte Characterization

Enantiomer chemical equivalencies were verified by optical absorption (OA), circular dichroism (CD), Raman, and SERS spectroscopy. Mass spectrometry (MS) and high performance liquid chromatography (HPLC) data were provided by the vendor, aaddTek™, (data not shown).

Optical Absorption Spectra Equivalent concentrations of stock solution were confirmed by optical absorption spectra Equal amounts of the analytes, by weight, were dissolved in water. Serial dilution sets made from the stock solution(s), were extended in water until the optical density across the wavelength range of 250 - 280 nm, was observed within the optical density range of 0.2 to 1. Molecular concentration was determined by the Beer-Lambert law (Equation 4-1). Absorption data not will not be shown.

$$C = \frac{A}{\alpha L}$$

Equation 4-1 Beer-Lambert law

where: A is the measured absorbance, α is the absorption coefficient, and L is the cell path length (cm). Absorption coefficients applied in these experiments were: Tryptophan

5610 $M^{-1}cm^{-1}$ @ 278 nm, and Phenylalanine 195 $M^{-1}cm^{-1}$ @ 257 nm or 144 $M^{-1}cm^{-1}$ @ 260 nm.

Circular Dichroism CD measurements verified 1) electronic activity sign symmetry of the analyte solution, and 2) retention of molecular chirality when bound to a plasmonic substrate. The analytes are monomer tryptophan and phe-cys-gky-gly. Since there is no secondary structure of the analytes probed, any observable sign changes in the CD spectra are due solely to molecular chirality.

Vibrational Spectroscopy Raman and SERS data were compared to verify common vibrational modes of the analytes, and thus, common molecular structure. For enantiomer pairs, Raman and SERS spectra were respectively by reasonable approximation, equivalent.

ROA ROA calibration spectra were collected from as delivered (S)- and (R)-phenylethylamine, Signals from saturated cysteine, phenylalanine, and tryptophan were too weak to be measured.

4.2.4 Film Sample Preparation

An Au NP suspension was prepared by reducing 40 mL of potassium carbonate (K-carb solution) with 250 µL of formaldehyde (H_2CO), followed by centrifugation of the particles (2500 RCF, 10 min.) and redispersion in 2 mL of water.

A schematic of the sample development process is shown in Figure 4-3A. SEM Micrographs of the NP film structures are shown in **Figure FY A**

150 µL aliquots of the dense NP suspension were deposited onto 0.5" diameter, PVP coated fused silica substrates. The NP films were not allowed to dry. Immediately before analyte functionalization, the NP film was gently rinsed with water and dried with filtered N_2.

Aqueous 50 µM analyte solutions were deposited on the NP films and allowed to incubate overnight. The samples were gently rinsed with water and dried with filtered N_2. To ensure molecular monolayer coverage of a second layer of nanoparticles, in a 15 mL centrifuge tube, the applicable analyte was added in excess to a 2 mL aliquot of the dense aqueous NP suspension. The solutions were allowed to incubate overnight. The functionalized NPs settled at the conical bottom of the vial. The supernatant was decanted, followed by gentle redispersion of the functionalized NPs in water. The NPs were allowed to settle to the bottom of the vial.

The film substrates were gently rinsed with water and dried with filtered N_2. 150 µL of the functionalized particles were then deposited onto the functionalized NP film. Tryptophan samples were allowed to dry, then gently rinsed with WATER and dried with filtered N_2. A SEM micrograph representative of analyzed samples is shown in Figure 4-5.

Phe-cys samples were allowed to incubate for three hours, gently rinsed with water and dried with filtered N_2. An SEM micrograph representative of analyzed samples is shown in **Figure 4-1 C.** All samples were isolated and stored in an N_2 environment before use.
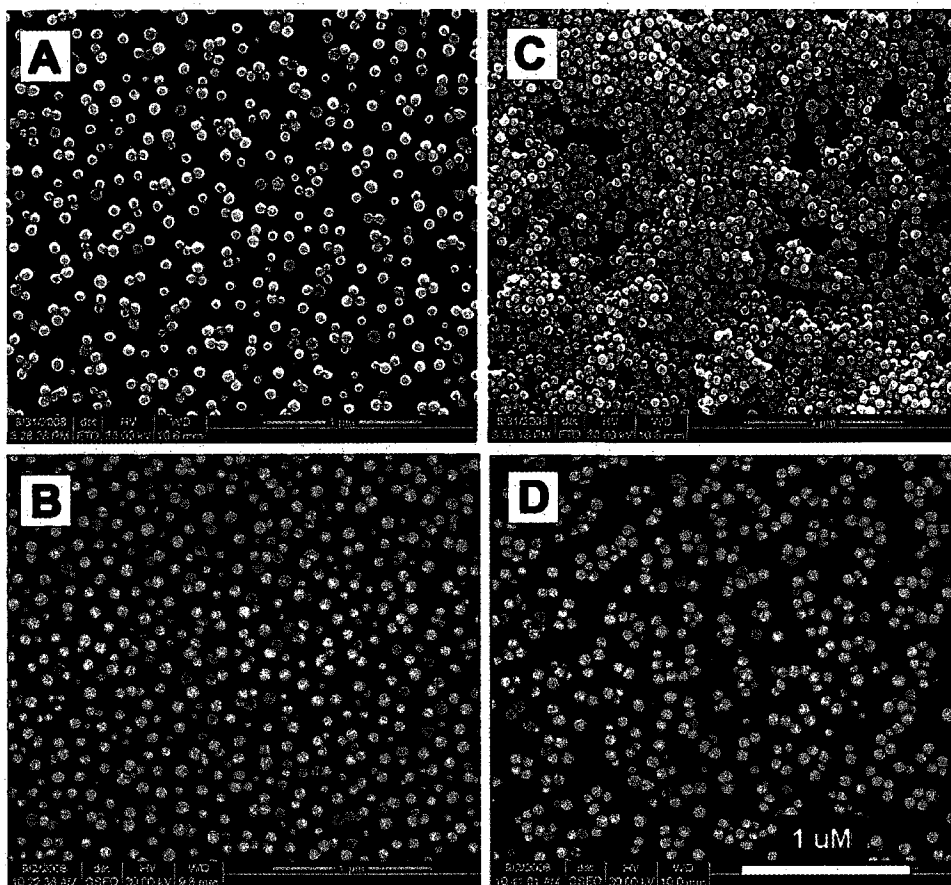
Figure 4-1 SEM images of Au NP films.
(A) Analyte functionalized NP dense NP film, (B) thin NP film (C) 3D film after the overnight deposition of phe-cys functionalized NP, onto (A), and (D) 2D NP film after a one-hour deposition of phe-cys functionalized NP onto (B). All scale bars are 1 μm.

4.3 Nonresonant Tryptophan SEROA

Tryptophan is one of 20 standard amino acids and an essential amino acid in the human diet. Tryptophan is distinguished from other amino acids by the presence of the *indole* functional group.[93] In this section, samples consisted of a 3D Au nanoparticle film functionalized by monomer tryptophan molecules. The samples were characterized and evaluated for evidence of SEROA. Clear circular intensity differences were observed and correlated with the parent Raman and SEROA spectra. Significantly, the diagnostically important[21, 94] indole W3 ROA peak at 1550 cm^{-1} was elucidated from a nearly featureless background.
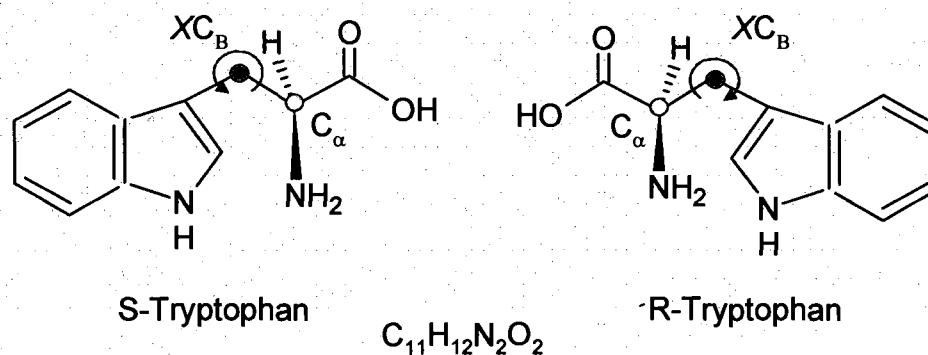
Figure 4-2 Chemical structures of (S)- and (R)-tryptophan with the chiral centers (C_a) indicated in red and the torsion center (XC_B) indicated in blue.

Characterization of Tryptophan samples

The order of sample assembly and final structure are illustrated in Figure 4-3A. The NP film extinction profile includes the NP plasmon resonance peak at 520 nm, and a broad aggregate resonance peak in the NIR region (Figure 4-3B). Interestingly, this extinction profile is ideal for a direct comparison of nonresonant and resonant SEROA. A comparison of the control solution and functionalized NP film CD spectra confirms the presence of the analyte on the NP film and the retention of chirality while bound to a metal surface (Figure 4-4). The 3D morphology of the samples was confirmed by SEM. (Figure K2).
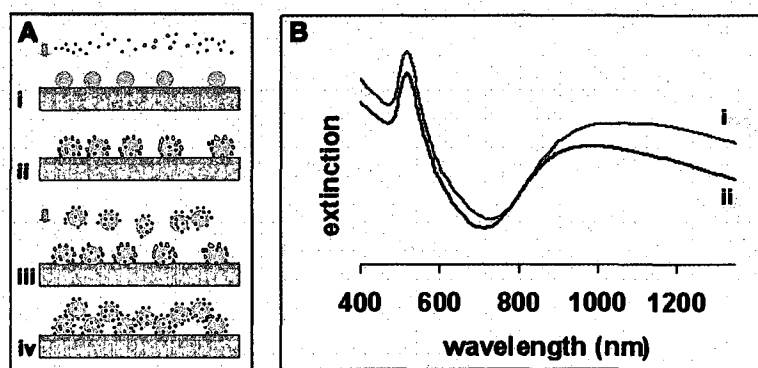
Figure 4-3 Tryptophan nanoparticle sample morphology and extinction spectra.
(A) Tryptophan SEROA NP film assembly order: (i, ii) functionalization of a NP film, (iii) deposition of functionalized NPs, and (iv) final 3D NP aggregate film structure. (B) Optical extinction spectra of (i) (R)-tryptophan and (ii) (S)-tryptophan, which include both NP and NP aggregate peaks.
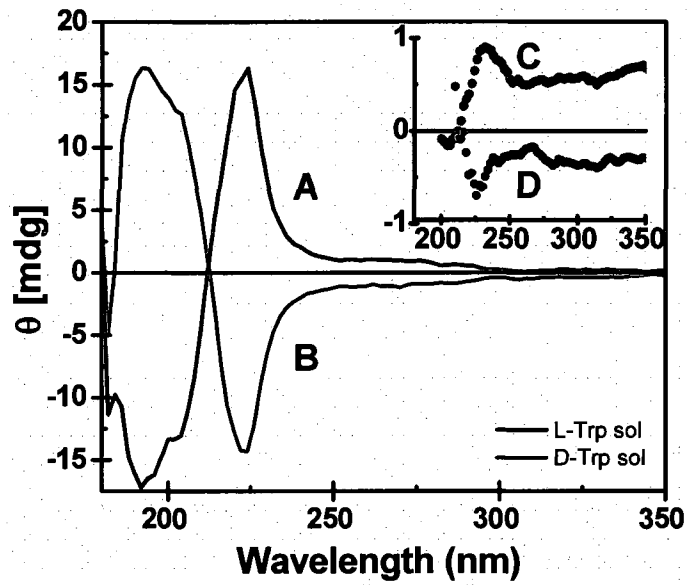
Figure 4-4 Tryptophan circular dichroism spectra.
(A) aqueous (S)-tryptophan and (B) aqueous (R)-tryptophan. Inset shows the circular dichroism spectra of a (C) (S)-tryptophan nanoparticle film and (D) (R)-tryptophan nanoparticle film.
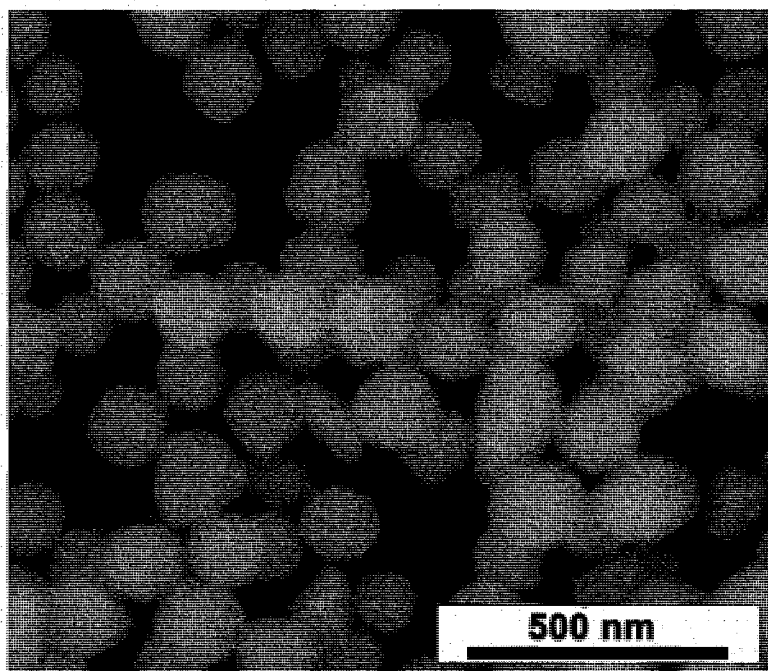
Figure 4-5 A SEM image of a 3D-tryptophan nanoparticle film

Experimental

SEROA and SERS spectra were collected simultaneously. Spectra were collected at three randomly chosen locations on each substrate. Instrument conditions included a laser power of 18 mW @ 780 nm and a cumulative exposure time of 20 minutes. A total of 3.4×10^8 SERS counts @ 1350 cm^{-1} were collected, with a SERS S/N ratio of 1.1 and SEROA CID of E^{-3}.

Shown in Figure 4-6 are scaled, tryptophan Raman and -NP SERS spectra and raw (S)- and (R)-tryptophan SEROA spectra. Relative to the ROA, the scan parameters are considered very low numbers, yet the SEROA spectra did appear quickly and clearly.
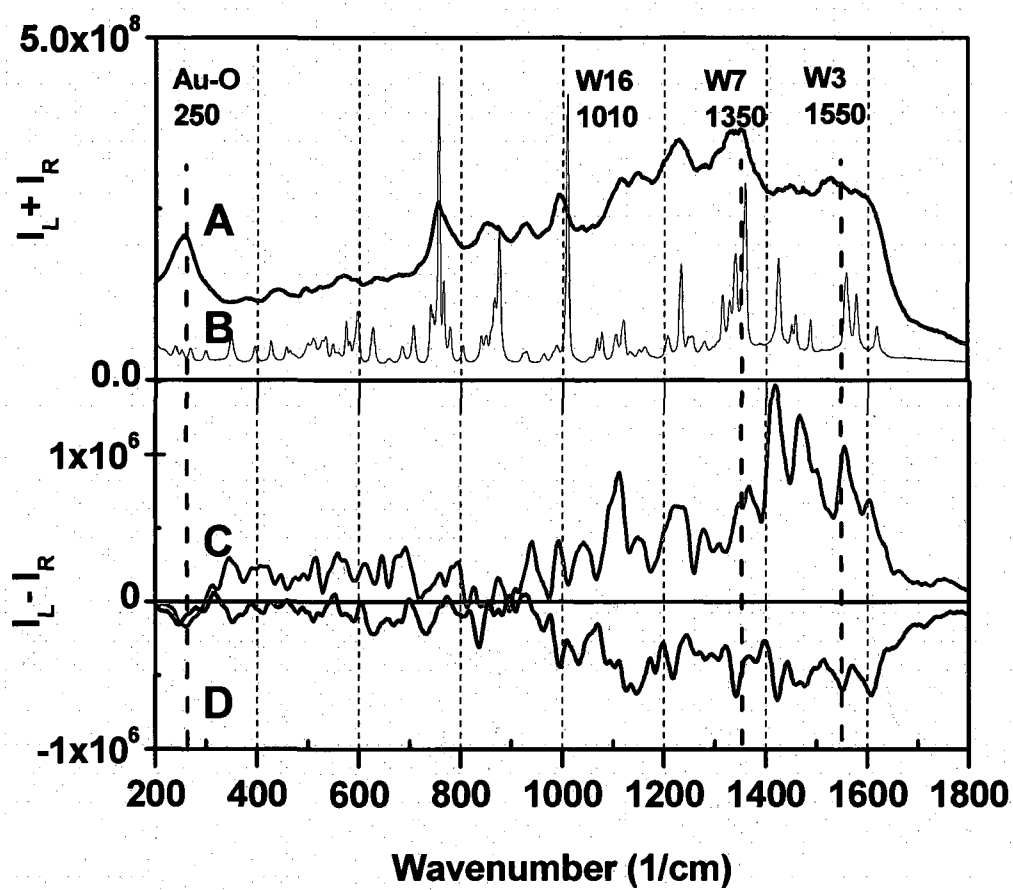
Figure 4-6 Tryptophan SEROA, SERS, and Raman spectra.
(A) SERS, (B) unenhanced powder Raman, (C) (R)-tryptophan SEROA, and (D) (S)-tryptophan SEROA spectra.
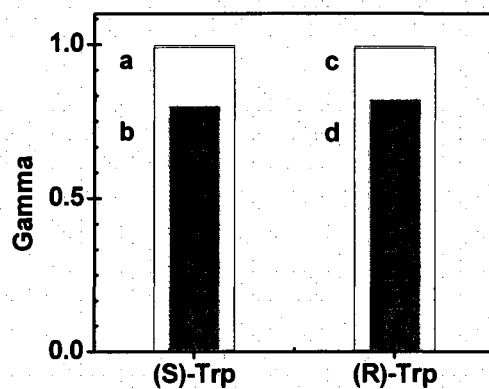
Figure 4-7 Gamma, the statistical probability of spectral repeatability
is calculated for three (R)- and (S)-tryptophan SERS and SEROA spectra. Gamma values
for (a) (S)-tryptophan SERS, (b) (S)-tryptophan SEROA, (c) (R)-tryptophan SERS, and
(d) (R)-tryptophan SEROA

Discussion

Vibrational modes observed in the SERS and SEROA spectra are coincident with Raman peaks and peak manifolds in the spectra of neat tryptophan. (Figure 4-6) A 5-point rolling average has been applied to the SEROA spectra to smooth high frequency noise. Mirror symmetry was clearly observed in the SEROA spectra between 900 and 1600 cm^{-1}. Below 900 cm^{-1} both symmetry and asymmetry were observed. The lower region exhibits significantly less symmetry in the high frequency regime, however, as illustrated in the ROA spectra of phenylethylamine (Figure 3-6), symmetry is observed across the spectral baseline. The peak at 250 cm^{-1}, is present in both the SERS and SEROA spectra but not present in the neat Raman spectra. This peak has been assigned to a linear Au-O bond[95]. The significance of this peak is that both SEROA spectra share a common sign and amplitude.

Gamma (Γ) calculations[44], the statistical probability that multiple spectra are equally representative of the analyte, returned $\Gamma = 1$ for the SERS spectra, while both SEROA spectra returned $\Gamma = 0.8$. (Figure 4-7) These high and equivalent values are indicative of consistent molecular conformation on the NP surface.

Attributes of conventional ROA and recently published resonant SEROA spectra are observed in the nonresonant SEROA spectra.[96] The SEROA peak resolution exceeds that of the SERS. Exclusive and inclusive of the signed plasmonic substrate background, the (S)-tryptophan and (R)-tryptophan SEROA CID was E^{-3}, which is comparable to high quality ROA and silver aggregate SEROA spectra.[96] These attributes suggest that in this experiment, the nonresonant SEROA cross section is comparable to resonant ROA and SEROA experiments.[14]

Clearly defined SEROA modes coordinate well with the Raman spectra in places where the SERS S/N ratio approaches one. Excellent examples are observed in the amide II region between 1400 and 1600 cm^{-1}. These include weak CH_2 and CH_3 deformations between 1400-1480 cm^{-1} and the biologically significant Raman and ROA marker at 1550 cm^{-1}.[94]

The most interesting observation is the SEROA indole ring W3 vibration at 1550 cm^{-1}.[94] The W3 vibration is indicative of the torsion angles about the XC_β atom on the tryptophan backbone. (Figure 4-1) This peak is clearly defined in the Raman and SEROA spectra, but very weak in the SERS spectra. This peak contributes to the determination of the absolute stereochemistry of a tryptophan residue. It can also be the sole and very weak Raman and ROA marker for tryptophan side chains in filamentous bacteriophanges.[21, 94] In a recently published theoretical tryptophan study, Jacob and Reiher placed the strongest tryptophan ROA peak *ca.* 1540 cm^{-1} and attribute the precise peak location to the torsion angle about the C_β position on the tryptophan backbone $(C_2 = C_1 - C_\beta - C_\alpha)$. This is illustrated in **Figure 4-1**.[97,94] Combined with information from the orthogonally coupled in plane W7 amide III peak *ca.* 1350 cm^{-1} mode, the exact stereochemistry of the tryptophan residue in complex molecules can be determined.[21, 98]

Conclusion

The observation of symmetry and asymmetry, where they are expected, and the elucidation of the W3 vibration at 1550 cm^{-1} bring validity to nonresonant surface enhanced Raman optical activity spectroscopy. Significantly, the 250 cm^{-1} mode attributed to linear Au-O bonding, is equal in both sign and magnitude i.e., perfectly asymmetrical. With these attributes, the 250 cm^{-1} peak is an internal symmetry reference point.

The SEROA spectra include the mirror image of the plasmonic substrate photoluminescent background. A plausible explanation is that SERS substrate photoluminescence includes a circular intensity difference, influenced by the chirality of the analyte. This implies that binding tryptophan to the Au surface has induced chirality at the particle surface and broken the Au d-band symmetry. Furthermore, the sign of the asymmetry is dependent on the chirality of the conjugated molecule. This is a phenomena that and merits further investigation.

Raman	SERS -SEROA	SERS FWHM	Assignement	ref
cm^{-1}	ri	cm^{-1}	comment	
254	s	50	Au-O	6
380	vw	25		
431	w			
442	w	30		
495	w	10		
533	vw			
570	m			
637	w		COO⁻ Wag bk bone	2
670	vw		sym Breath, W18	1, 2
776	s	30		
853	w	40		
875	w			
930	m	30		
995	s	30	ip asym W1	1, 2
1050	vw		W16	
1117	w	15		
1140	vw	20	NH_2 def.	2
1228	s	50	Ip W7	1
1306	w		Ip W7	1
1347	s	60	NH_2 def. W7	2, 3
1450	w			
1540	m	40	Ind W3	4, 5
1578	vw			3

Table 1. Tryptophan Raman, SERS, and SEROA peak assignments.

Ref 1[99], ref 2[100], ref 3[101], ref 4[21], ref 5[97], ref. 6[95].

74

4.4 Nonresonant Phenylalanine-Cysteine SEROA

A logical step following the successful tryptophan SEROA experiment is to advance the technique to molecules of greater complexity. Phenylalanine is an essential amino acid and a component of the controversial artificial sweetener, aspartame.[102] Roles of phenylalanine in the human body range from feelings of well-being to a diagnostic marker for the diagnosis of phenylketonuria.[103] Gamma (Γ), is the probability that multiple nonidentical spectra are genuinely representative of an analyte. Γ is the average of off diagonal cross correlation coefficients, determined between spectral pairs. Recently, Wei and Hartgernik reported a phe-cys SERS $\Gamma = 0.95$.[104] Based on the biological significance and high level of SERS repeatability, phe-cys was selected as the analyte for the second phase of the SEROA validation experiments.

By design, shown in Figure 4-8, the amino acid sequence (SS)- and (RR)-amine-terminated phenylalanine-cysteine-glycine-glycine (phe-cys) provides an S-Au bond and a spacer for the phenylalanine molecule. As a molecular monolayer on a gold surface approaches saturation, S-Au bonds are expected to displace N-Au bonds. The result is an energetically favorable amine-terminated surface, where the packing density limits the number of molecular surface conformations.

In this section, 3D Au nanoparticle films functionalized by the phe-cys oligomer are evaluated. Clear evidence of signed circular intensity differences that correlate with the parent Raman and / or the SEROA spectra were observed. Gamma calculations returned: SERS $\Gamma = 1$ for both analytes, and SEROA $\Gamma = 0.36$ and 0.43 for (RR)- and (SS)-phe-cys respectively. The difference was attributed to the greater complexity of the

phe-cys-gly-gly molecule, which could result in a broader distribution of molecular orientations on the nanoparticle surface.

Characterization of phenylalanine-cysteine
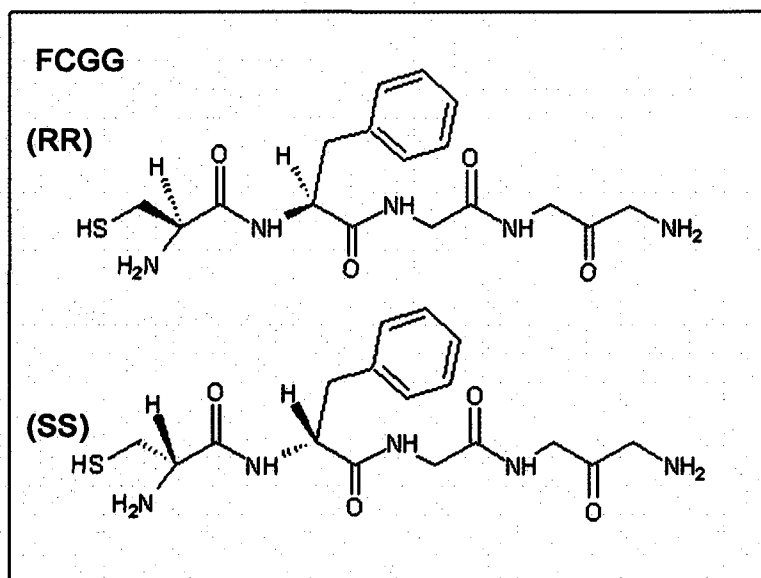
Figure 4-8. Chemical structure of amine-terminated (SS)- and (RR)-phenylalanine-cysteine-glycine-glycine.

Phe-Cys Conjugation Kinetics

In the case of a saturated monolayer, the SH⁻ group is expected to displace N-Au bonds. This results in an amine-terminated surface. When additional Au or phe-cys functionalized particles are added to the sample, molecularly bound aggregates are expected to form as illustrated in Figures 4-9 and 4-10.

To confirm the molecular binding of NP on film substrates, a study of aqueous NP aggregation by phe-cys was conducted. When phe-cys was combined with CO-Au-NP suspensions, the samples immediately began to change color from red to pink to

violet and continued to darken. The initial tint of the sample (pink to dark purple) is dependent on the phe-cys concentration. The final tint was both molecule and particle concentration dependent. The color change indicates a plasmon red-shift and therefore, NP aggregation. Because NPs are condensed in suspension for these experiments, it is impossible to know the NP density and the repeatability of the aggregate plasmon resonance was low. None-the-less the trend is consistent. The rapid aggregation of NPs into colloids, that remain suspended in solution, implies molecular binding of the NP by both functional groups and an amine-termination of exposed NP surfaces. The molecular dimer model is illustrated in Figure 4-9.
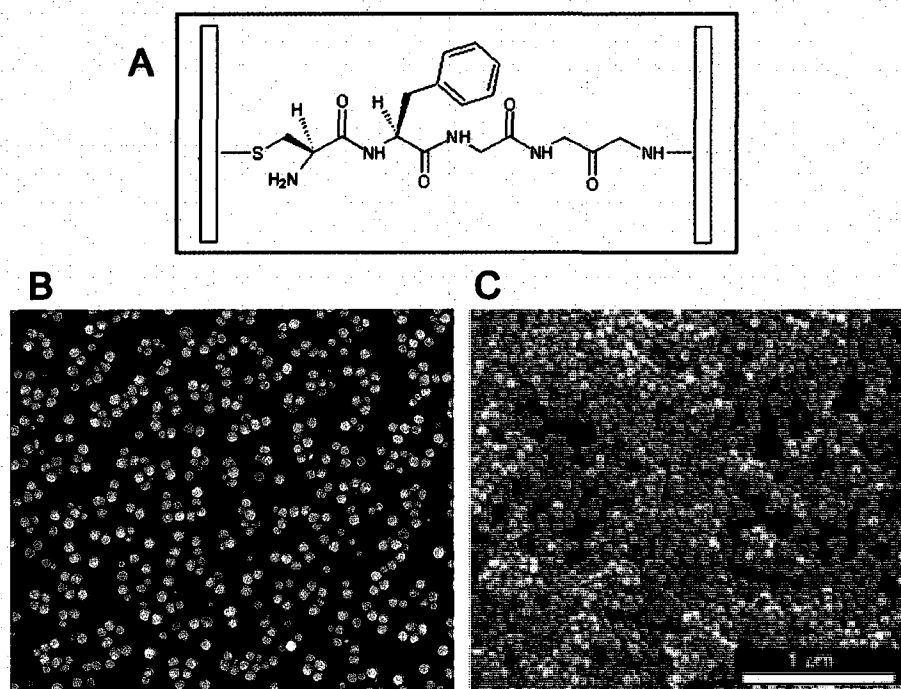
Figure 4-9 Schematic of a phe-cys in dimer junction and SEM images of nanoparticle films.
(A) Schematic of a phe-cys in a dimer junction. SEM images of nanoparticle films. B) before, and C) after phe-cys functionalization followed by deposition of phe-cys functionalized NPs.
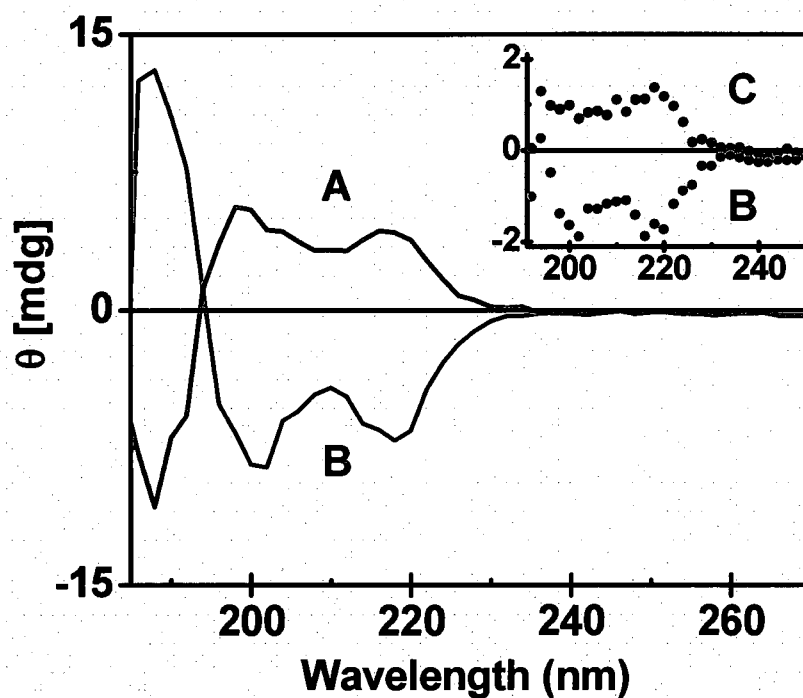
Figure 4-10. Phenylalanine-cysteine circular dichroism spectra.
(A) aqueous (SS)-phe-cys, (B) aqueous (RR)-phe-cys. The inset shows the circular dichroism spectra of a (C) a (SS)-phe-cys functionalized nanoparticle film, and (D) a (RR)-phe-cys functionalized nanoparticle film.

Experimental

SEROA and SERS spectra were collected simultaneously. Spectra were collected at three randomly chosen locations on each substrate. Instrument conditions included a laser power of 20 mW @ 780 nm and a cumulative exposure time of 120 minutes. A total of E^{10} SERS counts @ 1000 cm^{-1} were collected, with a SERS S/N ratio *ca.* 3.
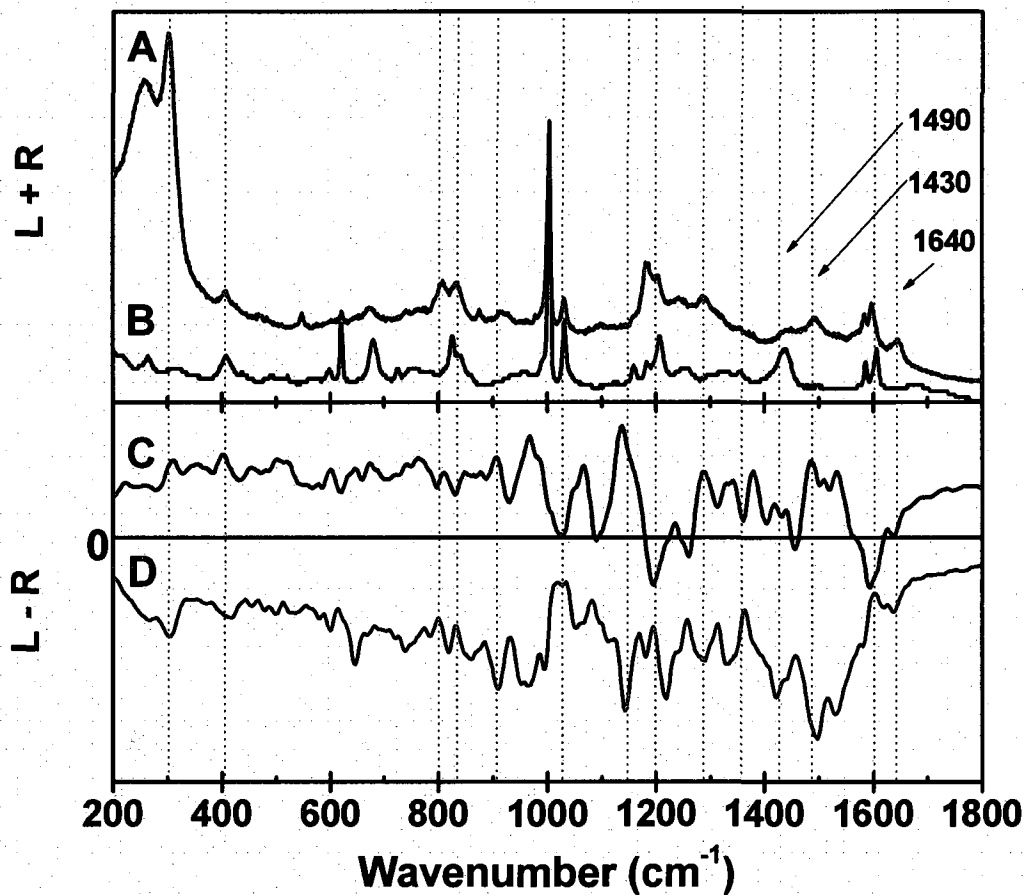
Figure 4-11. Averaged spectra SERS, Raman, and SEROA phe-cys spectra.
(A) (S)-phe-cys SERS, (B) Raman spectra of crystalline phe-cys, (C) SEROA spectra of
(SS)-phe-cys, and (D) SEROA spectra of (RR)-phe-cys. SEROA peaks possessing mirror
symmetry and correlation are indicated by dotted lines.
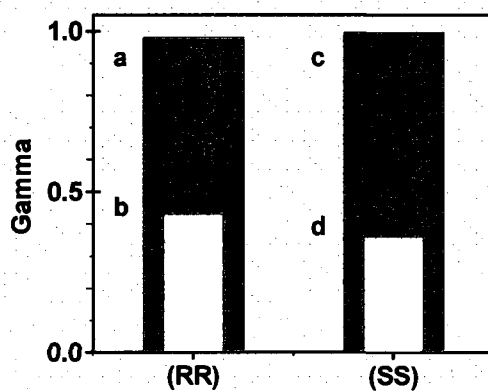
Figure 4-12 Gamma, the statistical probability of spectral repeatability.
Gamma calculated for three (RR)- and three (SS)-phe-cys SERS and SEROA spectra.
Returned values were: (a) (RR)-phe-cys SERS, (b) (RR)-phe-cys SEROA, (c) (SS)-phe-cys SERS, and (d) (SS)-phe-cys SEROA

Discussion

Circular dichroism measurement of control solutions and the functionalized NP films are shown in Figure 4-11. The mirror symmetry and line shape confirm the presence of the phe-cys analytes on the NP film and the retention of chirality when bound to a metal surface. The 3D morphology of the sample structure was confirmed by SEM. (Figure 4-10B)

In this experiment nonresonant SEROA spectra were collected from samples consisting of; (SS)- and (RR)-phe-cys bound to Au nanoparticles in an aggregated film morphology.

The vibrational spectra displayed in Figure 4-12 are: (A) SERS, (B) neat Raman spectra, (C) the average of three (SS)-phe-cys SEROA, and (D) the average of three (RR)-phe-cys SEROA. Each of the three averaged spectra per analyte, were collected at randomly chosen locations on the sample substrates. The vibrational modes of the SERS and SEROA spectra are coincident with peaks and peak manifolds observed in the Raman and / or SERS spectra. Gamma (Γ) calculations[44] returned: SERS Γ = 1 and SEROA Γ = 0.36 and 0.43 for (SS)- and (RR)-phe-cys respectively. (Figure 4-13)

The SEROA spectra exhibit symmetrical line shapes between 200 - 1540 cm^{-1}, followed by an abrupt transition to well-defined asymmetry. Excluding the strong phenyl ring modes at ~ 1000, 1200, and 1600 cm^{-1}, and the CH_2 rocking modes at 830 cm^{-1}; the SERS modes display a low S/N ratio. Nonresonant SEROA spectroscopy has resolved these vibrations. A clearly delineated example is given by the CH_2 bending mode centered at 1430 cm^{-1}. This well-pronounced Raman mode becomes a broad shoulder of the SERS peak at 1490 cm^{-1}, which is almost nonexistent in the Raman spectra. Both

peaks are resolved in the SEROA spectra. A new peak given an amide 1 assignment, appears at 1640 cm^{-1} in the SERS and SEROA spectra.[105]. As observed in the tryptophan experiments, the mirror image of the plasmonic substrate photoluminescent background contributes to the SEROA spectra.

Conclusion

In this second experiment, the complimentary amino acid sequence of phenylalanine-cysteine-glycine-glycine has been evaluated. Relative to the tryptophan SEROA spectra, the lower phe-cys Γ values and broader peak widths are attributed to the higher degree of complexity; thus a broader range of molecular-surface conformations can coexist. Observations of spectral symmetry and elucidation of a amide I mode at 1640 cm^{-1} extends the application of nonresonant SEROA from monomer to oligomer amino acid sequences.

Raman	SERS	SEROA	Assignment	ref.
1605				
1598	1590	1590	ring CC stretch	2
	1490	1490		
	1468	1468	CH_3 def	1, 3
		1458		
1430	1430	1430	CH_2 bend	1
		1378		
	1350	1350	amide III	1, 2
	1300	1300	CH_2 wag, amide III	2, 3
		1235		
1200	1205	1205	CH_2 wag	1, 2
1031	1034	1034	sym RBM	
1000	1000	1000	sym ring CC st	2
		920		
825	830	830	CH_2 rock, cys	
	800	800	CH_2 rock	1
700	700	700	C-S	1
620			COO^- + ring	1, 3
405	400	400		
270	270	270		

Table 2 Proposed Phe-Cys peak assignments. Ref 1[106], Ref 2[100] ref 3[107]

Chapter 5. Conclusion

A novel, general, and simple method, based on carbon monoxide reduction of Au and Ag plating solutions has been developed and used successfully in the synthesis of plasmonic Au nanoshells, solid Au and Ag nanoparticles. CO-NS were found to be smoother, and could be made thinner than previously possible, before incurring continuity defects. This is the first nanoshell synthesis method that can be scaled for mass production in a continuous flow process.

The first near infrared excited scattered circular polarization Raman optical activity spectrometer (NIROAS) has been designed, built, and characterized. Expectations of the conversion from a 532 nm to a 780 nm excited ROA spectrometer have been met. With consideration to the Raman (E^{-3}) and ROA (E^{-4}) scattering dependency, the NIROAS level of efficiency is comparable with 532 nm systems.

Three-dimensional nanoparticle based SEROA substrate designs applicable to biologically significant molecules have been developed, characterized, and utilized. Circular dichroism measurements of functionalized nanoparticle films confirm the retention of chirality by the amino acid tryptophan and the amine-terminated amino acid series phenylalanine-cysteine-glycine-glycine.

Nonresonant surface enhanced Raman optical activity has been validated by the repeatable collection of circular intensity difference spectra possessing extended mirror symmetry, and the elucidation of biological markers including the structurally significant W3 (*ca.* 1550 cm^{-1}) SEROA peak, in the absence of definitive SERS structure.

Bibliography

1.   Barron, L. D.; Hecht, L.; Blanch, E. W.; Bell, A. F., Solution Structure and Dynamics of Biomolecules from Raman Optical Spectroscopy. *Prog. Biophys. Mol. Biol.* **2000**, 73, 1-49.

2.   Barron, L. D.; Buckingham, A. D., Rayleigh and Raman scattering from optically active molecules. *Mol. Phys.* **1971**, 20, (6), 1111-1119.

3.   Atkins, P. W.; Barron, l. D., Rayleigh scattering of polarized photons by molecules. *MOL. PHYS.,* **1969**, 5, (16), 453-466.

4.   Barren, L. D.; Bogaard, M. P.; Buckingham, A. D., Raman Scattering of Circularly Polarized Light by Optically Active Molecules. *J. Am. Chem. Soc.* **1973**, 95, (2), 603-605.

5.   Spencer, K. M.; Freedman, T. B.; Nafie, L. A., Scattered Circular Polarization Raman Optical Activity. *Chem. Phys. Lett.* **1988**, 149, (4), 367-374.

6.   Che, D.; Nafie, L. A., Theory and Reduction of Artifacts in Incident, Scattered and Raman Optical Activity. *Appl. Spectrosc.* **1993**, 47, (5), 544-555.

7.   Hug, W., Virtual Enantiomers as the Solution of Optical Activity's Deterministic Offset Problem. *Appl. Spectrosc.* **2003**, 57, (1), 1-13.

8.   BioTools, Inc. 17546 Bee Line Hwy (SR 710) Jupiter, FL 33458, (561) 625-0133. In.

9.   Hecht, L.; Barron, L. D.; Blanch, E. W.; Bell, A. F.; Day, L. A., Raman Optical Activity Instrument for Studies of Biopolymer Structure and Dynamics. *J. Raman Spectrosc.* **1999**, 30, 815-825.

10.   Bour, P.; Baumruk, V.; Hanzlikove, J., Measurement and Calculation of the Raman Optical Activity of a–Pinene and trans-Pinane. *Czech. Chem. Comm.* **1997**, 63, 1384-1395.

11.   Jeanmaire, D. L.; Duyne, R. P. V., Surface Raman Spectroelectrochemistry part 1. Hetrocyclic aromatic and aliphatic amines adsorbed on the anodized silver electrode. *J. Electroanal. Chem.* **1977**, 84, 1-20.

12.   Abdali, S., Observation of SERS effect in Raman optical activity, a new tool for chiral vibrational spectroscopy. *J. Raman Spectrosc.* **2006**, 37, 1341-1345.

13.   Johannessen, C.; White, P. C.; Abdali, S., Resonance Raman Optical Activity and Surface Enhanced Resonance Raman Optical Activity Analysis of Cytochrome C. *J. Phys. Chem. A* **2007**, 111, (32), 7771-7776.

14.   Abdali, S.; Blanch, E. W., Surface enhanced Raman optical activity (SEROA). *Chem. Soc. Rev.* **2008**, 37, (980-992), 980.

15.   Nafie, L., Professor. In 1) validation of SEROA requires both R & S enantiomers 2) ed.; Brinson, B., Ed. Syracuse U., 2006.

16.   Nafie, L. A.; Brinson, B. E.; Cao, X.; Rice, D.; Rahim, O.; Durkor, R. K.; Halas, N., Near-Infrared Excited Raman Optical Activity. *Appl. Spectrosc.* **2007**, 61, (10), 1103-1106.

17.   Raman, C. V., A new type of Secondary Radiation. *Nature* **1928**.

18.   Raman, C. V., A new radiation. *Indian J. Phys.* **1928**.

19.   Demtroder, W., *Laser Spectroscopy, Basic Concepts and Instrumentation*. 3rd ed.; Springer: Heidelberg Germany, 2003; p 987.

20.   Barron, L. D.; Hecht, L.; McColl, I. H.; Blanch, E. W., Raman Optical Activity comes of Age. *Mol. Phys.* **2004**, 20, (8), 731-744.

21.   Blanch, E. W.; Hecht, L.; Day, L. A.; Pederson, D. M.; Barron, L. D., Tryptophan Absolute Stereochemistry in Viral Coat Proteins from Raman Optical Activity. *J. Am. Chem. Soc.* **2001**, 123, (20), 4863-4864.

22.   Hecht, L.; Barron, L. D.; Gargaro, A. R.; Wen, Z. Q., Raman Optical Activity Instrument for Biochemical Studies. *J. Raman Spectrosc.* **1992**, 23, 401-411.

23.   Jackson, J. B.; Halas, N. J., Silver Nanoshells: Variations in Morphologies and Optical Properties *J. Phys. Chem. B* **2001**, 105, (14), 2743-2746.

24.   Oldenburg, S. J., Averitt, R. D., Westcott, S. L. and Halas, N. J. , Nanoengineering of optical resonances. *Chem. Phys. Lett.* **1998**, 288, 243-247.

25.   Oldenburg, S. J.; Westcott, S. L.; Averitt, R. D.; Halas, N. J., Surface enhanced Raman scattering in the near infrared using metal nanoshell substrates. *J. Chem. Phys.* **1999**, 111, (10), 4729-4736.

26.   Kundu, J.; Le, F.; Nordlander, P.; Halas, N. J., Surface enhanced infrared absorption (SEIRA) spectroscopy on nanoshell aggregate substrates. *Chem. Phys. Lett.* **2008**, 452, (1-3), 115-119.

27.   Oldenburg, S. J.; Hale, G. D.; Jackson, J. B.; Halas, N. J., Light Scattering from Dipole and Quadrupole Nanoshell Antennas. *Appl. Phys. Lett.* **1999**, 75, (8), 1063-1065.

28.   Jackson, J. B. Surface Enhanced Raman Scattering with Metal Nanoshells. Rice University, Houston, TX, 2004.

29.   Mie, G., *Annalen der Physik* **1908**, 25, 377-445

30.   Hale, G. D.; Jackson, J. B.; Shmakova, O. E.; Lee, T. R.; Halas, N. J., Enhancing the active lifetime of luminescent semiconducting polymers via doping with metal nanoshells. *Appl. Phys. Lett.* **2001**, 78, (11), 1502-1504.

31.   Sershen, S. R.; Westcott, S. L.; Halas, N. J.; West, J. L., Temperature-sensitive polymer–nanoshell composites for photothermally modulated drug delivery. *J. Biomed. Mater. Res.* **2000**, 51, 293-298.

32.   Sershen, S. R.; Westcott, S. L.; West, J. L.; Halas, N. J., An opto-mechanical nanoshell-polymer composite. *Appl. Phys. B* **2001**, 73, 379-381.

33.   Sershen, S. R.; Westcott, S. L.; Halas, N. J.; West, J. L., Independent optical addressable nanoparticle-polymer optomechanical composites. *Appl. Phys. Lett.* **2002**, 80, (24), 4609-4611.

34.   Hirsch, L. R.; Jackson, J. B.; Lee, A.; Halas, N. J.; West, J. L., A Whole Blood Immunoassay Using Gold Nanoshells. *Anal. Chem.* **2003**, 75, 2377-2381.

35.   Hirsch, L. R.; Stafford, R. J.; Bankson, J. A.; Sershen, S. R.; Rivera, B.; Price, R. E.; Hazle, J. D.; Halas, N. J.; West, J. L., Nanoshell-mediated near-infrared thermal therapy of tumors under magnetic resonance guidance. *Proc. Nat. Acad. Sci. U.S.A.* **2002**, 23, 13549-13554.

36.   Sarkar, D.; Halas, N. J., General vector basis function solutions of Maxwell's equations. *Phys. Rev. E* **1997**, 56, (1), 1102-1112.

37.   Wang, H.; Levin, C. S.; Halas, N. J., Nanosphere Arrays with Controlled Sub-10-nm Gaps as Surface-Enhanced Raman Spectroscopy Substrates. *J. Am. Chem. Soc.* **2005**, 127, (43), 14992-14993.

38.   Wang, H.; Kundu, J.; Halas, N. J., Plasmonic Nanoshell Arrays Combine Surface-Enhanced Vibrational Spectroscopies on a Single substrate. *Angew. Chem. Int. Ed.* **2007**, 46, 9040-9044.

39.   Kerker, M.; Wang, D.-S.; Chew, H., Surface enhanced Raman scattering (SERS) by molecules adsorbed at spherical particles: errata. *Appl. Opt.* **1980**, 19, (24), 4159-4174.

40.   Moskovits, M., Surface-enhanced spectroscopy. *Rev. Mod. Phys.* **1985**, 57, (3, part 1), 783-826.

41.   Kneipp, K.; Wang, Y.; Kneipp, H.; Itzkan, I.; Dasari, R. R.; Feld, M. S., Population Pumping of Excited Vibrational States by Spontaneous Surface-Enhanced Raman Scattering. *Phys. Rev. Lett.* **1996**, 76, (14), 2444-2447.

42.   Kneipp, K.; Wang, Y.; Kneipp, H.; Perelman, L. T.; Irving Itzkan; Dasari, R. R.; Feld, M. S., Single Molecule Detection Using Surface-Enhanced Raman Scattering (SERS). *Phys. Rev. Lett.* **1997**, 78, (9), 1667-1670.

43.   Nie, S.; Emory, S. R., Probing Single Molecules and Single Nanoparticles by Surface-Enhanced Raman Scattering. *Science* **1997**, 275, (21), 1102-1106.

44.   Zhang, D.; Ben-Amotz, D., Enhanced Chemical Classification of Raman Images in the Presence of Strong Fluorescence Interference. *Appl. Spectrosc.* **2000**, 54, (9), 1379-1383.

45.   Berger, A. J.; Wang, Y.; Feld, M. S., Rapid, noninvasive concentration measurements of aqueous biological analytes by near-infrared Raman spectroscopy. *Appl. Opt.* **1996**, 35, (1), 209-212.

46.   Yonzon, C. R.; Haynes, C. L.; Zhang, X.; Jr., J. T. W.; Duyne, R. P. V., A Glucose Biosensor Based on Surface-Enhanced Raman Scattering: Improved Partition Layer, Temporal Stability, Reversibility, and Resistance to Serum Protein Interference. *Anal. Chem.* **2004**, 76, (1), 78-85.

47.   Haslett, T. L.; Tay, L.; Moskovits, M., Can surface-enhanced Raman scattering serve as a channel for strong optical pumping? *J. Chem. Phys.* **2000**, 113, (3), 1641-1646.

48.   Haynes, C. L.; Duyne, R. P. V., Plasmon-Sampled Surface-Enhanced Raman Excitation Spectroscopy. *J. Phys. Chem. B* **2003**, 107, 7426-7433.

49.   Osawa, M.; Matsuda, N.; Yoshii, K.; Uchida, I., Charge Transfer Resonance Raman Process in Surface-Enhanced Raman Scattering from p-Aminothiophenol Adsorbed on Silver: Herzberg-Teller Contribution. *J. Phys. Chem.* **1994**, 98, 12702-12707.

50.   Bishnoi, S.; Levin, C. S.; Gheith, M.; Johnson, B.; Rozell, C.; Johnso, D. H.; Halas, N. J., An all-optical nanoscale pH meter. *Nano Letters* **2006**, 6, (1687-1692), 1687.

51.   Hug, W.; Hangartner, G., A Novel High-throughput Raman Spectrometer for Polarization Difference Measurement. *J. Raman Spectrosc.* **1999**, 30, 841-852.

52.   Jenkins, F. A.; White, H. E., *Fundamentals of Optics*. 4th ed.; McGraw Hill: 1976.

53.   Guenther, R. D., *Modern Optics*. Wiley Press: 1990.

54.   Hecht, E.; Zajac, A., *Optics*. 4th ed.; Addison-Wesley Pub. Co: 1979; p 565.

55.   White, J. a., *Fundamentals of Optics*. 4th ed.; McGraw Hill.

56.   Oldenburg, S. J.; Averitt, R. D.; Westcott, S. L.; Halas, N. J., Nanoengineering of optical resonances. *Chem. Phys. Lett.* **1998,** 288, 243-247.

57.   Wang, H.; Brandl, D. W.; Le, F.; Nordlander, P.; Halas, N. J., Nanorice: A Hybrid Plasmonic Nanostructure. *Nano Lett.* **2006,** 6, (4), 827-832.

58.   Wang, H.; Brandl, D. W.; Nordlander, P.; Halas, N. J., Plasmonic Nanostructures: Artificial Molecules. *Acc. Chem. Res.* **2007,** 40, 53-62.

59.   Halas, N. J., Playing with Plasmons: Tuning the Optical Resonant Properties of Metallic Nanoshells. *MRS Bulletin* **2005,** 30, 362-367.

60.   Tam, F.; Goodrich, G. P.; Johnson, B. R.; Halas, N. J., Plasmonic Enhancement of Molecular Fluorescence. *Nano Lett.* **2007,** 7, (2), 496-501.

61.   Tam, F.; Moran, C. E.; Halas, N. J., Geometrical Parameters Controlling Sensitivity of Nanoshell Surface Plasmon Resonance to Changes in Dielectric Environment. *J. Phys. Chem. B* **2004,** 108, 17290-17294.

62.   Lal, S.; Grady, N. K.; Kundu, J.; Levin, C. S.; Lassiter, J. B.; Halas, N. J., Tailoring plasmonic substrates for surface enhanced spectroscopies. *Chem. Soc. Rev.* **2008,** 37, 898-911.

63.   Gobin, A. M.; Lee, M. H.; Halas, N. J.; James, W. D.; Drezek, R. A.; West, J. L., Near-Infrared Resonant Nanoshells for Combined Optical Imaging and Photothermal Cancer Therapy. *Nano Lett.* **2006,** 7, (7), 1929-1934.

64.   Hirsch, L. R.; Gobin, A. M.; Lowery, A. R.; Tam, F.; Drezek, R.; Halas, N. J.; West, J. L., Metal Nanoshells. *Ann. Biomed. Eng.* **2006,** 34, (1), 15-22.

65.   Prodan, E.; Nordlander, P.; Halas, N. J., Effects of Dielectric Screening on the Optical Properties of Metallic Nanoshells *Chem. Phys. Lett.* **2003,** 368, 94-101.

66.   Prodan, E.; Nordlander, P., Structural Tunability of the Plasmon Resonances in Metallic Nanoshells. *Nano Lett.* **2003,** 3, (4), 543-547.

67.   Prodan, E.; Lee, A.; Nordlander, P., The effect of a dielectric core and embedding medium on the polarizability of metallic nanoshells. *Chem. Phys. Lett.* **2002,** 360, 325-332.

68.   Prodan, E.; Radloff, C.; Halas, N. J.; Nordlander, P., A Hybridization Model for the Plasmon Response of Complex Nanostructures. *Science* **2003,** 302, 419-422.

69.   Prodan, E.; Nordlander, P., Plasmon Hybridization in Spherical Nanoparticles. *J. Chem. Phys.* **2004,** 120, (11), 5444-5454.

70.   Brandl, D. W.; Nordlander, P., Plasmon modes of Curvilinear Metallic core/shell particles *J. Chem. Phys.* **2007,** 126, 144708:1-1. H.

71.   Radloff, C. J. "Concentric Nanoshells and Plasmon Hybridization", Ph. D Thesis. Rice University, Houston, 2003.

72.   Nehl, C. L.; Grady, N. K.; Goodrich, G. P.; Tam, F.; Halas, N. J.; Hafner, J. H., Scattering Spectra of Single Gold Nanoshells. *Nano Lett.* **2004,** 4, (12), 2355-2359.

73.   Wang, H.; Goodrich, P. G.; Tam, F.; Oubre, C.; Norldander, P.; Halas, N. J., Controlled Texturing Modifies the Surface Topography and Plasmonic Properties of Au Nanoshells. *J. Phys. Chem. B* **2005**, 109, 11083-11087.

74.   Oubre, C.; Nordlander, P., Optical Properties of Metallodielectric Nanostructures Calculated Using the Finite Difference Time Domain Method. *J. Phys. Chem. B* **2004**, 108, 17740-17747.

75.   Wang, H.; Wu, Y.; Lassiter, B.; Nehl, C. L.; Hafner, J. H.; Nordlander, P.; Halas, N. J., Symmetry breaking in individual Plasmonic Nanoparticles. *PNAS* **2006**, 103, (29), 10856-10860.

76.   Wu, Y.; Nordlander, P., Plasmon hybridization in nanoshells with a nonconcentric core. *J. Chem. Phys.* **2006**, 125, 124708.

77.   Jackson, J. B.; Halas, N. J., Silver Nanoshells: Variations in morphologies and optical properties. *J. Phys. Chem. B* **2001**, 105, (1), 2743-2746

78.   Turkevich, J.; Stevenson, P. C.; Hillier, J., A Study of the Nucleation and Growth Processes in the Synthesis of Colloidal Gold. *Discuss. Faraday Soc.* **1951**, 11, 55-75.

79.   Donau, J., Uber eine rote, mittels Kohlenoxyd erhaltene kolloidal goldlosung (Red Colloid Solution of Gold Obtained by means of Carbon Monoxide). *Monatsh. Chemie* **1905**, 26, 525-530.

80.   Duff, D. G.; Baiker, A.; Edwards, P. P., A New Hydrosol of Gold Clusters. 1. Formation and Particle Size Variation. *Langmuir* **1993**, 9, 2301-2309.

81.   Perenboom, J. A. A. J.; Wyder, P.; Meier, F., Electronic properties of small metallic particles. *Phys. Rep* **1981**, 78, 173-292.

82.   Ozaki, M.; Kratohvil, S.; Matijević, E., Formation of Monodispersed Spindle-Type Hematite Particles. *J. Colloid Interface Sci.* **1984**, 102, 146-151.

83.   Johnson, P. B.; Christy, R. W., Optical Constants of the Noble Metals. *Phys. Rev. E* **1972**, 6, 4370-4379.

84.   Kreibig, U.; Vollmer, M., *Optical Properties of Metal Clusters*. Springer Verlag: Berlin, 1995.

85.   Averitt, R. D.; Sarkar, D.; Halas, N. J., Plasmon Resonance Shifts of Au-Coated Au_2S Nanoshells: Insight into Multicomponent Nanoparticle Growth. *Phys. Rev. Lett.* **1997**, 78, (22), 4217-4220.

86.   Streitwieser, A.; Heathcock, C. H., Introduction to Organic Chemistry. In *A Series of Books in Organic Chemistry*, Andrew Streitwieser, J., Ed. Macmillian Publishing Co., Inc.: New York, 1976; pp 105-126.

87.   Barron, L., Private Communication Aug. 2004. In Brinson, B., Ed. 2004; p "We have recently taken delivery of the first production model. It is around five times faster than our homemade instruments and much easier to use".

88.   Cahn, R. S.; Ingold, C. K.; Prelog, V., Specification of Molecular Chirality. *Angew. Chem. Int. Ed.* **1966**, 5, (4), 385-415.

89.   Prelog, V., Basic Principles of the CIP-System and Proposals for a Revision. *Angew. Chem. Int. Ed.* 21, (8), 567-583.

90.   Einterz, C. M.; Lewis, J. W.; Milder, S. J.; Kliger, D. S., Birefringence Effects in Transient Circular Dichroism Measurements with Applications to the Photolysis of Carbonmonoxyhemoglobin and Carbonmonoxymyoglobln. *J. Phys. Chem.* **1895,** 89, 3845-3853.

91.   Barron, L. D.; Excribano, J. R., Stokes-antiStokes Asymmetry in natural Raman Activity. *Chem. Phys.* **1985,** 98, (3), 437-446.

92.   Savitzky, A.; Golay, M. J. E., Smoothing and Differentiation of Data by Simplified Least Squares Procedures. *Anal. Chem.* **1964,** 36, (8), 1627-1639.

93.   Radwanski, E. R.; Last, R. L., Tryptophan biosynthesis and metabolism: biochemical and molecular genetics. *Plant Cell* **1995,** 7, (7), 921-934.

94.   Blanch, E. W.; Bell, A. F.; Hecht, L.; Day, L. A.; Barron, L. D., Raman Optical Activity of Filamentous Bacteriophages: Hydration of a-Helices. *J. Mol. Bio.* **1999,** 290, (1), 1-7.

95.   Delgado, J. M.; Orts, J. M.; Pe´rez, J. M.; Ro, A., Sputtered thin-film gold electrodes for in situ ATR-SEIRAS and SERS studies. *Journal of Electroanalytical Chemistry 617 (2008) 130–140* **2008,** (617), 130-140.

96.   Abdali, S., Observation of SERS effect in Raman optical activity, a new tool for chiral vibrational spectroscopy
J. Raman Spectrosc. **2007,** 37, 1341-1345.

97.   Jacob, C. R.; Luber, S.; Reiher, M., Calculated Raman Optical Activity Signatures of Tryptophan Side Chains. *ChemPhysChem* **2008,** 9, 2177-2180.

98.   Tsuboi, M.; Uedab, T.; Ushizawab, K.; Yoshiko Ezakib; Overman, S. A.; George J. Thomas, J., Raman tensors for the tryptophan side chain in proteins determined by polarized Raman microspectroscopy of oriented N-acetyl+tryptophan crystals'. *Journal of Molecular Structure* **1996,** 379, 43-50.

99.   Takashi Miura, H. T., & Issei Harada, J. Raman Spectro., 20, 667-671 (1989), Tryptophan Raman Bands Sensitive to Hydrogen Bonding & Side-chain Conformation. *J. Raman Spectro.* **1989,** 20, 667-671.

100.   Stewart, S.; Fredericks, P. M., Surface-enhanced Raman spectroscopy of peptides and proteins adsorbed on an electrochemically prepared silver surface. *Spectrochimica Acta part A* **1999,** 55, 1615-1640.

101.   Tsuboi, M.; Overman, S. A.; Nakamura, K.; Arantxa Rodriguez-Casado; Jr., G. J. T., Orientation and Interactions of an Essential Tryptophan (Trp-38) in the Capsid Subunit of Pf3 Filamentous Virus. *Biophysical Journal* **2003,** 34, (3), 1969-1976.

102.   Hodgson, A. S., Falsifications and Facts about Aspartame. In *Food Safety and Technology*, College of Tropical Agriculture and Human Resources: 2001.

103.   Guthrie, R.; Susi, A., A simple phenylalanine method for detecting phenylketonuria in large populations of newborn infants. *Pedatrics* **1963,** 32, (3), 338-343.

104.   Wei, F.; Zhang, D.; Halas, N. J.; Hartgerink, J. D., Aromatic Amino Acids Providing Characteristic Motifs in the Raman and SERS Spectroscopy of Peptides. *J. Phys. Chem. B* **2008,** 112, (30), 9158-9164.

105.   Lin-Vien, D.; Colthup, N. B.; Fateley, W. G.; Grasselli, J. G., *The Handbook of Infrared and Raman Charactoristic Frequencies of Organic Molecules*. Academic Press. Inc.: San Diego, CA, 1991.

106.   Neil A. Macleod; Butz, P.; Simons, J. P.; Grant, G. H.; Baker, C. M.; tranter, G. E., Structural, electroni circular dichroism and Raman optical activity in the gas phase and in solution: a computational and experimental investigation. *Phys. Chem. Chem. Phys* **2005,** 7, 1432-1440.

107.   Hug, W., Raman Circular Intensity Differential Spectroscopy. The Spectra of (-)-a-Pinene and (+)-a-Phenylethylamine. *J. Am. Chem. Soc.* **1975,** 97, (19), 5598-5590.
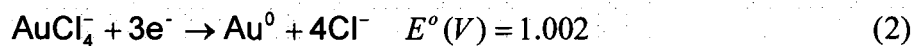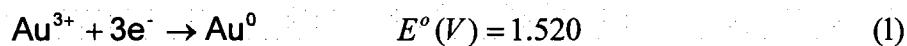
Appendix I

Supplemental Information

Thermodynamics of HAuCl$_4$ reduction in aqueous solutions using CO$_{(g)}$ and H$_2$CO$_{(aq)}$ as reducing agents

General properties: The entire process is performed at the temperature of 20 °C and pressure of 1 atmosphere. Additionally, several simplifications can be accepted. 1) The reaction environment is a dilute (1-10 mM) aqueous solution. 2) Because of their excessive amount, some reagent concentrations can be considered constant. 3) This also applies to the pH of the plating solution. The pH value remains at 5.5 during the entire process due to the carbonate buffer.

Plating solution: The plating solution is prepared as 0.38 mM of HAuCl$_4$ and 1.79 mM of K$_2$CO$_3$ in water. An aqueous solution of HAuCl$_4$ contains AuCl$_4^-$ ions as well as both free Cl$^-$ and hydrated Au^{3+} ions. However, the stability constant K_b of AuCl$_4^-$ derived from the two standard potentials (Equation 1, 2) suggests that AuCl$_4^-$ is the dominating form of Au(III) in the plating solution and that this domination increases as the reduction of Au(III) proceeds releasing free Cl$^-$ ions.

$$Au^{3+} + 3e^- \rightarrow Au^0 \qquad E^o(V) = 1.520 \qquad (1)$$

$$AuCl_4^- + 3e^- \rightarrow Au^0 + 4Cl^- \quad E^o(V) = 1.002 \qquad (2)$$

$$K_b = \frac{[Au^{3+}][Cl^-]^4}{[AuCl_4^-]} = exp\left[\frac{Fn\left(E^o_{AuCl_4^-/Au^o} - E^o_{Au^{3+}/Au^o}\right)}{RT}\right] \approx 1.9 \cdot 10^{-27} \quad (3)$$

where T is the absolute temperature 273.2 °C, R the absolute gas constant = 8.31 J / (mole*K), F = the Faraday constant 96,485 C / mol, n is the number of e^- required to balance the Redox equations.

The actual reduction of Au(III) to Au is a two-step process; Au(III) to Au(I) (Equation 4), and Au(I) to Au (Equation 5).[1] The transitional state $AuCl_2^-{}_{(aq)}$ dominates among other Au(I) species because of the reason similar to that of Au(III) described above.

$$AuCl_4^- + 2e^- \rightarrow AuCl_2^- + 2Cl^- \qquad E^o(V) = 0.926 \qquad (4)$$
$$AuCl_2^- + e^- \rightarrow Au^0 + 2Cl^- \qquad E^o(V) = 1.154 \qquad (5)$$
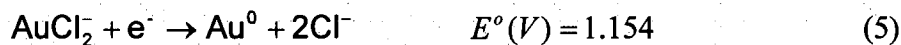
Since both processes are thermodynamically favorable, the combined Equation 6 can be considered

$$AuCl_4^- + 3e^- \rightarrow Au^0 + 4Cl^- \qquad E^o(V) = 1.002 \qquad (6)$$
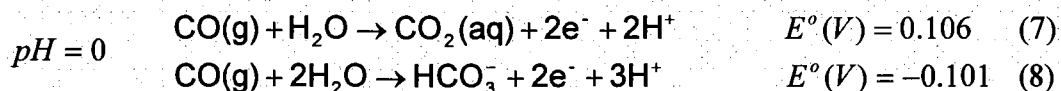
When the reducing agent is introduced into the plating solution, electrons are donated to the gold ions. The process develops towards the equilibrium between different gold species, original reducing agent and its oxidized form.

Carbon monoxide reductant: Carbon monoxide (CO) contains C(II), which transforms to C(IV), donating two electrons. There are multiple possible C(IV) products in this reaction, such as $CO_{2(g)}$, $CO_{2(aq)}$, $H_2CO_{3(aq)}$, $HCO_3^-{}_{(aq)}$, $CO_3^{2-}{}_{(aq)}$. The maximal amount of $CO_{2(g)}$ generated in the reduction process is below the $CO_{2(g)}$ solubility limit in water, which is insufficient for $CO_{2(g)}$ liberation. Between two dissolved forms, $CO_{2(aq)}$ and $H_2CO_{3(aq)}$, the $CO_{2(aq)}$ dominates with a concentration 40 times that of $H_2CO_{3(aq)}$.[2] HCO_3^- $_{(aq)}$ and $CO_3^{2-}{}_{(aq)}$ are the minor species in the *pH=5.5* reaction solutions as the *pKa₁* and *pKa₂* of $H_2CO_{3(aq)}$ are 6.37 and 10.33 respectively.

Therefore, the major reaction products in the case of *pH=5.5* are $CO_{2(aq)}$ and $HCO_3^-{}_{(aq)}$, and the concentration of $CO_{2(aq)}$ is approximately ten times larger than that of $HCO_3^-{}_{(aq)}$.

Carbon monoxide gas was introduced into the system by bubbling through the solution at atmospheric pressure through a glass diffusion tube (Chemglass) immersed to the bottom of the vial at measured flow rates (Cole Parmer) of 20 to 150 standard cubic centimeters per minute for periods of 10 to 15 seconds. The reducing half reactions are the following:[1]

$$pH = 0 \quad
\begin{array}{ll}
CO(g) + H_2O \rightarrow CO_2(aq) + 2e^- + 2H^+ & E^\circ(V) = 0.106 \quad (7) \\
CO(g) + 2H_2O \rightarrow HCO_3^- + 2e^- + 3H^+ & E^\circ(V) = -0.101 \quad (8)
\end{array}$$

Redox potentials (7) and (8) are *pH* dependent and must be adjusted for *pH=5.5* using the Nernst equation. The adjusted values are presented in equations (9) and (10):

$pH = 5.5$

$$(90\%) \quad CO(g) + H_2O \rightarrow CO_2(aq) + 2e^- + 2H^+ \qquad E(V) = 0.426 \qquad (9)$$
$$(10\%) \quad CO(g) + 2H_2O \rightarrow HCO_3^- + 2e^- + 3H^+ \qquad E(V) = 0.379 \qquad (10)$$
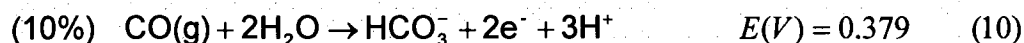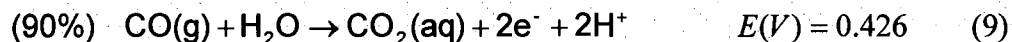
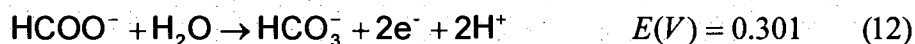***Formaldehyde reductant:*** Formaldehyde contains C(0) and acts as a reducing agent transforming to formic acid, C(II), and further to carbonates and carbon dioxide, C(IV). The formic acid $pK_a=3.77$,[1] and its dominating form at *pH=5.5* is the formate anion $HCOO^-_{(aq)}$. Possible formaldehyde reduction processes and their potentials[1] at *pH=5.5* are:

$$HCOH(aq) + H_2O \rightarrow HCOO^- + 2e^- + 2H^+ \qquad E(V) = 0.398 \qquad (11)$$
$$HCOO^- + H_2O \rightarrow HCO_3^- + 2e^- + 2H^+ \qquad E(V) = 0.301 \qquad (12)$$
$$HCOO^- \rightarrow CO_2(aq) + 2e^- + H^+ \qquad E(V) = 0.163 \qquad (13)$$

Equation (11) represents the first stage of formaldehyde reduction. Since the concentration of formic acid generated in the process is ~100 times less than that of formaldehyde and that of the carbonates in the plating solution, equations (12) and (13) can be ignored. Low formic acid concentration also favors the reaction presented in equation (11).

Oxidation-reduction process: Combining equations (6) with (9), (10), and (11), the Gibbs free energy for gold, the reduction process can be evaluated. The formal values of

the equilibrium constants of both processes turn out to be on the order of 10^{90}, which indicate that such reactions are extremely thermodynamically favorable, especially at the beginning of the process when the reagent concentration is high and no products have yet formed. Such high values effectively mean 100% reaction completion, considering that the total number of reacting molecules is $\sim 10^{16}$. Since both processes are strongly favored by thermodynamics, the kinetic factors become the most important. From this point of view, the reagent delivery to the reaction zone has to be considered.

The difference between the two reductant methods is the reducing agent delivery. An excessive concentration of formaldehyde is introduced to the system as a solution. As the reaction proceeds, the concentration in the reaction zone decreases slightly, while at the same time an oxidized form (formic acid) begins to form and increases in concentration. Both of these factors cause the actual potential of the reaction (Equation 11) to decrease from very high values during the time of the process, especially at the very beginning, which is the most important part of nanoshell growth.

In contrast, there is no such variation in potential when carbon monoxide is utilized (Equation 9, 10). First, it is supplied as a gas at a constant pressure, and therefore has a constant chemical potential. Second, the reacting solution contains an excess of C(IV) as carbonate ions, which is an oxidized form of $CO_{(g)}$, and the additional amount of C(IV) generated in the reaction is small in comparison. These two factors may be important in stabilizing the C(IV)/C(II) reduction potential and improving the quality of nanoshells fabricated with this reductant.

1. Bard, A. J.; Parsons, R.; Jordan, J., *Standard Potentials in Aqueous Solution;* Mercel

Dekker,

Inc.: Madison, NY, 1985.

2. International Chemical Safety Card ICSC: 0012, 2006.

Appendix II

1   ROA v3.20 Operation, Display and Control

Bruce Brinson

Rice University

Department of Electrical and Computer Engineering

6100 Main Street

Houston, TX 77005

Phone: (713) 348-4020

Fax: (713) 348-5686

Dave Rice

Critical Link, LLC

6712 Brooklawn Parkway

Syracuse, NY 13211

Phone: (315) 425-4045

Fax: (315) 425-4048

BioTools, Inc

17546 Bee Line Hwy (SR 710)

Jupiter, FL, 33458

Phone: (561) 625-0133

Fax: (561) 625-0717

E-mail: info@btools.com

Table of Content

1.1 Introduction

The BioTools *Chiral*Raman software application, ROA v3.20, is a functionally advanced and operationally streamlined version of the BioTools *Chiral*Raman ROA user interface.

This document is a detailed guide to ROA v3.20. The application, manual, and comments are generally applicable to the BioTools *Chiral*Raman™ product line. The intent is to provide details of operation, associated procedures, and benefits of experience to manufacturing centers, field engineers and user of *Chiral*Raman™ spectrometers.

Proprietary camera configuration and diagnostic programs are maintained by Critical Link, LLC and are available to the BioTools, Inc. manufacturing center and field engineers.

The reader is expected to possess an advanced understanding of: geometrical and polarization optics, the principles of Raman scattering and Raman Optical Activity scattering, the physical components, subsystems, and the assembly of the *Chiral*Raman Scattered Circular Polarization ROA spectrometer.

Information needed by the average user, to install the ROA software, and immediately begin collecting data will initially be presented. Subsequent sections vary in detail, depending on functions. In some cases, comments are included to provide a frame of reference. Topics are discussed as they appear in the graphical user interface, from left to right, with subtopics discussed in descending order. Information observed in the Engineering section is useful in cases where diagnostic procedures are required. The user should never attempt to alter any values in the Engineering section. The final section

describes the Simulation modes, which are used to demonstrate the software and test the

ROA application in the absence of the spectrometer.

1.2   Software Installation

ROA is a self-installing program typically delivered in a compressed file format as ROA.zip. Minimum hardware and software requirements include a Pentium-3 microprocessor-based personal computer and the Microsoft Windows 2000 or XP™ operating system. Compatibility with Microsoft Vista™ has not been determined.

ROA v3.20 is expected to be backward compatible. Nonetheless, it is strongly recommended that the user backup the current version of ROA and all supporting files before installing the ROA application.

1.3 Plotting Area

The plots shown in **Figure 1** are **A**) Circular Converter [CC], **B**) Raman and **C**) ROA spectra. When in the ROA mode, the Raman and ROA spectra are displayed in the application window. In Raman mode, only the Raman spectrum is displayed. Optionally, enabling **Setup | Show CC Graph** will display the four (4) [CC] spectra in either mode. While on the [CC] plot, a right mouse click will toggle the [CC] legend on / off. Within the legend window, the individual plots can be toggled on / off.
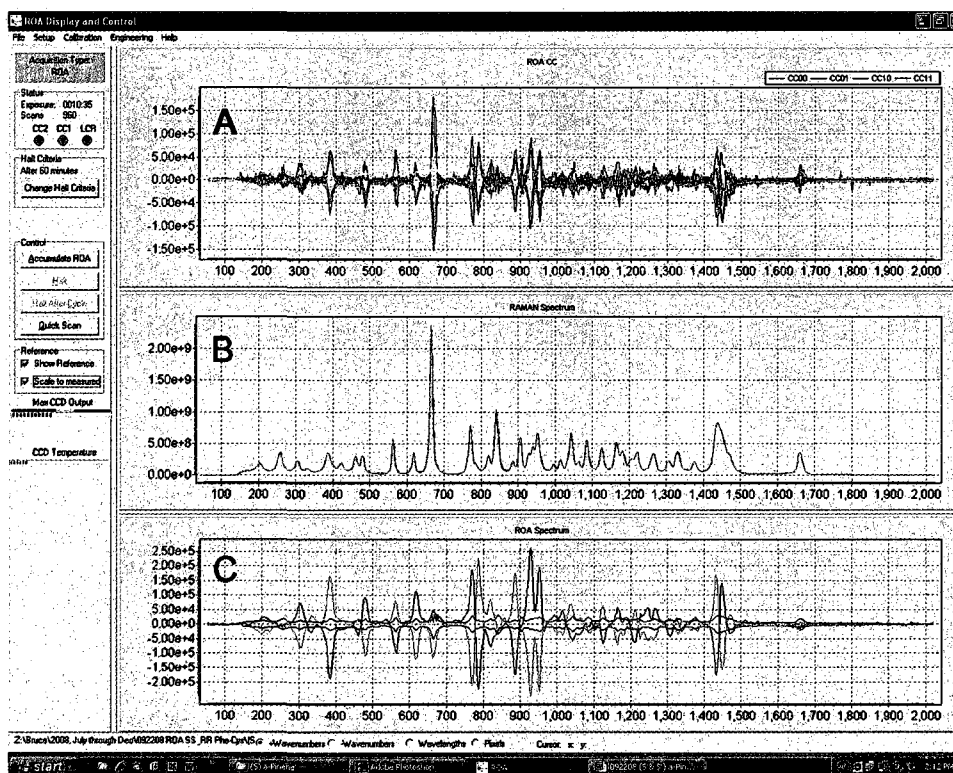

Figure 1. ROA Display and Control window with (R) and (S) α-pinene **A**) [CC], **B**) Raman and **C**) ROA spectra displayed.

While in Raman mode, the [CC] plots are meaningless. In the ROA mode, the [CC] spectra are helpful in identifying the validity of ROA peaks and the location of artifacts due to CCD pixel saturation. The DSS routine in v3.20 minimizes the saturated scan problem, but in previous versions of ROA this becomes a critical tool in the interpretation of ROA spectra. Essentially, any signal coincident with a saturation event should be very critically scrutinized.

To the trained user the [CC] spectra can be informative about the validity of the ROA and instrument conditions. These interpretations could be considered an art form, developed as the user gains experience. The [CC] plots are useful to the field engineer as a diagnostic tool for alignment and calibration.

The x-axis and y-axis by default auto-scale to present the full spectrum. By clicking and dragging the mouse from upper-left to lower right, the user can select an area of the plot to zoom in on.

To zoom back to the full spectrum, drag the mouse in the opposite direction (from lower-right to upper-left). Note: It does not matter how far the user drags the mouse in this direction; any drag in this direction will result in full spectrum display. The relative size of the two or three plots can be adjusted by grabbing the bar that separates them and sliding it up or down.

The bottom of the main screen includes four buttons that allow the user to specify the X-axis in units of increasing or decreasing wavenumber (cm^{-1}), wavelength (nm) or CCD column number.

In the lower right corner of the screen, the X and Y values as a function of the computer mouse position on a plot are displayed in real time.

1.4   Instrument Operation

This section describes the basic operation of the ROA instrument. The camera power supply should be turned on prior to running the ROA application. The spectrometer can be turned on before, or after the application is run. However, if the ROAS is turned off, clicking an acquire button will generate errors. The program will have to be terminated within Windows Task Manager ™.

Raman Intensity Adjustment

Once the sample is prepared and placed in the sample holder, the first step in measuring an ROA spectrum is to adjust the intensity of the Raman spectrum. This initial step is very important. It ensures that the CCD is not saturating thus operating in the linear response regime while minimizing data collection time and the signal to noise ratio. While in Raman mode, adjust the sample position for maximum intensity. Note: In SERS applications, the position of maximum intensity may not be the optimal position. If, for some reason, the system is in **Easy Calibration** mode (usually for alignment procedures), the laser safety interlock is overridden, so extreme care must be taken. A red warning message is placed at the bottom of the main screen to remind the user that the system is in this mode.

Be sure to wear laser eye protection goggles suited for operation at your laser wavelength, typically 532 or 780 nm. Jewelry, including wristwatches, should be removed when working in the sample compartment with the safety lock disabled. Additionally, when working with the ROAS enclosure removed, specular surfaces such

as belt buckles should be removed. Any chair(s) in which a person sitting would be at, or close to, eye level with the spectrometer, should be removed from the room. Alignment procedures can be performed with the laser at low power, i.e., a few mW. If the laser intensity is high, the user must also take care not to put his hands or any flammable material in the path of the beam!

Now, press **Quick Scan** to assess the Raman intensity. Roughly adjust the laser intensity to get the **Max CCD Output** meter in the green range and within 2 blocks of the yellow range. If necessary, stop the Quick Scan and adjust the Illumination Period on the **Acquisition Setup Screen**.

Sample Placement Optimization

Once the Raman intensity is within the green range, use the horizontal adjustment wheel on the sample holder to move the sample closer to or farther from the objective lens. While making this adjustment, watch the Raman intensity. Adjust this position for maximum Raman intensity. Once this is complete, adjust the laser power or illumination time to get the **Max CCD Output** meter into the high end of the green range. Halt the acquisition and if applicable turn off the **Easy Calibration Mode.**.

Collecting Spectra

The user is now ready to collect an ROA spectrum. Press the **Accumulate ROA** button on the main screen to begin this process. Within a few seconds, data will appear in the Raman plot. The CC2, CC1, and LCR indicators will start changing color. Furthermore, the number of **scans** and **exposure** counters should begin incrementing.

The instrument can be left to collect data. In the **Change Halt Criteria** window, the acquisition period can be set to end after 1) a number of scans, 2) a specified amount of accumulated exposure time, 3) a number of counts at a predetermined position on the x-axis or, 4) to run until stopped by the user. When satisfied with the spectrum, the user can simply press the **Halt After Cycle** or **Halt** button to stop the acquisition.

1.5   Main Screen

The ROA Display and Control window, see **Figure 1**, is the primary user interface. The interface consists of the control panel, pull down menus, and the plotting area. All user controls are accessible through this screen. A fair warning: unless advised by Biotools, Inc,. it is strongly recommended that the customer <u>not</u> attempt to make any changes within the **Engineering** menu windows.
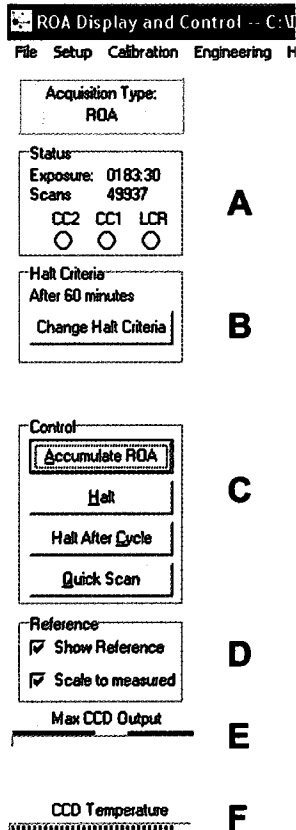
1.5.1   Control Panel

Figure 2. ROA control panel.

Acquisition Type will indicate the kind of spectra being acquired as selected in the **Setup | Acquisition Setup** window, which will be discussed later.

Status (Figure 2A) indicates the currently accumulated **Exposure** time (MMMM:SS), and the number of valid Raman **Scans** (exposures) accumulated in all [CC] states. The accumulated exposure time is the total amount of time that the CCD camera is exposed to scattered light, not real time. Real time will vary depending on exposure time and CCD read -out time.

Three indicators display the state of the circularity converters (CC1, CC2) and the liquid crystal retarder (LCR). These indicators are meant to provide the user with a visual indication that the correction cycles of the ROA instrument are operating normally.

Halt Criteria (Figure 2B) displays the user-defined conditions under which the data collection period (scan) will end. This can be specified in total exposure time or the number of exposures. The **Change Halt Criteria** button will open the **Halt Criteria** window **(Figure 3)**. Conditions under which a spectral scan will terminate are displayed in and controlled through this window.

A scan can be halted manually when the **Control | Halt** or the **Control | Halt after Cycle** button is selected, or automatically after 1) a specified number of scans, 2) specified amount of accumulated illumination time, or 3) a specified number of counts at a specified position on the x-axis (cm_{-1}). Alternatively, when satisfied with the spectrum, the user can simply press the **Halt After Cycle** button to stop the acquisition. The **Halt**

when the Halt button is pressed option does not have to be enabled to use the **Halt** or

Halt after Cycle buttons in the **Control panel**. In the case of a preset number of scans or

exposure time, the preset value will be displayed in the **Halt Criteria** panel.
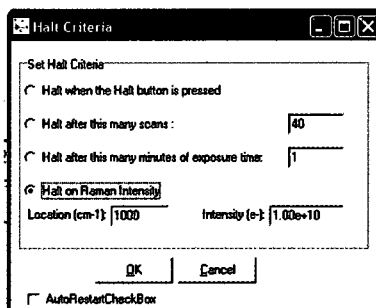
Figure 3. Halt Criteria control window.

The **Control panel** (**Figure 2C**) includes four (4) buttons for starting and

stopping the acquisition of ROA and / or Raman data.

Buttons may be actuated by clicking the left mouse button or the underlined letter

on keyboard. **Accumulate ROA** will initiate an **ROA** scan, conventional **Raman** scan or

a **Degree of Circularity** scan. When this button is pressed, the instrument begins all of

the operations required to accumulate the chosen spectra. The user is presented with a

dialog box, which asks if the user wants the data cleared before starting. (**Figure 4**)
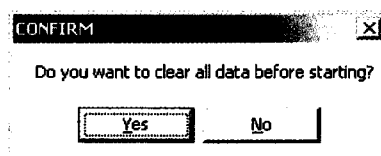
Figure 4. Clear data option / confirmation window.

112

If this is a new sample scan, answer "Yes", so that previous data will be cleared. If the user is continuing a run that has been halted, or would like to add data to a run that was previously saved (**File | load filename.dat**), answer "No", to have the system add new data to the existing data.

The **Halt** button is used to halt the acquisition <u>immediately</u>. The instrument will not complete a correction cycle, but will stop when the current exposure period ends. The **Halt** button should only be used when collecting only Raman spectra or when performing calibration and setup operations, not when collecting ROA spectra. When selected, a **Confirm** window will appear (**Figure 5**).
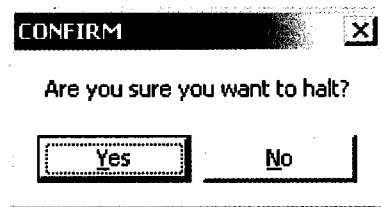
Figure 5. The Halt or Halt After Cycle button confirmation window.

The **Halt After Cycle** button is used to halt the acquisition after completing the correction cycle (a set of 32 exposures) in progress. By using this button, the user ensures that the collection of data will include equal numbers of spectra in each of the correction states. When selected a **Confirm** window will appear (see **Figure 5**).

The **Quick Scan** button is used while calibrating the instrument, setting up a scan, or to view spectral exposures individually; that is, without accumulating counts from

multiple exposures. In this mode, the system will acquire, display, and clear data until the user **Halts** the process or the **Halt Criteria** have been met. In this mode, the user can view the effects of changing the laser intensity, exposure time or sample position in near real time. The displayed exposure appears two (2) exposure periods after it is acquired.

Reference

If enabled (**File | Load Reference**), the **Reference panel** (**Figure 2D**) appears below the **Control Panel** (**Figure 2C**). The reference data displayed (orange) can be toggled on / off by checking the **Show Reference** box. When the **Scale to Measure** box is checked, the reference Raman spectra is scaled to the displayed data at the point along the x-axis, where the y-axis has the greatest intensity. The reference ROA spectrum is scaled proportionately.

Max CCD Output

The **Max CCD Output** meter (**Figure 2E**) monitors the CCD pixel of highest intensity during a single exposure, not to be confused with the intensity of a spectral peak or sum of counts along a column of pixels.

Optimally, the laser power and exposure period should be adjusted so that the indicating bar is in the green range, a block or two to the left of the yellow range. Improper adjustment can result in an increase in the number of spectra discarded by the **DSS** routine (see **Setup | Acquisition Set up | Discard Saturated Spectra**), due to pixel saturation. Alignment issues (see **Image Alignment and Binning**) can significantly affect the overall collection efficiency of the CCD array.

Recall that:

1) The output from the polarization analyzer is coupled to the spectrometer via the hexagonal close packed (HCP) fiber arrangement at the input of the fiber-optic bundles and the fibers at the output are arranged in an arc that compensates for spherical aberration induced by the spectrograph.

2) The image, on the CCD array is that of fiber-optic bundle.

3) The intensity displayed in the Raman spectra is the sum of charge in each column of pixels. In principle, it may be that one or all pixels in a column contribute to the sum.

4) The response of a saturated CCD pixel is non-linear and thus any single saturated pixel will corrupt the collective value of the binned of pixels.

When coupling the output of the polarization analyzer to the inputs of the fiber-optic bundles, the optimal position of the fiber bundle produces uniform illumination, along a column of pixels. At best, a close approximation to this condition can be achieved. In the worst-case scenario, but not possible in the ROAS design, all light is incident on one (1) pixel. Neither is there any reason to expect the illuminated pixels to be a continuous line of pixels. This is due to the geometrical conversion from the 2D (HCP) arrangement at the input of the fiber bundle to the 1D arrangement at the output, e.g. in the spectrometer's object plane. The objective when aligning the fiber bundles (x, y, z) to the polarization analyzer output is to maximize the total photon count along a column(s) of pixels.

Although compensated for by the radial slit design of the fiber bundle, due to the effects of spherical aberration, it is possible that the image of the fibers on the CCD array can be slightly defocused toward the upper and lower edges of the CCD array relative to the middle of CCD array. Therefore, preferentially, the higher intensity pixels should be positioned close to the edge of the CCD array. If the energy distribution along the column is reasonably uniform and the image of the object is slightly defocused as in **Figure 15C**, due to the design of the instrument, this becomes an insignificant point.

Recalling that the system resolution is 8 cm^{-1} and that this equates to about four (4) horizontal pixels, the sharpest focus of the FO bundle is not necessarily the best condition for maximizing the number of photons that can be counted within a given exposure period. A slight defocus that spreads the central intensity in the image of a fiber across 1.5 to 2 pixels is ideal for maximizing signal intensity. The defocus of the fiber will also reduce spectral noise, e.g. smoothe the spectra.

It is important that the CCD binning is correctly calibrated. This should be done following any alignment work or physical disturbance of the instrument. (**Calibration | Image Alignment and Binning**).

CCD Temperature

The **CCD temperature meter (Figure 1F)** indicates the relative temperature of the CCD array. The camera power supply must be turned on before running the ROA application. The camera will not begin cooling down until the ROA application is open. In practice, the ROAS and camera should be turned on at the same time. When collecting

spectra, the meter should be in the range of 3-5 blocks from the left of the screen. It will take ~15 minutes to reach the correct temperature.

In some versions of ROA prior to v3.20, the application has to be started with the camera turned on and while the camera is still on, the application must be closed and restarted.

Messages

The area above and below the **Max CCD Output** and the **CCD Temperature** meters are used to display messages. The messages are self-explanatory and vary with versions. In the case of v3.20 the common message options include 1) "Camera Cooling Off!" 2) "LCR Not Calibrated" 3) "Easy Calibration Mode" 4) "Sample cover is open", 5) "Waiting for Lock" (LR synchronization)", and 6) a DSS "Saturated Scan" counter.

1.5.2   Pull down menus

Export
Import

Load Data
Load Reference

Print ROA Graph
Print RAMAN Spectrum Graph
Print Screen
Printer Setup...

Set Data Directory...

Exit

ROA Display and Control
File   Setup   Calibration   Engineerin
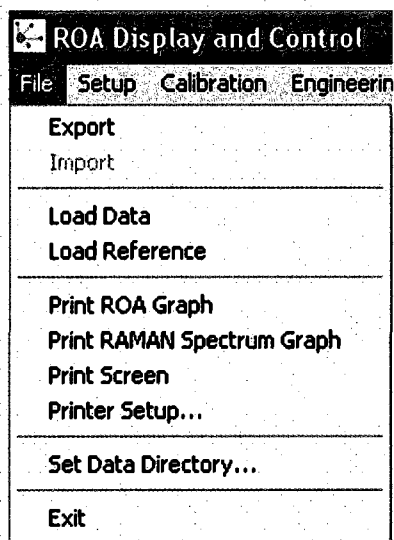
Figure 6. File pull down menu.

1.5.2.1   Files

Export will export the data display in the main screen into four (4) file formats: .dat, .plt, .txt and .all. Filenames include the Sample Name from the set up window, the date, and the time the file was saved.

Filename.plt is a ASCII file containing the x-axis, Raman and ROA data strings. This is the output file generally intended for the user to import into spreadsheet and plotting programs.

Filename.dat is a system file readable by the ROA application. This is the file loaded by the Load Data or Load Reference command.

Filename.txt is a tab and comma delimited ASCII file containing the information written in the **Setup | Acquisition Setup | Comments** window, Raman, ROA, and spectra recorded in all [CC] and LCR states.

Filename.all is an ASCII file containing the x-axis and spectra recorded in all [CC] and LCR states.

In previous versions of ROA, it was necessary to export the data at the conclusion of the scan. As of ROA V3.20 within the **Setup | Acquisition Setup** window checking the **Save at the End of Collection** box will automatically export the four (4) files at the end of the scan as defined in the **Halt Criteria**. If the scan is stopped before the **Halt Criteria** and **Save at the End of Collection** is not enabled, the data must be exported using this command.

Load Data loads a previously saved filename.dat file.

Load Reference loads the Raman and ROA spectra (orange) from a previously saved filename.dat file, for comparison to the displayed data (green).

BUG Alert: In some previous versions of the ROA when a reference spectrum was loaded, the contents of the **Setup | Comments** window and the **Sample Name** from the reference.dat file have been known to replace the entries for the current sample.

Additionally, the elapse scan time will become that of the **Reference data**. This problem has been resolved.

Work around: Load the last **filename.dat** file created before the Reference File that was previously loaded. When the file is loaded, the contents of the **Comments** window and the **Status window**'s **Exposure** and **Scans** values should be restored. The **Sample Name** will <u>not</u> be restored and must be manually reentered. To prevent confusion in the future, any files created with the **Reference Data** info in the setup box and incorrect filename should be promptly deleted. Verify that all settings have been returned to the desired state before proceeding with the next scan. Creating a text file while setting up a scan is a convenient way to compose and enter information into the **Comments** window, via the copy and paste commands.

Print Raman Graph sends the displayed Raman spectrum to the default printer.

Print ROA Graph sends the displayed ROA spectrum plot to the default printer.

Print Screen, not to be confused with the keyboard *print screen* button will send the main screen to the default printer. Alternatively, the computer's *print screen* button can be used to copy the entire image of the computer screen to the clipboard, after which it can be pasted into a document and more easily managed.

Printer Setup will display the typical Microsoft Windows™ printer setup window.

Set Data Directory opens the **Set File Locations** window (**Figure** 7) from which the subdirectory to which data will be saved can be chosen. The data directory has to be created outside of the ROA application, for example with MS Explorer™. If a subdirectory is defined while the **Set | Data | Directory** window is open, clicking the yellow file folder will refresh the directory tree. Within the **File | Set Data Directory** window the chosen data directory must be double clicked.

Bug Alert: In some previous versions of ROA, the application will create a data subdirectory with the selected subdirectory's name and save the data subdirectory(s) outside the chosen directory. Data files will be saved into a subdirectory(s) created by ROA that resides outside the selected subdirectory.

Work around:

Select the subdirectory you want data saved to. Exit ROA and reopen the application. The data files will now be stored in the data subdirectory(s) ROA created in the user selected subdirectory.

The location of manually **Exported** files will default to the data subdirectory created by ROA. However, an alternative subdirectory can be selected.

The SNR.cvs file will be saved by default into the user selected subdirectory, not in the application generated data directory.
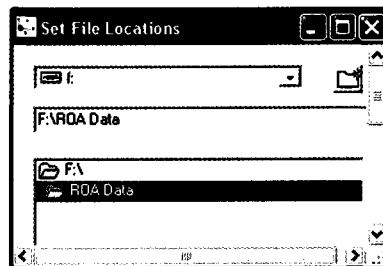
Figure 7. Set File Location Window.

1.5.2.2   Setup
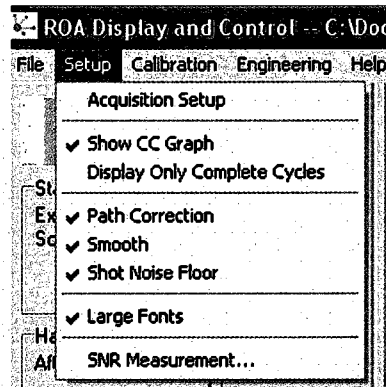
Figure 8. Setup drop down menu.

1.5.2.2.1   Setup window

Setup | Acquisition Setup

The **Acquisition Setup window**, shown in **Figure 9** is used to control the majority of the user-definable options.

Length of Illumination Period defines the duration of one (1) exposure of the CCD array to the scattered light. The time required for one (1) ROA scan includes 32 exposure periods, plus 32 CCD read periods. The CCD read period can be observed in the **Engineering | Instrument Setup (Factory Settings)** window. Because of the synchronization / timing of the linear rotators, only certain illumination times (exposure periods) are allowed. Moving the slider to the left or right, or pressing the left or right

arrows will decrease or increase the illumination time. Exposure periods range from about 73.5 ms to 10.3 seconds.

Because reading out the CCD generates read out noise, when scattered photons are limited, longer exposures are preferential to multiple, short exposures.

Shutter Run State determines which of the two shutters will be used to collect the data. The **Incident** shutter controls the light before it enters the sample cell. The **Scattered** (spectrometer) shutter controls the entry of scattered light into the spectrometer. The **Scattered** shutter must be used for calibration procedures that require a neon lamp.

Enabling the incident shutter will minimize the amount of time that the sample is exposed to light. This is important if the sample is susceptible to photochemical decomposition. Inversely, leaving the shutter open may serve to preferentially photo bleach or burn out fluorescent chronophers in the sample.

When the incident shutter is left open during a scan, the scattered shutter must be enabled. It is not normally necessary to use both shutters simultaneously. Additionally, leaving **Calibration | Quick Calibration | Easy Calibration** enabled will hold the incident shutter open. This is useful when aligning the ROAS. It is also useful when working with samples that fluoresce, since leaving the sample illuminated constantly can help to burn fluorescent chronophers, prior to the beginning of the data acquisition.

The elimination of fluorescent chronophers is often applicable when analyzing biomolecular molecules in resonant Raman and ROA experiments (533 nm). However,

for non-resonate experiments (780 nm) fluorescence by biological molecules does not present a problem.

Note: The incident shutter will not be heard by the user, although the scattered shutter should be clearly heard. If, when enabled, the spectrometer shutter is not heard, applying a small drop of oil to the shutter's solenoid should resolve the problem. Do not apply oil to the shutter blades.

In future models, the design of the spectrometer shutter mount should be changed, so that the spectrometer shutter solenoid is positioned vertically with the solenoid rod pointed downward.
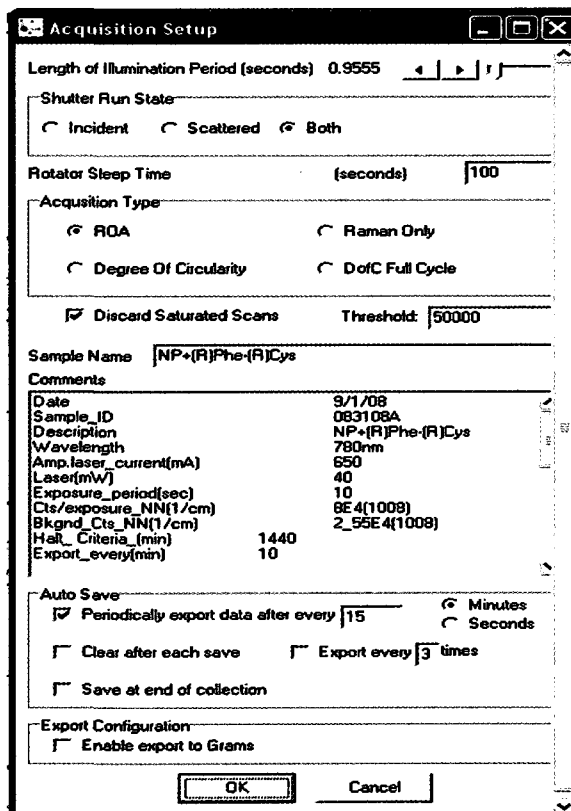
Figure 9. The Acquisition Setup window.

Rotator Sleep Time [NNN] is the amount of time that the system waits after going to an idle state before shutting down the rotator motors. Normally leaving this set in the range of 100 – 200 seconds will help to avoid delays on startup while the system waits for the linear rotator motors to synchronize.

Acquisition Type allows the user to select from four (4) options; 1) **ROA** measurements, where full artifact correction is employed, 2) **Raman** 3) Regular **DoC** puts the ¼ wave plate in the beam but does not put the CC's in the beam path(s). This allows the observation of the effect of nearly purely circularly polarized light as the source.4) **DoC Full Cycle** puts the ¼ wave plate in the beam and does the regular [CC] dance. This allows one to get a feel for how well the system is canceling incident, circular polarized light. The typical user will not use the **DoC** modes.

Discard Saturated Scans A saturated pixel is defined as a pixel on which the incident intensity is sufficient to shift the detector response from linear into the non-linear (exponential) regime. Saturated pixels are commonly attributed to a cosmic ray(s) incident on the CCD array. Within ROA spectra, cosmic rays can result in well-defined positive, negative, and sigmoidal peaks. These are purely spectral artifact(s).

DSS will discard the eight (8) spectra in the associated [CC] state in which the y-value of a one (1) single point along the x-axis exceeds the average value of the two (2) adjacent columns by a preset threshold value. The system will then recollect eight (8) spectra in that [CC] state. Additionally, a message including a counter will be displayed below the **CCD Temperature** meter.

125

The stronger the ROA signal, the less of a problem saturated scans present. **DSS** errors appear to have three (3) origins. 1) cosmic rays, 2) excessive intensity at the CCD array which most likely due to improper setup parameters and 3) leaving either of the **Simulations** modes enabled.

The cosmic ray problem is cumulative in the ROA spectra, thus longer scans are at greater risk. If two (2) adjacent columns contain saturated pixels, the routine will not discard the spectral. Due to the high number of counts in the Raman spectra, pixel saturation events will not be observed in the accumulated Raman spectra, but can easily be observed in the [CC] spectra. The threshold for discarding spectra can be set in the window to the right of the **DSS** check box. Possible values for the threshold range from 0-65,536, with 64,000 being the default value (no filtering).

If **DSS** is enabled and the scattering intensity is excessive, no data will be displayed because it is all being discarded. This could be confusing when setting up the next sample if it turns out to be much brighter than the previous sample.

When the **CCD Max** meter is at the green to yellow transition region, the nominal A to D value is ~25,000. The adjustable threshold range is then between the intensity and 65,500K. The discarding of spectra will increase the overall collection period, so this parameter should be optimized. A threshold value of 28,000 seems to be a reasonable value for catching saturated scans where the intensity of the column exceeds $1E^5$.

Sample Name is a text through which the user can enter an identifier that will be included in the name of all saved files.

Bug Alert: Older versions of the ROA application are not protected from user entry of illegal characters (* \ / > < | : ?). If an illegal character were entered, no files will be saved. This problem has been resolved. Additionally, ROA will allow filenames that exceed 64 characters. This may result in files that Windows™ applications will not open. This problem has not been resolved.

Comments is a text box in which the user can save information about the sample, along with the data that is collected. Information in the **Comments** box will be found in the .dat files, .all and .txt file, which are created by the **File | Export** command and when the **Setup |Acquisition Setup | Save at end of collection** option is enabled.

Periodically export data after every [ ] This feature will export a filename.dat file periodically over the duration of the scan. In the event of a power failure, sample photochemical decomposition, or an instrument problem; the data up to that point has been saved. After trouble shooting a problem, the last acceptable data file (.dat) can be reloaded and the scan resumed. The amount of time between saves is specified in the box to the right. These are real time minutes, not minutes of exposure time. The time between exports must exceed the amount of time required to collect 32 scans unless only Raman spectra are being collected. In this case, time must be allowed for 8 exposures. Unlike the **File | Export and Setup | Acquisition Setup | Save at end of collection** routines, only a filename.dat file will be saved. This feature is normally enabled.

Clear after Each Save clears the previous scan after the **Periodically export data** routine saves a filename.dat file. This can be used for time resolved experiments. This feature is only applicable to Raman spectra. ROA data becomes meaningless if this feature is enabled.

Exports every [ ] times exports a filename.dat every [N] scans. This feature can be used for time-resolved experiments, but otherwise is typically disabled.

Save at end of collection will run the **File | Export** command when the scan is stopped by the **Halt Criteria** or **Halt after Cycle** command.

Enable export to Grams when enabled, data is exported in a Grams data format. Use of this feature requires a Software License available from BioTools, Inc. If this feature is enabled, the application will not automatically save filename.dat files, nor will the **File | Export** functions work.
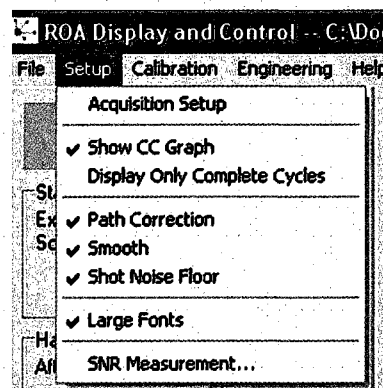

Figure 10. Setup drop down menu.

Setup | Show CC Graph

When enabled adds a plot of the | Il - Ir | spectra for each of the 4 [CC] logic states to the application window (**Figure 1A**).

Setup | Display Only Complete Cycle

When enabled, the Raman, [CC], and ROA spectra are only updated after a complete set of scans have been collected in each of the [CC] logic states. This feature is typically enabled.

Setup | Path Correction

Due to the nature of transmission through the two paths separated by the beam splitting cubes, some systematic errors can be introduced into the measurements. In previous versions of ROA, the algorithm attempts to quantify the difference and apply a correction to the collected data.

The **Path Correction** code has been rewritten to include compensation for intensity differences between [CC] states, induced by translating waveplates. This modification is also beneficial under conditions where slow variations of laser, and / or scattering intensity are encountered. The new path correction (really, intensity correction would be more accurate) is calculated at the end of each set of 32 scans.

Setup | Smooth

The ROA software allows the user to apply a 5-point boxcar-smoothing algorithm to the data. This algorithm makes each plotted point equal to the average of the original point and its four closest neighbors.

The basic resolution of the ROA instrument, ~ 8 cm^{-1}, is determined primarily by the image size of the slit on the CCD camera. In this system, the slit image is four (4) to five (5) pixels wide. For this reason, 5-point smoothing will have little effect on the system resolution, while significantly reducing the shot noise. The feature is typically enabled.

Setup | Photon Shot Noise Floor

The quality of the spectra collected on the ROA instrument is primarily limited by the photon shot noise. This is overcome by collecting large numbers of counts, often over long periods of time, which reduces the shot noise floor, relative to the signal. The ROA software will compute and plot an estimate of the shot noise floor, based on the Raman spectrum and display it with positive and negative signs in the ROA plot. It is not exported but can easily be calculated, e.g. = ± SQRT(Raman counts) .This feature is typically enabled

Setup | Large Fonts

Toggles the plot axis font size.

1.5.2.2.2   Setup | SNR Measurement

The SNR window facilitates the plotting of the intensity ratio for 6 (six) pairs of points along the X-axis, in real time. If **Sig only** and **Enable** are selected, the Raman intensity will be plotted at the position indicated in the **Signal** window. The value in the **Reference** window is ignored.
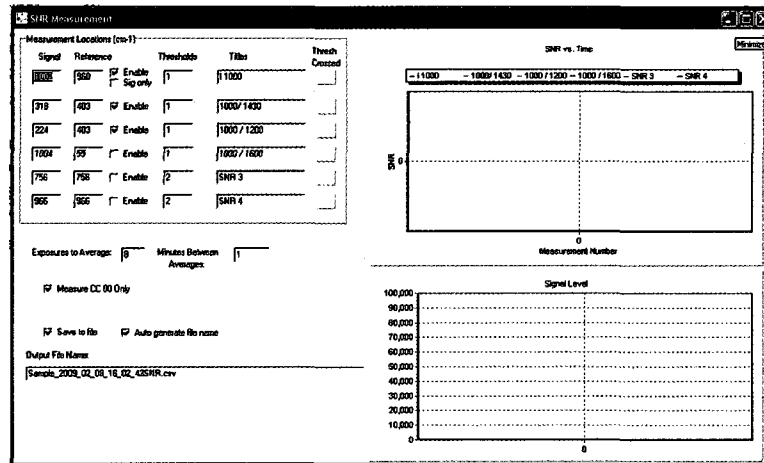
Figure 11. SNR Measurement, Peak intensity and ratio plotting window.

Each of the six (6) data strings can be enabled or disabled and each can be titled. A **Threshold** value for changes in the ratio of Y-axis values can be set. If the ratio falls below the set value, the appropriate **Threshold Crossed** box will turn red. To reset the boxes, the scan must be stopped and restarted. Note: The intensity includes background noise. To disable the **Threshold Crossed** alerts, set the threshold to zero (0).

Scans (exposures) **To Average** should be set to 32 when collecting ROA spectra. If other values are used, due to reflective losses when waveplates are inserted, the SNR trace will be transformed from a line to a periodically oscillating trace, offset by the

average SNR. In the case of a purely Raman scan any number of exposures can be averaged. The SNR plots will be updated when .dat files are saved.

Minutes Between Averages is the real time between the end of the last set of average exposures and the beginning of the next set of exposures to be averaged. To average continuous sets of N scans, set time = 0.

Measure CC 00 Only When enabled, only scans in the [CC] = [00] state will be included in the SNR average. Enabling this option is recommended if any number of scans other than 32 is to be averaged during an ROA scan.

In the case of ROA, optimally the number of **Scans To Average** should be **32** or **8** with **Measure CC 00 Only** enabled. If the **Minutes Between Averages** is set to a time less than the time required to collect N + 24 spectra (or the number of **Scans To Average**), the SPR plot will average every other set of N scans.

When **Save to file** is enabled, the data strings will be saved to an SNR.cvs file. This file is updated each time a data point is added.

Auto generate file name, when enabled, will add the **Sample Name** defined in the **Setup** window to the SNR filename and written to the subdirectory specified under **File | Set Data Directory**.

If the SNR window is closed and reopened during a scan, the previously collected SNR data points will not be displayed. However, the SNR.cvs file will continue to be updated. There will be a break in the data string if the scan is stopped and restarted. This will have to be manually edited, if the user would like one plot that includes all of the data points.

1.5.2.3 Calibration

| File | Setup | Calibration | Engineering | Help |

| Acquisiti |
| R(|

Wavenumber / Wavelength Calibaration
LCR Calibration
Image Alignment and Binning

Status
Exposure

Easy Calibration Mode
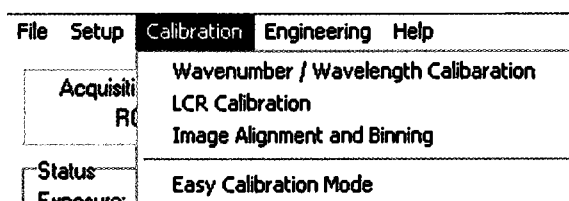
Figure 12. The Calibration pull down menu.

1.5.2.3.1 Wavenumber / Wavelength Calibration

Calibration of the system for accurate measurement of wavenumber or wavelength requires a neon lamp. Before executing the calibration routine, the application will compare the neon lamp spectrum to the spectrum embedded in the application. In the event that the spectra are not a close match, the software will not be recalibrated.

Wavelength/Wavenumber Calibration

Laser Wavelength: 779.75

Calibrate | Cancel

Figure 13. The Wavelength / Wavenumber Calibration window.

1) Turn off the laser. Position the calibration lamp on the sample compartment rail, far from the objective lens and insert the calibration lamp. The position of the neon lamp will be adjusted later. The Ne lamp emits UV in addition to visible and NIR radiation. **Avoid looking directly at the lamp.**

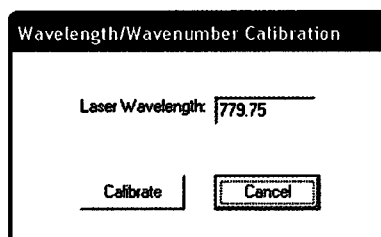2) Enable the **Easy Calibration Mode** in the calibration menu. When enabled, the incident shutter will remain open continuously. The sample door interlock will likely have to be bypassed using the supplied tool. The spectrometer shutter must be enabled in **Setup | Acquisition Setup** window.

3) Press the **Quick Scan** button on the main screen. The lamp position can be adjusted so that the **Max CCD Output** meter is in the green, and within a couple blocks of the yellow range. Note: If the photon intensity on the CCD array is excessive and the **DSS** routine is enabled, the **Max CCD Output** meter may not respond because the **DSS** routine is discarding all scans.

4) Adjust the illumination time on the **Setup | Acquisition Setup** window. Note: To change the illumination time, the user must halt the acquisition, change the value, then re-enable **Quick Scan.**. Repeat this until there is a high green indication on the **Max CCD Output** meter

5) **Halt** the **Quick Scan** acquisition and press **Accumulate ROA** to start accumulating spectra. After the Ne lamp spectrum has been collected, press **Halt**.

6) Select **Calibration | Wavenumber / Wavelength Calibration** and enter the laser wavelength. Most *Chiral*Raman systems use a solid state frequency doubled ND:YAG laser emitting at 532nm, with a 20-30 GHz free spectral range. In this type of laser, the line position and width are well defined by atomic transitions and do not change. Enter 532 in the **Laser Wavelength** box and click **Calibrate**. The application will compare the spectra to an

embedded Ne spectrum. If they are reasonable approximations of each other, the x-axis will be calibrated.

At the time of this writing, the highest optical power NIR lasers (1-1.5 W) on the laser market are wavelength tunable diode lasers in a Littrow configuration. Differences of 0.1nm will shift the spectrum a few wave numbers, and very few laser labs have the capability to resolve laser wavelength with 0.1 nm resolution. Laser wavelength meters available from Bristol Instruments are capable of measuring wavelengths to .002 nm of resolution and are a potential means of using a tunable laser (Bristol Instruments' laser instruments are developed jointly with Critical Link).

One way to address ambiguity in the laser line wavelength is to use a known Raman line (calibration molecule) and tweak the laser or wavelength entered in the calibration window.

To this end, collect and export the Ne lamp spectra. Collect the Raman spectra of a reference molecule and compare the peak to the position indicated on the x-axis. If the peak position is incorrect, load the Ne spectra, tweak the **Laser Wavelength** value, and click **Calibrate**. Repeat this process iteratively until the peak position is in the correct place. The final wavelength value may be in the 100^{ths} of a nm.

The x-axis is now calibrated for wavelength and wavenumber.

1.5.2.3.2   LCR Calibration

The **LCR Calibration** screen is used to determine optimal control voltages for operating the liquid crystal retarder (LCR) as a dynamic $\pm \lambda/4$ wave plate.
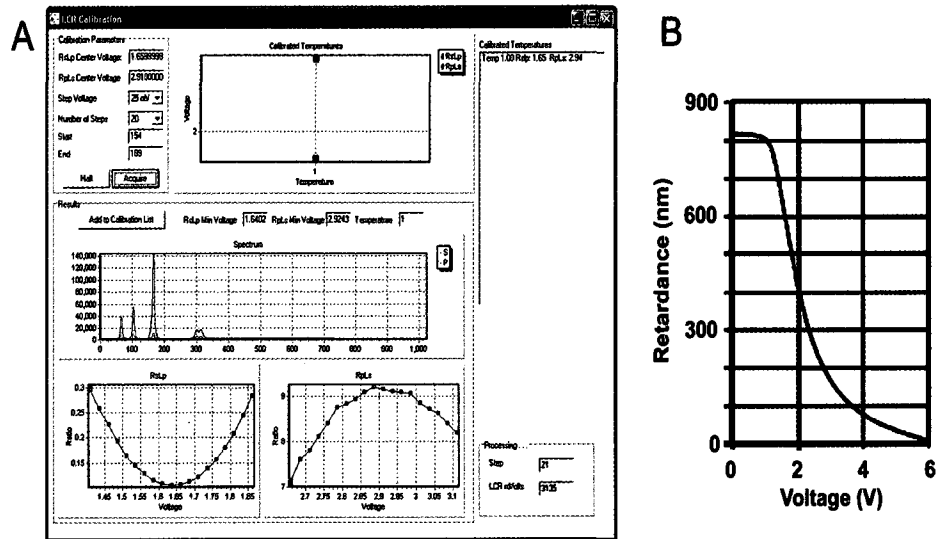
Figure 14. A) The LCR Calibration window with typical calibration curves displayed. B) The near infrared LCR voltage vs optical phase retardance plot.

What is physically taking place during the **LCR calibration** routine?

RsLp indicates that right-hand circular polarized light R is converted to S polarization, and left-hand circular polarization L is converted to P polarization. It indicates the desired state of the LCR.

All linear rotators are rotating and the $\lambda/4$ plate on the incident rail is in the beam. This will result in circularly polarized light being incident on the sample, which from a highly polarizable sample such as CCl_4, results in circularly polarized scattered light, with a sense common to that of the incident beam.

The orientation of the $\lambda/4$ wave plate about the optical axis is determined by placing a linear polarizer (analyzer) in front of a photo detector, positioned on the sample

136

rail at the far end of the sample compartment. While observing the photo detector output on an oscilloscope, the $\lambda/4$ plate is rotated until a minimum oscillation in the waveform is observed, then locked into place. Note: Because optical elements are not perfect, the waveform cannot be reduced to a flat line. Once the $\lambda/4$ plate is aligned, unless the Glan-Thompson polarizer is reoriented about the optical axis, there should be no reason to reposition the $\lambda/4$ wave plate.

The LCR's ordinary plane is orientated at 45 degrees. to the GTP and the polarization analyzer. This axis is marked on the LCR housing.

A ramped (square) wave voltage results in a phase shift and the application determines the optimum voltages for $\lambda/4$ and $3\lambda/4$ ($-\lambda/4$).

In principle, at these voltages, the circular polarization is converted to purely linear S or P polarization. In reality, this is not quite true due to imperfections in real world optical elements.

The **RsLp** and **RpLs** plots are the ratios of the integrated intensity over the selected pixel range for the two halves CCD array, as described in the **LCR Calibration** section below.

Some of the ROAS systems have LCR's with integrated temperature sensors, while others do not. Proponents argue that the phase retardation vs voltage will drift with changes in the temperature of the device; in this case the room temperature, and that compensation for changes in temperature is needed. On systems where temperature monitoring is an enabled option, interpolation or extrapolation is employed to optimize the LCR for the current temperature. Our experience has been that the ROAS is pretty

insensitive to the exact LCR voltage, so any drift based on temperature is not really significant.

1) **LCR Calibration using carbon tetrachloride (CCl₄)**

2) Place a CCl₄ sample into the sample mount.

3) Set the system into **Easy Calibration Mode** by choosing **Calibration | Easy Calibration Mode** from the main menu.

4) Go to the main screen and press **Quick Scan**. Optimize the sample position for maximum peak amplitude, then adjust the exposure time and / or laser power so that the **Max CCD Output** meter is in the high green range.

5) Once the sample intensity is set, find the ~460 cm^{-1} band of CCl₄. Set the display to pixels and locate the same peak. Pick two points (in pixel numbers), one on each side of the peak, and note the starting and ending pixel numbers.

6) Go to the **LCR Calibration** screen by choosing **Calibration | LCR Calibration** on the main menu.

7) Enter the starting and ending pixel values noted above into the **Start** and **End** fields of the **Calibration Parameters** panel. These numbers may have to be dithered to get a proper curve.

8) Enter starting values for the **RpLs** and **RsLp** voltages. If the instrument has been previously calibrated, these numbers can be estimated by looking in the **Calibrated Temperatures** table to the right of the screen.

9) Set the **Step Voltage** to 20 mV, and the **Number of Steps** to 20.

10) Press the **Acquire** button to begin the calibration process. The instrument will now step through a range of voltages centered about the two center voltages to find the optimum LCR voltage, at the current temperature, if applicable. The typical **RsLp** line shape will be a smooth curve, while the typical **RpLs** line shape is not (**Figure 14A**). The difference in the smoothness between the **RsLp** and **RpLs** plots is at least partially attributed to the difference in the rate of change in the phase shift versus voltage in **Figure 14B**. Worth noting, the rate of change differs more for the NIR LCR, than for the visible light LCR commonly used in *Chiral*Raman spectrometer.

11) Once the calibration process is complete, the user will see the **RsLp** and **RpLs** windows that contain plots of intensity ratio vs. voltage. If all is well, these should be reasonably smooth curves with one showing a minimum and the other showing a maximum. Furthermore, the **RsLp** and **RpLs Min Voltage** boxes should now show the interpolated optimum voltages for the LCR. These should be close to the minimum (**RsLp**) and maximum (**RpLs**) voltage values observed in the two plots.

12) If these voltages look reasonable, press **Add to Calibration List** to accept them. If the graphs have obvious outlying points, it is usually best to re-run the calibration process. Adjusting the intensity level by shutter speed and laser power can improve the smoothness of the graph, if repeated runs prove to be noisy. As of v3.20, the accepted calibration curve will replace, not be added to the data stored in the **Calibrated Temperature** window. If the

temperature compensation option is enabled, the calibration curve will be added to the list. This option is not presented in all versions or ROA.

Comment: producing nice curves can be tedious.

1.5.2.3.3   Image Alignment and Binning
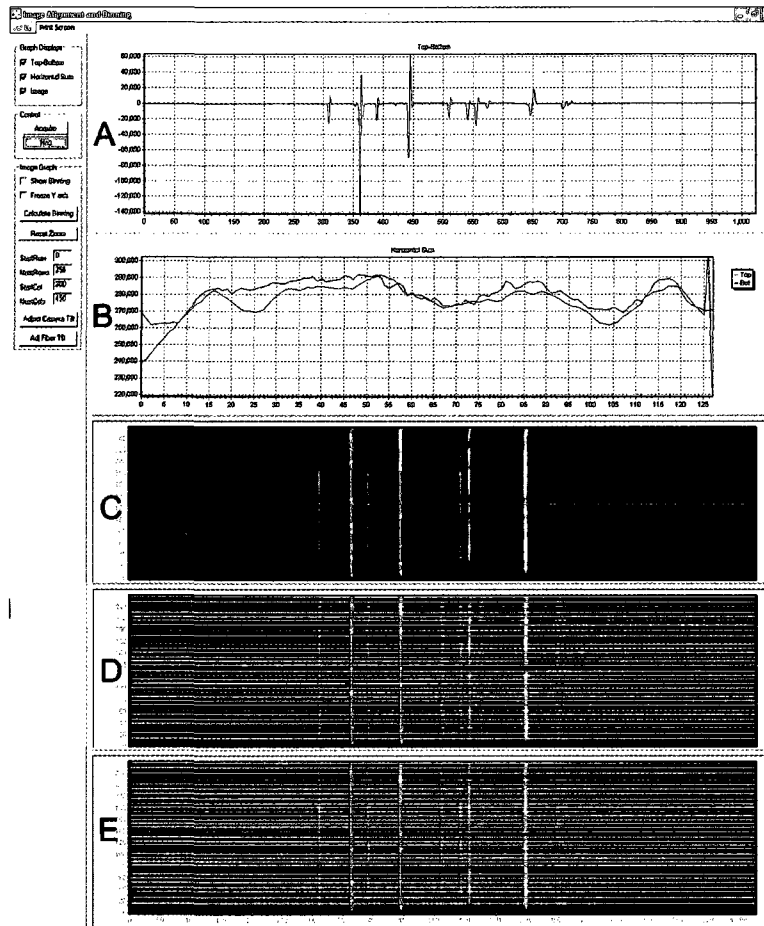
Figure 15. Image Alignment and Binning screen. **A)** Top minus Bottom spectra, **B)** Horizontal Sum, **C)** Image of CCD without the current binning displayed, **D)** Image of CCD with the current binning displayed, **E)** Image of CCD with recalculated binning displayed. Note: Only one image of the CCD will be displayed at one time in the ROA application.

The **Image Alignment and Binning** screen is used to optimize the alignment of the fiber optic bundle to the polarization analyzer, and the FO cable and CCD array to the

141

spectrograph. This routine is also used to determine the binning pattern of the CCD. The binning pattern may need to be repeated occasionally to optimize the light collection. When the **Image and Alignment Binning** window is active, the system operates in Raman mode, i.e., the [CC] logic state is [00]. Anytime the instrument is realigned, the binning optimization routine should be run.

Truly, **Image and Alignment Binning** adjustments are an art-form developed with experience.

Image Alignment and Binning pull down menu

SetUp options include, **Acquisition SetUp** and **Gray Scale**

Acquisition Setup brings up the **Acquisition Setup** window. This option is here so that it is not necessary to close the **Image Alignment and Binning** window, adjust the setup on the main screen, and then reopen the window, repetitively, to get the exposure time set correctly for this screen. It is simply a time-saver.
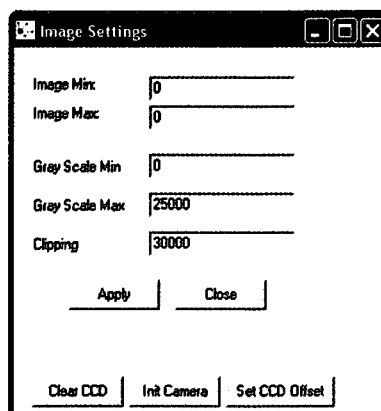

Figure 16. The Gray Scale | Image Setting window.

Gray Scale| Image Setting window allows the user to effectively zoom in amplitude on the image. The Gray Scale settings allow the user to set the max and min pixel amplitudes used in coloring the image. Anything <u>above or below</u> the <u>max or min</u> value will show as red.

The Image Min and Image Max value(s) are displayed to assist the user in selecting an appropriate Gray Scale Min and Max. The Clipping value allows the user to set a "clipping level" which is lower than the Gray Scale Max. This is normally not necessary.

These settings are helpful when looking at a peak (line) that is much fainter than the maximum intensity line. Normally the image will scale to the max intensity pixel, but if the user is trying to look at a faint line, he / she can lower the Gray Scale Max to get it closer to the top value in the faint line.

Set CCD Offset. This feature is obsolete and will likely be removed from later versions of ROA.

Auto Gray instructs the software to automatically scale the intensities in the image each time an image is acquired.

Image Alignment and Binning controls are displayed on the left side of the screen.

Graph Displays allows for selective display of the Top-Bottom, Horizontal Sum and Image plots.

The **Top-Bottom and Horizontal Sum** plots, **Figures 15A** and **15B** respectively, display a vertical axis measured in A/D converter counts. This is a good relative measure of intensity.

The **Top-Bottom** (pronounced top minus bottom) plot (**Figure 15A**) displays the intensity difference between the lower and upper halves of the CCD array. This display is used to adjust fiber input tilt. When correctly adjusted, this plot should show a fairly small peak amplitude. Minimizing these peak amplitudes will increase the number of counts that can be collected before the **CCD Max. Output** meter moves out of the green range. Ideally, the shape of each peak should be symmetrical about its center, i.e., a "W" or "V" line shape. If the peak shows an **N** shape (positive then negative) or the opposite, this is an indication that the fiber optic cable is rotated slightly, relative to the spectrograph diffraction grating. It may not be possible to eliminate all non-ideal line shapes across the spectrum. **Figure 15A** represents an ideal alignment.

The **Horizontal Sum** plot, (**Figure 15B**) displays the horizontal sum plots of counts along the selected rows of the upper and lower halves of the CCD array. Put another way, it quantitatively indicates the energy distribution along the upper and lower columns of CCD pixels. This plot is used to adjust the launching lens and fiber input. Ideally, the plot should not have strong peaks, but rather, a fairly smooth distribution of light.

To minimize spectral collection time, it is important that (to a reasonable approximation), that the scattered light intensity be uniformly distributed along the CCD column. This is because the minimum spectral acquisition (exposure) period is limited by

the highest intensity pixel limit. The line shapes do not need to be identical. However, the mean or average line positions should be similar in amplitude.

The intensity distribution is controlled by the alignment of the fiber optic bundles to the arms of the polarization analyzer. To achieve the best approximation of an equal number of counts from the upper and lower halves of the CCD array, the **Calculate Binning** routine determines which rows will be binned for spectra collection

Image The image of the CCD array (**Figure 15C**) graphically indicates the relative intensity of each CCD element. The CCD Image is the best tool for optimizing the fiber optic bundle to polarization analyzer alignment, spectrometer alignment, and spectrometer focus. The **Image** is updated two (2) exposures after acquisition.

Since the main screen includes the **Max CCD Output** meter, binning is not as critical as it would otherwise be, because when properly adjusted, the probability of saturating or overexposing the CCD has been minimized. However, for optimum performance (primarily optimum collection speed), it is best to have the binning pattern set reasonably well. Once the pattern is set, it is probably not necessary to reset it, under normal circumstances. Before adjusting the binning, adjust the Ne lamp position and intensity, as the user would for a normal ROA acquisition. If the **Image Alignment and Binning** plots do not update, reduce the lamp intensity by moving it away from the objective lens. To set the binning pattern, go to the **Calibration | Image Alignment and Binning** screen.

Setting the **Binning** pattern: The **Image Alignment and Binning** screen can display three plots, each of which can be displayed or hidden, by checking / clearing a box in the **Graph Displays** panel. Any combination of plots may be displayed. In the **Image Graph** panel, check the **Show Binning** box. Press the **Acquire** button to acquire an image. Once a valid image (determined by the application) has been acquired, the current binning pattern will be displayed as white lines overlaid on top of the image (**Figure 15D**). The white binning lines should be closer together in higher intensity portions of the image and further apart in lower intensity portions.

In **Figure 15**, the CCD columns 0-1024 and rows 0-256 are selected. When selecting rows or columns, the beginning row or column number is entered in the **StartRow** or **StartCol** box. The range of rows, or columns are entered into the **NumRows** or **NumCols** box(s). For example: if **StartCol** = 100 and **NumCols** = 200, the CCD will be evaluated for pixel columns 100-300. When acquiring a spectrum, the response time or cycle time is a function of the number of pixels to be evaluated. It may be advantageous to reduce the number of columns or rows at times, for example, when focusing the image of the fiber optic cable on the CCD array.

The CCD array is illuminated using a Ne calibration lamp. Position the calibration lamp on the sample compartment rail, far from the objective lens and insert the calibration lamp. It may be necessary to adjust the position of the Ne lamp fixture for optimum signal strength. The **Top-Bottom** plot shown in **Figure 15** appears as expected in that, the predominant line shapes are that of "W" and "Z", as opposed to "V". The line shapes result from the fact that the spectrometer focus, not to be confused with the sample focus, may not be exactly the same for the top and bottom, across the upper and

146

lower areas of the CCD array. Also, the photon counts on the upper and lower halves of the CCD array are never exactly equal. Therefore, it is expected that the **Top-Bottom** plot will have peaks, even when there is no chirality in the sample, i.e, a lamp. The alternating state of the LCR, should completely eliminate this over a scan. This cancellation is not observable in the **Image Alignment and Binning** window. However, in the main application window, when **Setup | Display only Complete Cycles** is not enabled, the ROA spectra is displayed every other scan, such that the spectrum is composed of two summed spectra from a common [CC] state and opposite LCR states.

Reset Zoom resets the **CCD Image** x and y axis to full scale if, and only if the **Adjust Camera Tilt** and **Adjust Fiber Tilt** modes have not been enabled since the application was opened.

Adjust Camera Tilt and Adjust Fiber Tilt are convenient in that **Adjust Camera Tilt** displays the CCD image over the pixel ranges of 1-1024 and 100-150 and **Adjust Fiber Tilt** displays the CCD image over the pixel ranges of 400-760 and 1-256. Unfortunately, at the time of this writing, if either option is selected, the CCD image cannot be zoomed back to 1024 x 256 by a mouse drag or entry into the –**Row** or –**Col** boxes. The ROA application will have to be closed and reopened to return to the full image. This will be addressed in new releases or ROA.

1.5.2.3.4   Easy Calibration Mode

Calibration | Easy Calibration Mode

Opens the incident shutter and <u>overrides the sample compartment laser safety interlock</u>. When enabled, a red warning message is placed at the bottom of the main screen to remind the user that the system is in this mode.

Be sure to wear laser eye protection goggles suited for operation at the laser's power and wavelength. If the laser intensity is high, the user must also take care not to put his hands or any flammable material in the path of the beam!

1.5.2.3.5   Engineering

In general, the **Engineering** windows are self-explanatory to someone who understands the instrument, and has read this document. It serves little purpose to discuss all the information displayed in these windows. However, there are a few points that should be made.

1.5.2.3.6   Instrument Setup (Factory Settings)

Although it can be viewed to enhance the user's understanding of the *Chiral*Raman spectrometer, the engineering section is most useful as a diagnostic tool. These pages should be locked to prevent alterations by anyone other than the manufacturer
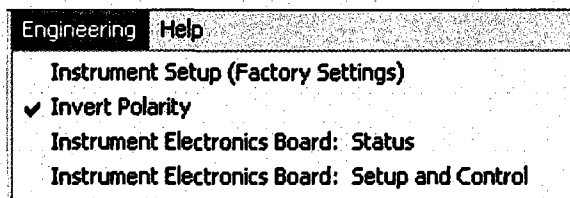

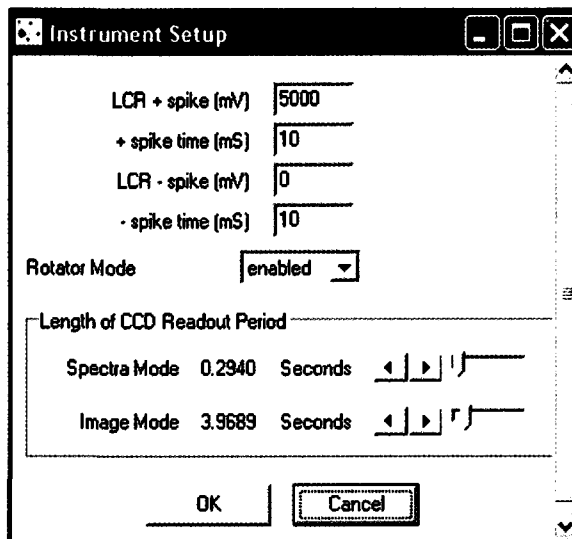**Figure 17.** Engineering pull down menu.

Figure 18. Engineering | Instrument Setup window.

In the **Instrument Setup (Figure 18)** window, the parameter of interest that can

be user-adjusted may be the **Length of CCD Readout Period | Spectra Mode**. This

parameter is set by the manufacture or field engineer. It determines the amount of time

allotted for the CCD to be read out and the data transferred to the computer. If this period

is too small, **CCD Overflow** errors will be generated and the data will be discarded (this

is different from the DSS routine). **Overflow** errors (counts) will be discussed in the **IEB**

Status section. The correct setting is a compromise between the data transfer speed and

minimizing the time required to collect ROA spectra.

It may be possible to decrease the factory setting to reduce collection time but if

reduced too much, losses to overflow errors will quickly increase the collection time.

This parameter may also need to be optimized if a supporting computer or a computer's

operating system changes. Changes in the camera communication format, for example,

upgrading camera communications from a Serial to USB or Ethernet, will allow the read-

out period to be decreased.

150

1.5.2.3.7   Invert Polarity

This feature compensates for the case where the inputs of the fiber bundles have been coupled to the wrong arms of the polarization analyzer. When enabled, the ROA data is multiplied by -1, thus flipping the spectra about the horizontal axis to satisfy the chiral sign convention. There is no impact on the quality of the data. Alternatively, the input ends of the fiber bundle may be switched to opposite arms of the polarization analyzer followed by realigning the fiber bundles and by recalibrating the camera.

The fibers at the output of the fiber bundle are arranged along a radius to compensate spherical aberration, which is inherent to spectrographs. Rotating the bundle 180 degrees at the spectrometer will introduce a significant curvature in the image of the bundle on the CCD array. Thus, this is not an alternative to the solutions mentioned above.

1.5.2.3.8   Instrument Electronics Board: Status

The **IEB Status** (Instrument Electronics Board) window, shown in **Figure 19,** is both a comprehensive real time display of instrument conditions, and a display of conditions at the end of the last scan. The information is not written to a log file, and will be lost, when the next scan is started or the application is closed. This virtual window into the instrument's interior is primarily used during installation, and for trouble shooting by the field engineer.
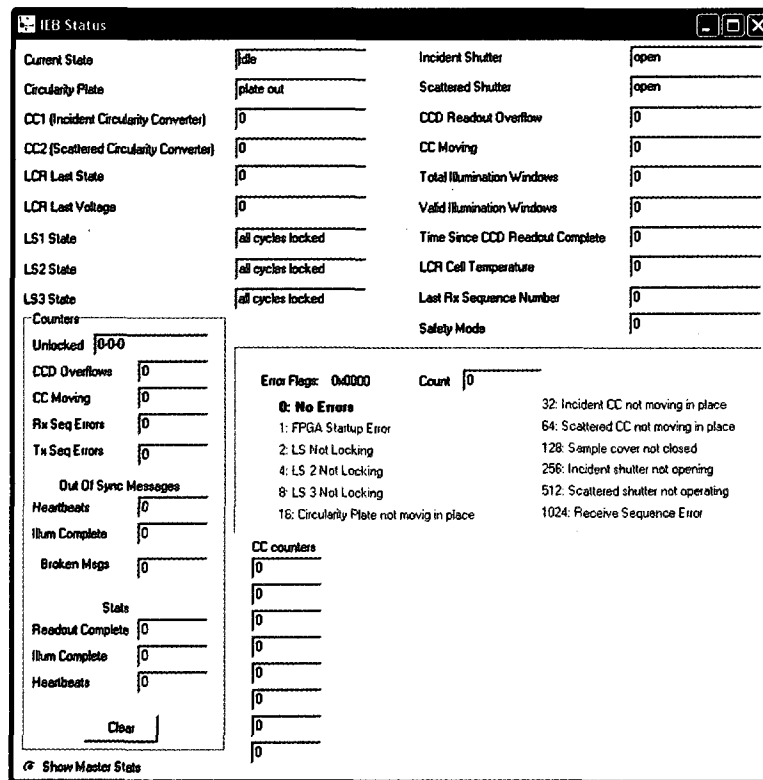

Figure 19. The Instrument Electronics Board: Status window.

The upper-left section of the window displays the logic state of CC_1, CC_2 and the LCR. The upper-right area is associated with the camera. The information displayed and

the significance of this information should be intuitively understood. Information in this window of interest to the user, or input by the user is generally accessible in or through the main application windows.

The **IEB Status | Counters** are most useful as a diagnostic tool.

Unlocked indicates the number of times and which LR motor loses synchronization. These values should remain zero.

CCD Overflows indicates that more time is needed for data transfer from the CCD camera to the computer. The Overflow value also increasees by eight (8) for each **DSS** count. This can occur for several reasons, ranging from hardware / software communication to saturation of the CCD array.

When a scan is initiated, the system will "clear" the CCD array of charge by reading out the dark noise eight (8) times. During this clearing period, the **CCD Overflows** counter will register errors. The number of errors will scale with the single exposure time, at ~ 10 per second. On the 9th exposure the counts should cease to increase. It is possible that the # of counts will slowly increase during the Scan period. This is where the user has to make a judgment call: to balance the quest for counts vs. the total collection time. **Length of CCD Readout Period** is the only parameter adjustable by the user. In principle, this value should not need to be altered from the factory setup. The need to make significant changes may indicate a significant hardware or software problem.

The system seems to be more susceptible to **CCD overflow** errors when the sample's signal to noise ratio (SN) is low. It is not clear why this occurs.

Out Of Sync Messages | Heartbeats when a scan is started this value will be reset to zero and may initially display a few counts, but should then remain constant for the duration of the scan. After the scan terminates, the counter will begin incrementing at approximately the rate of the **Stats | Heartbeats** counter because spectra are no longer being acquired.

Stats | Heartbeats indicates that the computer is communicating with the Camera. The counter will begin counting when the ROA application begins to collect spectra. The counts will continue to increase after the scan ends until a new scan begins, after which, the counters are reset to zero (0), and counting resumes.

If the heartbeats are not observed, it is likely that the serial communications cable is not connected.

Stats | Illum Complete and **Stats | Readout Complete** counts should be within a few counts of the **Heartbeat** value during a scan.

Error Flags are self-explanatory.

CCD Threshold is the DSS threshold value that has been entered in the **Setup | Acquisition Setup** window. It cannot be edited from the IEB window.

1.6 Camera Alignment Procedure

This procedure describes the alignment process for reinstalling the camera in the ROA system. This procedure does not use the laser as a source, so ensure that the laser shutter is closed and that laser emission is disabled while performing this procedure.

Once the camera is mounted to the spectrograph, turn on the camera power supply and the ROA electronics power. Make sure that the USB or ether net cable is connected to the camera, and open the ROA software. Bear in mind that the various adjustments to the camera can at times interact, so the user may need to repeat certain adjustments before optimum positioning is achieved.

1.6.1 Initial Focus adjustment

The initial focus adjustment is performed using the **Image Alignment and Binning** screen. Before beginning, take the cover off the spectrograph and look at the position of the Nikon lens in front of the camera. Set the focus on the Nikon lens to about 10 feet and replace the spectrograph cover.

Select **Calibration | Image Alignment and Binning** from the main menu. Push the **Adjust Camera Tilt** button. Place the neon lamp near the sample cell position. Press the **Acquire** button to begin acquiring spectra If the image is too intense, the user may need to move the lamp farther from the sample position to reduce the light, or to reduce the exposure time in the **Setup | Acquisition Setup** window. If **DSS** is enabled, pixel intensity exceeds the user defined **Threshold**, the CCD image screen will not update. **DSS** errors will be counted on the **Main Screen**. Similarly, if the image is too faint, adjust the lamp for more light, or increase the exposure time.

Loosen the setscrew on the fiber ferule mount at the entrance to the spectrograph to allow the ferule to be moved in or out, relative to the spectrograph. The ferule is the large cylinder at the end of the fiber optic cable. While looking at the **Image** screen, move the ferule in or out of the spectrograph to get the sharpest possible lines from the neon lamp. This will be optimized later. Do not worry at this point if the lines are not perfectly vertical. Once the lines are as sharp, tighten the setscrew to clamp the ferule in place. The ferule and mount should be rapped with black cloth to block light that will leak through the ferule mount, into the spectrometer, causing large spectral artifacts. This point cannot be over emphasized.

1.6.2   Camera Vertical Height and Tilt Adjustment

Fluorescent room light, or a Ne calibration lamp can be used to adjust the vertical position of the camera.

Place a white piece of paper between the slow linear rotator (LR2) and the second circular converter (CC2), on the scattered rail at about 45 degrees to the ceiling, so that it reflects some of the fluorescent lighting into the scattered rail collection optics.

In the ROA software, go to the image alignment screen by selecting **Calibration | Image Alignment and Binning** from the main menu. Push the **Adjust Camera Tilt** button. Press the **Acquire** button to begin acquiring frames. If the image is saturated, move the paper along the optical path to reduce the light, or you may need to reduce the exposure time in the **Setup | Acquisition Setup** window. Similarly, if the image is too faint, adjust the paper for more light, or increase the exposure time. Once a reasonable image is attained, begin to adjust the camera height and tilt as follows:

1) Loosen the four camera mounting screws so that the camera can be moved, but not easily.

2) Notice in the CCD image of the upper, and lower sets of fiber optics that there is a small gap running approximately horizontally through the middle. It may be necessary to further reduce the illumination intensity or exposure time to see the gap. This is the separation between the two (2) fiber bundles in the spectrometer's object plane.

3) Adjust the height of the camera until the gap is approximately in the center of the image. The height adjustment screw is either a 6 mm cap-head or setscrew in the center of the top of the camera mounting assembly on the spectrometer. There is a faint green line on the CCD image screen indicating the exact center of the CCD array. Try to get the gap evenly centered on this line.

4) If it becomes necessary to lower the camera height, friction between the camera and spectrograph mounting plates may prevent the camera from sliding down when the adjusting screw is rotated counter clockwise (CCW). Bear in mind that the vertical target position has a tolerance of ~ 50 μM. Normally, it is best to make the final adjustments so that you are raising the camera (CW) to bring the camera into position

5) If the gap tilts from right to left, or from left to right, adjust the tilt of the camera. This is done by loosening the tilt adjust setscrew on one side of the

camera and tightening the opposite setscrew. These set screws are located on the left and right side of the camera mounting assembly near the top.

6) Steps 3 through 5 may have to be repeated, in order to properly achieve this adjustment.

7) Once the height and tilt are satisfactory, gently tighten the four camera mounting screws to lock the camera into position. Check the alignment once more to ensure that it was not disturbed while tightening the screws.

1.6.3 Fiber Tilt Adjustment

The fiber tilt procedure aligns the image of the fiber optic cable to the columns of the CC array. The orientation of the image of the fiber cable to the CCD array is adjusted by rotating the fiber optic ferule, using the adjustment on the spectrometer. This is a critically important and very meticulous task.

1) Place the neon calibration lamp in the sample compartment.

2) Press the **Adj. Fiber Tilt** button. Begin acquiring images by pressing Acquire.

3) Adjust the lamp position to give strong lines without saturating.

4) When the fiber is correctly oriented, the **Top-Bottom** graph will ideally show peaks that are V-shaped, inverted V-shaped, W-shaped or inverted-W shaped. These equate to spectral lines that are primarily incident on two (2) columns or one column respectively. It is not possible to eliminate all sigmoid peaks. The final tweak will result in minimal values on the y-axis of the **Top-Bottom** plot. Again this is a very meticulous adjustment.

1.6.4   Focus Adjustment

Once the alignment is completely adjusted, the focus can be adjusted as well. This adjustment is made from the main ROA screen.

Set up the neon lamp as the source and press **Quick Scan** to begin acquisition. Adjust the focus control on the spectrometer (under the end of the spectrometer near the camera) to maximize the heights of the peaks in the Raman spectral display.

1.7 COM Port Selection

The selection of the COM port used to communicate with the board electronics is normally COM port 1. If for any reason a different COM port is needed for this function, the **roa.ini** file must be modified. To do this, open the Windows Notepad application, **Start | Programs | Accessories |Notepad**, and open the **roa.ini** file in the **C:\Program Files\Critical Link\ROA** directory. Near the top of the file is a line, which looks like this: "com Port=1". Change the COM port number to the desired COM port and save the file. The next time the software is run, the new COM port will be used.

When using the USB-Camera interface, the same <u>physical</u> USB port will have to be used, or the **roa.ini** file will have to be modified to address the correct USB port. Optionally, the camera's Ethernet interface can be used. Relative to USB, with the Ethernet interface the camera read-out time can be reduced. The camera's IP number and serial number are written on the camera. Contact BioTools for assistance with this configuration.

1.8 Simulation Mode

The simulation modes are used for diagnostic procedures and to allow demonstration of the *Chiral*Raman. The simulation mode is accessed by a right-clicking on the **Accumulate ROA** button. The Raman spectrum is that of cyclohexane. In addition to the simulation modes, the cyclohexane spectrum will appear anytime the ROAS is turned off, or the camera has not been cooled down to the design operating temperature, if either **Quick Scan** or **Accumulate ROA** is enabled.
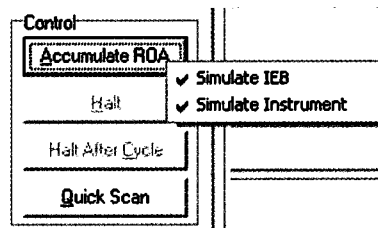

Figure 20. Simulate IEB and Instrument simulation menu.

Two (2) options will be presented:

Simulate IEB

Simulate Instrument

Either of the two, when preceded by a check mark, becomes active. **Simulate IEB** simulates the operation of the Instrument Electronics Board in its entirety. If **Simulate Instrument** is checked, the system can be used to communicate with an IEB without encountering errors, due to circularity converter motors not operating correctly. For normal operation, both of these should be disabled (unchecked) See **Section 1.8.1**. For demonstrations, both items should be checked.

When demonstrating this software on a laptop with no COM port, the **roa.ini** file must be modified. To do this, open the Windows Notepad application, **Start | Programs | Accessories | Notepad**, and open the **roa.ini** file in the **C:\Program Files\Critical Link\ROA** directory. Near the top of the file is a line which looks like this: comPortAvailable=1. Change the 1 to a 0 to disable the use of the serial port.

1.8.1 Grief Saving Comment

Failure to disable both the **Simulate IEB** and the **Simulate Instrument** options when connected to a ROA spectrometer and collecting data, will result in highly unstable behavior. This is because the application is receiving conflicting information from a real and a virtual instrument. The problems can include any aspect of operation that "should be working". False cosmic rays that appear to be getting by the **DSS** filter and lost data files are classic indications of a simulation mode(s) being enabled.